SANDIA REPORT

SAND2012-7831
Unlimited Release
Printed September, 2012

Bridging the Gap Between Atomistic Phenomena and Continuum Behavior in Electrochemical Energy Storage Processes

S. Davidson, S.K. Griffiths, J.W. Lee, R.E. Jones, A. Kung, R.H. Nilson,
M.N. Salloum, J.A. Templeton, D. Ward, B.M. Wong

Prepared by
Sandia National Laboratories
Albuquerque, New Mexico 87185 and Livermore, California 94550

Sandia is a multiprogram laboratory operated by Sandia Corporation,
a Lockheed Martin Company, for the United States Department of Energy's
National Nuclear Security Administration under Contract DE-AC04-94-AL85000.

Issued by Sandia National Laboratories, operated for the United States Department of Energy by Sandia Corporation.

Available to DOE and DOE contractors from
U.S. Department of Energy
Office of Scientific and Technical Information
P.O. Box 62
Oak Ridge, TN 37831

Telephone: (865) 576-8401
Facsimile: (865) 576-5728
E-Mail: reports@adonis.osti.gov
Online ordering: http://www.osti.gov/bridge

Available to the public from
U.S. Department of Commerce
National Technical Information Service
5285 Port Royal Rd
Springfield, VA 22161

Telephone: (800) 553-6847
Facsimile: (703) 605-6900
E-Mail: orders@ntis.fedworld.gov
Online ordering: http://www.ntis.gov/help/ordermethods.asp?loc=7-4-0#online

SAND2012-7831
Unlimited Release
Printed September, 2012

Bridging the Gap Between Atomistic Phenomena and Continuum Behavior in Electrochemical Energy Storage Processes

Scott Davidson, Stewart K. Griffiths, Jonathan W. Lee,
Reese E. Jones, Andy Kung, Robert H. Nilson,
Maher N. Salloum, Jeremy A. Templeton, Donald Ward, Bryan M. Wong
Sandia National Laboratories, P.O. Box 969
Livermore, CA 94550-0969

Abstract

One of the most significant impediments to advances in electrochemical energy storage lies in the gap between fundamental understanding of atomistic phenomena and our understanding of the impact of these phenomena on system performance at device scales. Atomistic models (DFT, MD, MC) provide insight into such phenomena along with a means of quantification, but such models are too computationally intensive to address device-scale behavior. Similarly, device-scale insight for design and optimization can be obtained through continuum models that are sufficiently fast, but these models account for only the simplest atomistic phenomena. There is thus a large gap between our ability to develop fundamental understanding and our ability to use this understanding to make rapid advances in energy storage technologies. The goal of this work is to help bridge this gap through an innovative synthesis of atomistic and continuum approaches in which atomistic phenomena are captured through fast reduced-order integral methods that can be imbedded into continuum-like models describing device-scale behavior.

Acknowledgment

Funding for this effort was provided by the Laboratory Directed Research and Development (LDRD).

Contents

List of Figures

List of Tables

Chapter 1

Introduction

Electrochemical energy storage is a critical technology for reducing petroleum consumption via vehicle electrification and for reducing carbon emissions from both transportation and stationary power generation via increased reliance on intermittent renewable sources. Despite this importance, however, batteries today suffer from low power density, low energy density, poor low-temperature performance, limited cycle life, high cost, and a host of safety concerns [2, 1]. Capacitors offer high power density and more-or-less unlimited cycle life, but their energy densities are very low even compared to present batteries and their costs are still much too high for widespread adoption in these applications.

The many needed improvements in batteries and capacitors will require major advances on multiple fronts, including improved electrolyte chemistries and improved anode, cathode, and separator materials [23]. These advances will in turn require improved fundamental understanding of the underlying electrochemical and transport phenomena governing materials performance at atomistic scales, as well as the practical embodiment of this fundamental understanding in computational tools that enable device design and optimization at scales many orders-of-magnitude larger than atomistic. This final step of linking atomistic phenomena to continuum scales is thus an essential bridge between fundamental science and the practical innovations having large impact at device scales.

Most atomistic phenomena relevant to energy storage are now well described by a suite of computational tools including Density Functional Theory (DFT) at both molecular and subatomic scales, various Monte Carlo (MC) methods, and Molecular Dynamics (MD). Collectively, these tools provide fundamental insight into the double-layer structure, as well as the kinetics of charge transfer at surfaces and in pores down to atomic size. Unfortunately, these methods are also extremely slow, requiring days, weeks or even months for solutions involving at most a million atoms over times generally much less than a microsecond. As such, these methods cannot address long-range ion transport and similar device-scale phenomena required for device design, and they certainly cannot address materials optimization because this inherently involves numerous calculations as well as interactions between atomistic processes and device-scale transport. In contrast, continuum-scale models do address device-scale phenomena such as heat transfer and long-range transport, but this speed comes at the expense of neglecting nearly all atomistic phenomena due to the widely disparate length and time scales of atomistic phenomena and the device. Moreover, the coupled and multi-grid methods commonly used to address disparate scales are not helpful in these problems because the required sub-grid calculations are still much too slow to perform in

real time.

The gap between atomistic theory and continuum models is thus substantial, and this seriously impedes our ability to apply fundamental understanding of atomistic phenomena to the challenge of making rapid advances in energy storage technologies. The objective of this project is to help bridge this gap. To do so, we have undertaken efforts in three main areas. First, a quantum DFT study of water under confinement has been performed to begin to understand how solvents change in the near-surface region of electrolytic flows. In electrochemical applications, surface chemical reactions are critical to device performance. Typically Butler-Volmer equations are used to model the electrochemistry, but these relations are built upon many approximations. Without a deeper understanding of how polar molecules are affected by the quasi-two-dimensional fluidic structure and electric fields at interfaces, it is not possible to test these assumptions and develop better models. The work performed in this project has shown that water forms previously unknown structures under certain conditions, and quantifies how electron exchange becomes increasingly important.

The second aspect considered in this work was to develop a computationally efficient but physically accurate reduced order model of the electric double layer. Prior MD and DFT efforts have shown that atomistic effects dominate the Steric region of electric double-layers, and electrokinetic flow experiments have repeatedly shown significant deviations from the predictions of Poisson-Boltzmann theory. If atomistic behavior is not accounted for, a predictive model is not possible. A goal of this work was to build a predictive DFT model which has sufficient accuracy for engineering analysis. Rigorous comparisons were made between MD and DFT calculations to understand and rectify discrepancies between their results for a Lennard-Jones fluid at a charged surface. We were able to obtain excellent agreement between the two methods, both of which captured the divergence from the Poisson-Boltzmann double-layer model due to its lack of an atomistic description. As expected, the computational effort of the DFT model is orders of magnitude less than the MD counterpart. We have extended this DFT model to a simple polar solvent modeled by a dumbbell molecule. Because this model does not correspond to a real solvent, we have developed an optimization process to calibrate it against more accurate MD calculations involving realistically structured solvents (e.g., water). The result is a highly efficient DFT model which can correctly account for the discreteness of atoms at charged surfaces.

Finally, this work considered several methods to estimate classical transport coefficients from molecular simulations such that they are directly informed by the atomistic dynamics but can be used in efficient continuum models. Prior MD simulations had shown that accurate flow velocities can be obtained if the viscosity is based on mean densities integrated over the atomic density profiles [74]. Chapman-Enskog models had also been used to account for the density variations in electroosmotic flows [67]. In this work, we investigated two methods which can us MD simulations to directly inform continuum transport properties. The first is the Green-Kubo method which uses fluctuations in an equilibrium system to calculate transport coefficients such as viscosity and conductivity. A limitation is that the method was restricted to bulk systems. We have extended the theory to account for spatial inhomogeneities in one direction, in this case normal to the surface. Thus, we can identify spatially-varying transport models which is necessary for energy storage devices when the ionic concentration in the Stern layer can exceed that of the bulk by orders of

magnitude. The other approach we considered is to use Bayesian inference to estimate polynomial chaos expansions for transport coefficients from MD simulations. We demonstrated that this method can successfully infer continuum thermal conductivity relations from MD. However, we also identified regimes in which these models no longer hold. Specifically, at small length and time scales as well as over very large temperature ranges. Similar estimates were obtained from the Green-Kubo methodology. Thus, we can directly inform continuum transport models with atomistic physics and obtain bounds for their applicability.

The synthesis of this work provides a means by which high fidelity atomistic simulations, quantum DFT and MD, can be used to inform continuum DFT and transport models which are orders of magnitude faster to evaluate. It is therefore reasonable to expect that such models could be used for engineering analysis and design of electrochemical energy storage systems. The balance of this report provides the technical details related to each effort. First, Chapter 2 describes the results of confined water molecules obtained from quantum DFT associated with the first objective of this work. The second goal, development of an accurate DFT model, is described in Chapters 3 and 4. Methods to obtain MD-informed transport coefficients are provided in Chapters 5 and 6, constituting the final objective of the project. Some conclusions and suggestions for follow-on activities are provided in Chapter 7.

This page intentionally left blank.

Chapter 2

Density Functional Theory calculations of water in confined systems

Hydrated anions exhibit a diverse range of complex interactions due to the strong stability of hydrogen bonds that are spontaneously formed throughout the aqueous network. Since the solvation process usually results in a random orientation of molecules in the bulk, the formation of ordered anion/water clusters in chemical receptors allows a detailed characterization of molecular interactions in these confined environments. In particular, there has been significant attention on understanding the ordered water clusters in hydrophobic environments due to their importance in chemical and biological interfaces. Hydrogen-bonded water networks can naturally grow at the hydrophobic surface, often giving rise to a stable hydrate.

Upon solvation, a halide anion disperses its charge distribution spherically, making it an effective paradigm for anion hydration. Although hydrated halides such as X(H2O)n- have been the subject of numerous theoretical studies over the last several years, examples of encapsulated anion/water clusters by synthetic receptors are rare and are mostly limited to anions coordinated with a single water as X(H2O)-. Other hydrated anions have been characterized within lattices formed by a host matrix, a metal organic framework or between hosts. The structural characterization and energetic formation of anion/water clusters are essential for understanding mechanistic details of solvation processes, ion translocation in water-membrane interfaces, ion mobilities in the bulk, and electrical phenomena within aqueous/salt interfaces. In this chapter we report an unanticipated anion/water cluster assembled by one bromide and three highly-ordered "water tetramers" within the cavity of a bicyclic host L, providing a perfect C3 symmetric propeller-shaped bromide/water cluster [Br(H2O)12]- (Fig. 2.1). Such a highly symmetric, ordered assembly of a discrete anion/water cluster has not been reported previously or predicted theoretically. The rigid geometry of the host with its strategically-placed protonated nitrogens allows a stable, ordered assembly of three tetramer rings with the encapsulated bromide-stabilized geometry that is not possible in a bulk water system.

The bromide complex crystallizes as the hydrated bromide salt, [H6L(Br(H2O)12)]Br5, with four water molecules per asymmetric unit. The cationic unit is found to sit on a crystallographic 3-fold rotation axis, with the two tertiary nitrogen atoms unprotonated. One bromide is located inside the cavity lying on the bridgehead N1/N14 axis. As shown in Fig. 2.2, the internal bromide is hex-

This work was done in collaboration with the Hossain group at Jackson State University and was published in [83].

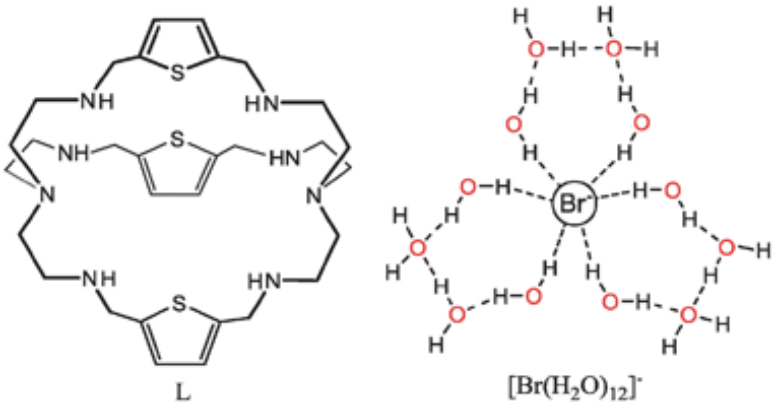

Figure 2.1. Bicyclic receptor L and [Br(H2O)12]- guest.

acoordinated with three "water tetramers," forming a propeller-shaped hydrate as [Br(H2O)12]- . The encapsulated bromide is directly linked to three pairs of water molecules bound between the cryptand arms. Each pair of water molecules is further connected to a water dimer (O4 and O1) with two strong hydrogen bonds, completing the bromide/water pentameric cycle. The water molecules are held with strong hydrogen bonds ranging from 2.66(3) to 2.77(2) , which are comparable to bond distances of 2.745(6) reported by Atwood and co-workers for the ice-like (H2O)8, and 2.72/2.93 reported by Fujita and co-workers for molecular ice (H2O).

In the bromide/water complex, each coordinating water molecule (O2 or O3) is further bonded with two protonated secondary amines (NH$\cdots$O = 2.75(2) to 2.92(2)) at both ends of L, providing an additional stability to these two water molecules as compared to other water molecules (O4S and O1S) in a given cycle, which is also reflected in the thermal analysis (discussed later). Three water molecules, which are directly coordinated with the bromide anion at each end of L, are linked alternately with three secondary amines to form a circular hydrogen bonding network (Fig. 2.1a and b). This specific arrangement of water molecules coupled with electrostatic interactions results in an interlocking of [Br(H2O)12]- within the cryptand to bring the anion/water cluster inside the cavity.

In order to characterize the nature of water molecules and the thermal stability of the complex, thermogravimetric analysis (TGA) and differential scanning calorimetry (DSC) at Jackson State University were performed. As shown in Fig. 2.3, the complex exhibited a first weight loss of 8.5% at a temperature of 200 °C, which corresponds to six water molecules. Another 8.5% weight loss occurred in the temperature range of 200 to 262 °C, corresponding to the remaining six water molecules. As seen in the solid-state structure, the complex contains twelve water molecules which are tightly held in the strong H-bonding network. The equivalent loss (8.5%) in the TGA, which corresponds to six water molecules at the two different temperature ranges, indicates that the water molecules are held with two different strengths in the cluster. The first loss could be due to the elimination of six water molecules that are not bound to the protonated amines, while the second loss could arise from the removal of tightly bonded water molecules with the cryptand as well as with the central bromide ion. This observation clearly indicates that the [Br(H2O)12]-

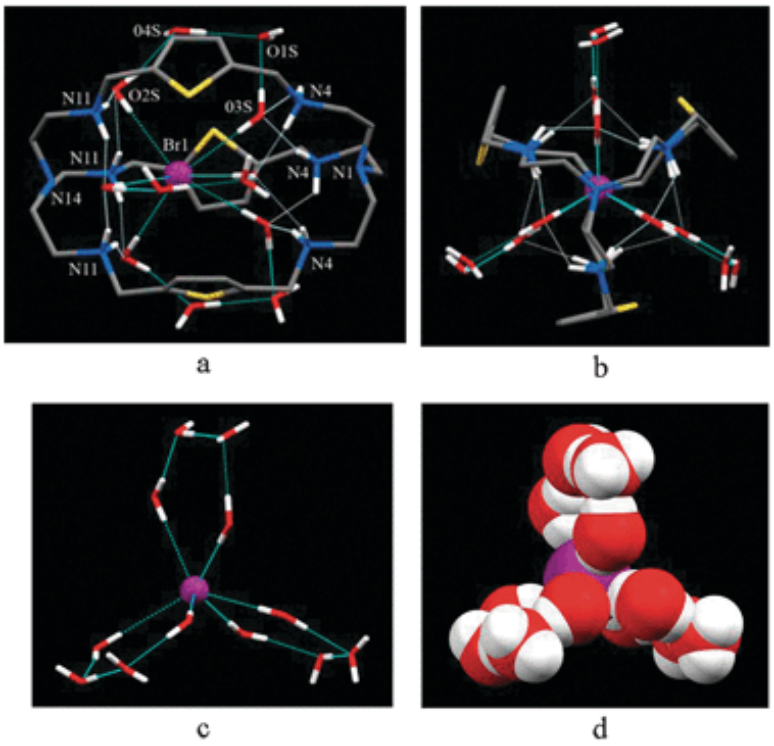

Figure 2.2. Crystal structure of [H6L(Br(H2O)12)]5+ showing the interlocked [Br(H2O)12]- guest with the cryptand: (a) side view, and (b) view down the three-fold axis (external bromides and hydrogen atoms of carbons are not shown for clarity); (c) perspective and (d) space filling views showing only [Br(H2O)12]-.

species is highly stable due to the interlocking with the cryptand, requiring high temperatures for the elimination of water.3m,10d. In the DSC, two exothermic peaks are seen at around 210 and 240 °C with 23 J g-1 and 43 J g-1, respectively. Further major weight loss (51.7%) in the TGA occurred at 350 °C, followed by 11.6% and 5.5% at 500 °C and 880 °C, respectively, due to the decomposition and combustion of the complex.

The formation of discrete, ordered [Br(H2O)12]- with the cryptand was indeed a surprise since the negatively-charged bromide was expected to interact directly with the hexaprotonated host. To further understand the energetics of this unusual situation, density functional theory (DFT) calculations were performed on both the cryptand/[Br(H2O)12]- complex and the isolated [Br(H2O)12]- species using the M06-2X hybrid functional which has been shown to accurately predict the binding energies of ions and other noncovalent bonding interactions in large molecular systems. Molecular geometries (including the empty ligand) were completely optimized without constraints at the M06-2X/6-31G(d,p) level of theory, and single-point energies with a very large 6-311+G(d,p) basis set were carried out in vacuo. Optimized geometries, vibrational frequencies, and enthalpies of formation were also calculated. Our calculations show that the cryptand/[Br(H2O)12]- complex has a complexation enthalpy of 627.4 kcal mol-1 and further indicate that the isolated [Br(H2O)12]-

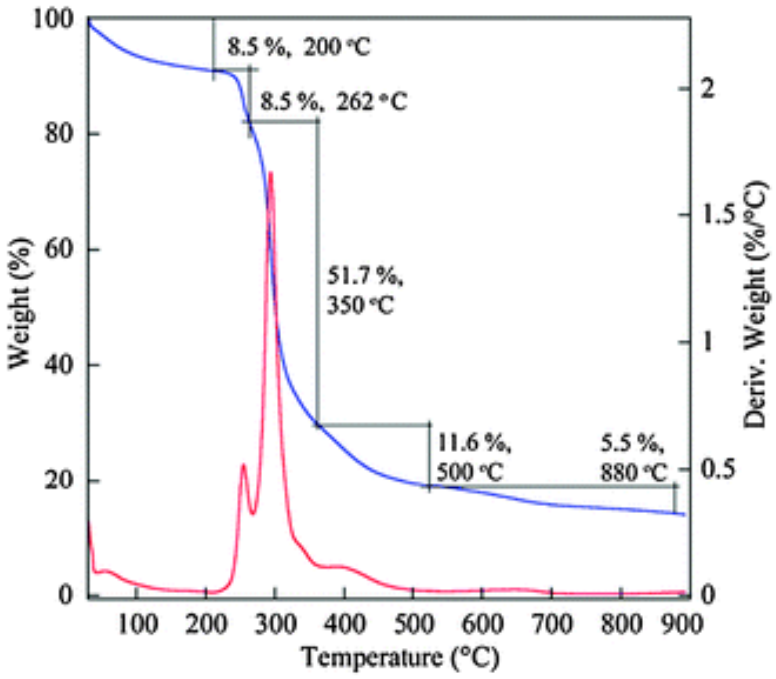

Figure 2.3. Thermogravimetric analysis (TGA) curve of [H6L(Br(H2O)12)]Br5 at a heating rate of 10 °C/min.

complex without the cryptand undergoes significant re-arrangement upon geometry optimization. In contrast, the C3 symmetry of the cryptand with its unique positions of protonated nitrogens at each of the C3-symmetric positions keeps each of the (H2O)4 tetramer units between the ligand arms (Fig. 2.4). The symmetric geometry of [Br(H2O)12]- with the cryptand is undoubtedly due to both the hydrogen bonding and positive charge of the cryptand as can be seen by the electrostatic potential.

In conclusion, we have presented a very unusual, highly-ordered anion/water cluster assembled by one central bromide anion and three "water tetramers" forming a discrete [Br(H2O)12]- species interlocked with a bicyclic receptor. Each "water tetramer" is involved in coordinating the encapsulated bromide at both ends, resulting in a perfect C3 symmetric propeller-shaped bromide/water cluster. The specific orientation of the cryptand provides both directional H-bonds and an accurate spacing for water molecules to be coordinated with the central anion, resulting in a complementary host for the large hydrated bromide. Our results from both experimental studies and theoretical calculations clearly demonstrate that the formation of the stable [Br(H2O)12]- species is assisted by the hydrophobic environment of the host and efficient molecular recognition within the cavity via water$\cdots$amine3m and water$\cdots$anion7 interactions. This finding represents a prototype for new types of highly-ordered, anion/water hybrid clusters and a step towards the understanding of complex aqueous phase environments of an anion, particularly with large hydrophobic surroundings in biological systems.

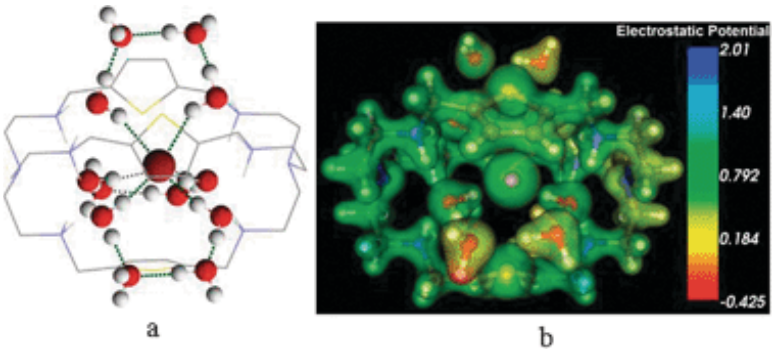

Figure 2.4. (a) Optimized DFT geometry of [H6L(Br(H2O)12)]5+ showing stabilization of the [Br(H2O)12]- guest with the cryptand at the M06-2X/6-31G(d,p) level of theory. (b) Electrostatic DFT potential of [H6L(Br(H2O)12)]5+ in PCM water solvent.

This page intentionally left blank.

Chapter 3

Comparison of Molecular Dynamics with Classical Density Functional and Poisson-Boltzmann Theories of the Electric Double Layer in Nanochannels

3.1 Introduction

The structure of the electric double layer (EDL) on a charged surface has long been modelled using the Poisson-Boltzmann (PB) theory. PB incorporates Coulombic interactions among charged particles but treats them as point charges, neglecting their finite size. Although this omission is relatively unimportant at low charge densities, it permits physically unrealistic ion packing densities when the surface potential and charge density become large, as occurs for example in energy storage applications [15]. To treat this deficiency, a number of modified PB theories have been devised over the years [105] and have met with some success, though they lack the fundamental foundation needed to accommodate a broad range of molecular interactions.

Molecular dynamics (MD) simulation provides the most fundamental and flexible platform for analysis of molecular interactions. As such, it has been used rather extensively in modelling of electro-osmotic flow (EOF) [27, 75, 94, 76, 49, 111] and to treat the higher charge densities of importance in EDL capacitors [17, 24, 103]. However, MD simulations entail considerable computational cost, making them impractical for treatment of time and length scales found in many applications. Difficulties also arise in applying boundary conditions and in computing long-range Coulombic interactions. For these reasons, alternative methods are still sought.

Alternative methods include modified PB approaches, integral equation methods, and classical Density Functional Theory (c-DFT). c-DFT, sometimes referred to as fluids DFT, yields the time-mean density distributions of molecular species that minimize a free energy functional [96, 91, 90, 70, 106, 34]. The free energy at any point is defined by a density weighted integration of molecular pair-potentials over the surroundings. Thus, c-DFT and MD are readily comparable given the same pair-potentials and input parameters. Unlike MD, however, c-DFT readily incorporates long-range Coulombic interactions as the product of ion charge with the electric potential obtained by

This chapter was originally published in [59].

solving Poisson's equation. In addition, the c-DFT formalism yields an expression for the chemical potential in terms of pair-potential integrals over the surrounding field. This chemical potential can be incorporated into existing finite element models of steady and transient transport processes, thus facilitating the introduction of atomistic physics into efficient multiscale models. Finally, c-DFT computing times are far shorter than those required for MD.

Validation of c-DFT for EDL applications has been ongoing for the past twenty years; it has encompassed a broad range of variants on the basic methodology and has been largely quite successful [91, 90, 70, 106]. However, these past validations are largely limited to comparisons between c-DFT and Monte Carlo (MC) simulations for the so-called primitive model (PM), in which the ions have defined charge and finite size but the solvent is treated as a background continuum defined only by its dielectric constant. Two exceptions to this are the studies by Goel *et al.* [35, 36] and Lamperski and Zydor [53] which compare c-DFT with MC for a non-primitive three component model (3CM), in which the solvent and ions are all treated as distinct molecular species differing in charge and size. However, all of these comparisons with MC simulations treat the ions as hard spheres and the charged surface as a hard wall.

Unlike those previous studies, the present paper compares c-DFT with MD results for the 3CM. In further contrast with prior work, 12-6 Lennard-Jones interactions among all species are included, and the wall interaction is modelled by the one-dimensional Lennard-Jones 10-4-3 potential, as these are more realistic and more compatible with MD practice than hard interactions. In addition, the present comparisons are extended to considerably greater charge densities than previously explored, reaching into a range relevant to energy storage.

We view these increases in complexity and range of the EDL model as a first step toward validation of c-DFT in a more realistic setting. This step is in the direction of the more general MD studies of EOF [27, 75, 94, 76, 49, 111] which also include the additional complexity of polar solvents, atomistically structured walls, and cross flow. An added complication for EOF is the apparent enhanced visocity within the EDL [111]. In our earlier effort to model EOF [67], we achieved favorable velocity-profile comparisons with MD simulation [75] by assuming a uniform viscosity, and even better results when applying the modified Chapman-Enskog model for density-dependent viscosity [10]. Comparison with EOF results is also hindered by absence of knowledge regarding a reference state or chemical potential that is typically needed for comparison with c-DFT. In order to directly extract that information, the reference state (adjoining reservoir or bulk fluid in this case) must be explicitly modelled. Otherwise those properties must be inferred via other means, such as the Widom insertion method for the chemical potential [108]. In addition, previous MD simulations of the EDL [27, 75, 94, 76, 49, 111, 24, 89, 16, 113, 110] have generally dealt with large ion concentrations and low surface charge densities, hence narrow EDLs with a single dominant "Stern layer" peak more nearly consistent with PB theory. In the current work, MD simulations were performed for a large range of ion concentrations and for surface charge densities many times greater than is typical of EOF. In most cases, the bulk region can be clearly distinguished, thereby revealing the reference state needed for comparison with c-DFT.

For the results of this paper, agreement between c-DFT and MD is deemed excellent, though it degrades somewhat with increasing charge density. The following three sections describe the details for PB, c-DFT simulations, and MD simulations. This is followed by a discussion of the

results and concluding remarks.

3.2 PB Theory

Here, we provide an overview of the classical PB theory. While it is understood that modified PB theories exist and provide improved model predictions[52], we choose to compare specifically with the classical standard since it is still in widespread use. Moreover, the classical result provides model validation for a specific regime, which will be discussed in more detail later in the paper.

In the PB formulation, ions near the wall form according to the Boltzmann distribution. The first order approximation for the electrolytes is expressed as:

$$n_+ = n_+^o \exp\left(\frac{-\phi\, e}{k_B T}\right) \qquad \text{and} \qquad n_- = n_-^o \exp\left(\frac{\phi\, e}{k_B T}\right). \tag{3.1}$$

n is the concentration of the ion species, the superscript o denotes the bulk value, ϕ is the local value of the total electric potential (relative to the bulk value), e is the elemental charge value, k_B is the Boltzmann constant, and T is the temperature. The summation of the two densities is the volume density of ionic charge, ρ. For a 1:1 electrolyte, i.e. $n^o = n_+^o = n_-^o$, ρ is then given by

$$\begin{aligned} \rho(\phi) &= n^o e\left[\exp\left(\frac{-\phi\, e}{k_B T}\right) - \exp\left(\frac{\phi\, e}{k_B T}\right)\right] \\ &= -2n^o e \sinh\left(\frac{\phi\, e}{k_B T}\right). \end{aligned} \tag{3.2}$$

The 1D Poisson equation [73] is

$$\frac{d^2\phi}{dz^2} = \frac{2n^o e}{\varepsilon} \sinh\left(\frac{\phi\, e}{k_B T}\right). \tag{3.3}$$

Multiplying both sides by $2\,(d\phi/dz)$ gives

$$\frac{d}{dz}\left(\frac{d\phi}{dz}\right)^2 = \frac{4n^o e}{\varepsilon} \sinh\left(\frac{\phi\, e}{k_B T}\right)\frac{d\phi}{dz}. \tag{3.4}$$

Integrating both sides from a point with zero potential (i.e. in the bulk) to some point at a finite potential (i.e. in the double layer, $z > d$) yields

$$\begin{aligned} \int_{\phi'=0}^{\phi'=\phi(z)} d\left(\frac{d\phi'}{dz}\right)^2 &= \int_{\phi'=0}^{\phi'=\phi(z)} \frac{4n^o e}{\varepsilon} \sinh\left(\frac{\phi'\, e}{k_B T}\right) d\phi' \\ \left(\left.\frac{d\phi'}{dz}\right|_{\phi'=\phi(z)}\right)^2 - \left(\left.\frac{d\phi'}{dz}\right|_{\phi'=0}\right)^2 &= \frac{4n^o k_B T}{\varepsilon} \cosh\left(\frac{\phi'\, e}{k_B T}\right)\Bigg|_{\phi'=0}^{\phi'=\phi(z)}. \end{aligned} \tag{3.5}$$

Following the application of the Neumann boundary condition for the bulk, the result becomes

$$\frac{d\phi(z)}{dz} = -\frac{2\kappa k_B T}{e}\sinh\left(\frac{\phi(z)\,e}{2k_B T}\right), \tag{3.6}$$

where $\kappa \equiv \sqrt{\frac{2n^o e^2}{\varepsilon k_B T}}$ is the inverse Debye length. After a separation of variables, a second integration from the wall to a point in the double layer ultimately leads to

$$\phi(z) = \frac{4k_B T}{e}\tanh^{-1}\left(\tanh\left(\frac{\phi_w\,e}{4k_B T}\right)\exp\left[-\kappa(z-d)\right]\right), \tag{3.7}$$

where ϕ_w is the total electric potential evaluated at the wall-fluid interface. Inserting Equation 3.7 back into the ionic charge density equation, Equation 3.2, yields the charge density as a function of position. Integrating the ionic charge density over all space yields the applied surface charge density.

3.3 c-DFT Simulations

In c-DFT, the equilibrium density distributions, $\rho_i(\mathbf{r})$, of multiple molecular species are determined by minimizing the grand potential energy, Ω, of the system [96, 91, 90, 70, 106, 34],

$$\Omega\left[\{\rho\}\right] = \sum_i \int \rho_i(\mathbf{r})\left(f_i(\mathbf{r}) - \mu_i\right) d\mathbf{r}. \tag{3.8}$$

Here, $f_i(\mathbf{r})$ is the Helmholtz free energy per molecule of the ith species, μ_i is the corresponding chemical potential, and the integral extends over the three dimensional domain of interest. The curly braces on ρ denote the set of unknown equilibrium density distributions. Here, we utilize a version of c-DFT developed at the University of Minnesota by Davis, Scriven, and colleagues [96, 91, 90]. In particular, our EDL calculations will utilize the 3CM in which the two ion species are represented as centrally charged spheres and the solvent molecules are treated as neutral spheres [90, 35, 53]. Electrostatic interactions arising from the solvent molecules are represented by the dielectric constant of the solvent, presumed to be spatially uniform.

The free energy consists of contributions from ideal gas behavior, the external potential field, $v(\mathbf{r})$, excess hard sphere repulsions, Lennard-Jones attractions [47], Coulombic forces, and short range electrostatic interactions evaluated using the Mean Spherical Approximation (MSA) of Waisman and Lebowitz [101, 102]:

$$f_i(\mathbf{r}, \{\rho\}) = f_i^{ig} + v(\mathbf{r}) + f_i^{hs} + \frac{1}{2}\left(f_i^{LJ} + f_i^{Coul} + f_i^{MSA}\right). \tag{3.9}$$

The ideal gas component depends on the local species density, temperature, deBroglie wavelength, Λ_i, and Boltzmann's constant:

$$f_i^{ig}\left(\rho_i(\mathbf{r})\right) = k_B T\left[\ln\left(\Lambda_i^3 \rho_i(\mathbf{r})\right) - 1\right]. \tag{3.10}$$

The external field, $v(\mathbf{r})$, is the non-electrical portion of the potential field induced by the solid walls. In most of the calculations presented here, $v(\mathbf{r})$ is obtained by integration of a Lennard-Jones potential over planar sheets of wall atoms. The integration [60] leads to the LJ 10-4-3 potential of the form:

$$v(z) = 2\pi\varepsilon^{LJ}\left[\frac{2}{5}\left(\frac{d}{z}\right)^{10} - \left(\frac{d}{z}\right)^{4} - \frac{\sqrt{2}d^3}{3\left(z+\left(0.61/\sqrt{2}\right)d\right)^3}\right], \tag{3.11}$$

where d is the LJ diameter and z is the wall-normal position measured from the wall. Note that the potential is a one-dimensional potential and is therefore a function of z, and not the general position, $\mathbf{r}$. The potential is cut off outside of 3.5 molecular diameters and shifted by subtracting the value at the cutoff.

Hard sphere exclusions of liquid molecules, modelled by f_i^{hs}, are included to avoid integration of self-interactions. The excess free energy is based on the following formula derived from the Carnahan-Starling equation of state:

$$f_i^{hs}\left(\bar{\rho}(\mathbf{r})\right) = k_B T \eta \frac{4-3\eta}{(1-\eta)^2}, \qquad \eta = \bar{\rho}\frac{\pi d_{hs}^3}{6}. \tag{3.12}$$

The normalized mean density, η, appearing here represents the volume fraction occupied by molecules having a hard sphere diameter d_{hs}. The local mean density, $\bar{\rho}(\mathbf{r})$, used in calculating these repulsions is a weighted average over the surrounding fluid,

$$\bar{\rho}(\mathbf{r}) = \int \left[\omega^0(s) + \omega^1(s)\bar{\rho}(\mathbf{r}) + \omega^2(s)\bar{\rho}^2(\mathbf{r})\right]\rho(\mathbf{r}')d\mathbf{r}'. \tag{3.13}$$

The weight functions, $\omega^k(s)$, are chosen in accordance with a third-order scheme derived by Tarazona [92]; a corrected version is given by Vanderlick, Scriven, and Davis [96]. The weighting functions are prescribed as:

$$\omega^0(s) \equiv \begin{cases} \frac{3}{4\pi d^3}, & s < d, \\ 0, & s > d, \end{cases} \tag{3.14a}$$

$$\omega^1(s) \equiv \begin{cases} 0.475 - 0.648\left(\frac{s}{d}\right) + 0.113\left(\frac{s}{d}\right)^2, & s < d, \\ 0.288\left(\frac{d}{s}\right) - 0.924 + 0.764\left(\frac{s}{d}\right) - 0.187\left(\frac{s}{d}\right)^2, & d < s < 2d, \\ 0, & s > 2d, \end{cases} \tag{3.14b}$$

$$\omega^2(s) \equiv \begin{cases} \frac{5\pi d^3}{144}\left[6 - 12\left(\frac{s}{d}\right) + 5\left(\frac{s}{d}\right)^2\right], & s < d, \\ 0, & s > d, \end{cases} \tag{3.14c}$$

where $s = \left|\mathbf{r} - \mathbf{r}'\right|$ is the relative atomic position. Here we will assume that all molecular species have the same diameter, d_{hs}, thus permitting the local summation of all species into the total densities, $\rho(\mathbf{r})$, used in computing $\bar{\rho}(\mathbf{r})$.

Attractive energies are defined by a density weighted integral of a pair potential function, $U_{ij}(s)$, over the surrounding fluid, separately summing the contributions from each species,

$$f_i^{LJ}(\mathbf{r},\{\rho\}) = \sum_j \int \rho_j(\mathbf{r}')U_{ij}(s)d\mathbf{r}'. \tag{3.15}$$

Although the LJ 12-6 potential is used in nearly all c-DFT modelling, authors differ in how they extract the attractive part. We follow one common approach by splitting the potential at its crossover point, $s = d$, and cutting it off at $s = s_{max} = 3.5d$.

$$U_{ij}(s) = 4\varepsilon_{ij}^{LJ}\left[\left(\tfrac{d}{s}\right)^{12} - \left(\tfrac{d}{s}\right)^{6}\right] \qquad \text{for} \quad d \le s \le s_{max} \tag{3.16}$$

Outside this interval, $U = 0$. To avoid a slight discontinuity in U_{ij} at $s = s_{max}$, this truncated function is shifted by subtracting $U_{ij}(s_{max})$.

Coulombic contributions to the free energy are computed as the product of the molecular charge, $q_i = ez_i$, with the local electric potential, ϕ:

$$f_i^{Coul}(\mathbf{r}) = q_i\phi(\mathbf{r}). \tag{3.17}$$

The electric potential field is obtained by solving Poisson's equation [73],

$$\nabla^2\phi = -\frac{4\pi}{\varepsilon}\sum_{i=1}^{N} z_i e\rho_i, \tag{3.18}$$

in which ε is the permittivity of the liquid, e is the elementary charge, and z_i is the number of charges per molecule.

The free energy associated with short range electrostatic interactions is modelled using MSA [101, 102]

$$f_i^{MSA}(\mathbf{r},\{\rho\}) = \sum_j \int \rho_j(\mathbf{r}')\Delta c_{ij}(\mathbf{r}-\mathbf{r}')d\mathbf{r}', \tag{3.19}$$

$$\Delta c_{ij} = \tfrac{q_i q_j}{\varepsilon}\left[\tfrac{2B}{d} - \left(\tfrac{B}{d}\right)^2 s - \tfrac{1}{s}\right], \qquad s < d, \tag{3.20}$$

$$B = \tfrac{d^*+1-\sqrt{1+2d^*}}{d^*}, \qquad d^* = d/\lambda, \tag{3.21}$$

$$\lambda = \left[\frac{4\pi}{\varepsilon k_B T}\sum_i \rho_i q_i^2\right]^{-1/2}. \tag{3.22}$$

Here, λ is the Debye length which we evaluate using local values of the species densities in the manner suggested by Gillespie *et al.* [34] and Wang *et al.* [106], rather than using the reference densities that refer to the bulk reservoir fluid, as was done in most early implementations of MSA [91, 90]. The molecular diameter appearing here is taken as the exclusion diameter, d_{hs}.

By taking the variation of Ω with respect to $\rho_i(\mathbf{r})$ we obtain the following expression for the chemical potential of each species, applicable to all points, $\mathbf{r}$:

$$k_B T \ln \rho_i + v_i + f_i^{LJ} + f_i^{Coul} + f_i^{MSA} + f_i^{hs} + f_i^{hs2} = \mu_i. \tag{3.23}$$

The new term, f_i^{hs2}, arises from (Fréchet) functional differentiation of the nonlinear hard sphere repulsion term,

$$f_i^{hs2}(\mathbf{r}, \{\rho\}) = \int \bar{\rho}(\mathbf{r}) \frac{\partial f_i^{hs}}{\partial \rho_i}(\mathbf{r}') d\mathbf{r}'. \tag{3.24}$$

Numerical solutions to the preceeding integral equations are obtained on a discrete grid having a uniform spacing of $d/30$. All of the integrals appearing in the c-DFT equations are represented as weighted summations over the surrounding grid points. The weight factors in these summations are calculated by numerical quadrature prior to numerical solution, and these weights remain fixed unless the grid is redefined. Moreover, in the case of 1D c-DFT, integration over two of the three dimensions can be performed at the onset to obtain weights describing interactions between slabs of volume bounded by parallel planes defined by their distance from the planar electrode surfaces. Introduction of this discretization into Eqn 3.23 then yields an independent equation for each species density at each grid point. This system of nonlinear algebraic equations is then solved iteratively to obtain the equilibrium density field. For a 1-D system with channel width of $w = 10d$, iterative solutions to the resulting system of coupled nonlinear equations require about a minute of computing time on a single 3GHz Dual-Core Intel Xeon CPU processor to obtain five digit accuracy after 4000 iterations. The numerical quadratures and primitive iteration scheme are detailed in Ref. [92].

3.4 MD Simulations

MD simulations of a similar electrically charged nanochannel were performed with the LAMMPS software package [72]. Important to note is that the MD domain is sufficiently wide in the wall-normal direction so that the bulk fluid can be explicitly modelled to measure ion molarities, solvent density, and the electric potential. The simulation domain consists of the electrolyte fluid bounded in the z-dimension by LJ 10-4-3 walls, as discussed previously, and in the transverse directions with periodic boundary conditions. Transverse dimensions are 5 nm $\times$ 5 nm, and the longitudinal dimension varies depending on the bulk ion concentration. Interatomic potentials were modelled with the superposition of a typical LJ 12-6 potential with Coulomb's law, both with a 1.3 nm cutoff. The pairwise potential is an abrupt cutoff, contrary to c-DFT which is cut and shifted. Fluid-wall interactions are treated as described in the c-DFT section.

Equations of motion were integrated with the velocity-Verlet algorithm [97, 98] and a timestep of 0.0005 picoseconds (ps). The electrolyte fluid is comprised of positive, negative, and neutral LJ atoms, all with the same interaction parameters. The atoms are assigned a mass of 18.0154 grams per mole. To account for the dielectric effects of a polar solvent, the dielectric constant ε_r was set to 80 to approximate water [27, 94]. In general, polar solvent molecules will solvate ionic charges and prevent oppositely charged ions from approaching too closely. This can be mimicked by reducing

all Coulombic interactions by the value of the dielectric constant. Long range Coulombics are computed using the PPPM algorithm [42] with slab geometry [114].

To facilitate equilibration, the initial system contains only uncharged particles. The number of particles must be selected such that the final steady state configuration produces the correct bulk concentrations and densities. Note that this procedure requires some iteration to target the desired values, and it can be approximately informed by the steady state configuration from the c-DFT calculations or PB theory. The atom velocities are all initialized to zero since potential energy variations will cause the system kinetic energy to increase rapidly. This uncharged system is equilibrated to 300K for 100,000 timesteps using the Nosé-Hoover [69, 43, 61] thermostat. Following the initial equilibration, fluid particles are randomly selected and assigned positive or negative electric charges. The selection process fills each approximate EDL region with counterions and randomly assigns the rest of the ions to the remainder of the domain according to a uniform distribution. This produces a biased overall distribution aimed to expedite equilibration. A background electric field is applied to simulate equally and oppositely charged surfaces. The charged system is then equilibrated for 500,000 more timesteps to 300K. To avoid any local minima in the energy landscape, the system is annealed to 1000K for 500,000 timesteps, followed by a cooling step back to 300K for one million timesteps.

Following equilibration, thermostats are turned off. The system is allowed to evolve toward a steady state solution for five million timesteps. The first one million timesteps are treated as transient, and the remaining timesteps are confirmed to be statistically steady. Five permutations of this simulation are performed for each molarity and surface charge combination. The permutations differ in the initial configuration of atom positions. To increase sampling in the larger domain for 10mM, an additional five permutations are simulated, and each production run is shortened by one million timesteps. Not all molarity and surface charge combinations are tested due to computational difficulty in achieving good statistics for low ion counts and low surface charges.

Spatial dependent particle concentrations are extracted by species from the domain via an atomistic-to-continuum (AtC) interpolation method [117]. The resolution of the 1-D continuum mesh is approximately 0.1 Å. Density data is sampled every 0.25 ps. After removing the transient data, the remaining data is time- and ensemble-averaged. Species concentrations, scaled by the atomic charge, yield the spatially resolved free charge density, ρ_{free}. Integrating Poisson's equation,

$$\nabla \cdot (\varepsilon_0 \varepsilon_r \mathbf{E}) = \rho_{free}, \tag{3.25}$$

produces the z-component of the electric field. Note that, consistent with c-DFT, $\varepsilon_r = 80$ is assumed to be pervasive in this integration, regardless of the presence or absence of solvent. Furthermore, the electric field is offset by the applied field, which is also augmented by the relative permittivity. The electric potential can similarly be obtained by integrating the electric field:

$$-\nabla \phi = \mathbf{E}. \tag{3.26}$$

The bare wall potential, also known as the electric surface potential, is determined by taking the electric potential at the fluid-wall contact point in reference to the electric potential evaluated in the bulk; see Figure 3.4. For this study, the contact plane, not to be confused with the shear plane where

the Zeta Potential is measured, is defined to be one half-molecular diameter away from the LJ 10-4-3 origin, to be consistent with the c-DFT calculation. Moving the measurement location within the free space region will merely add a linear offset to the electric potential (linear with respect to the applied surface charge) since the amount of charge does not change. The ion molarities are also measured by taking the average density of the channel center.

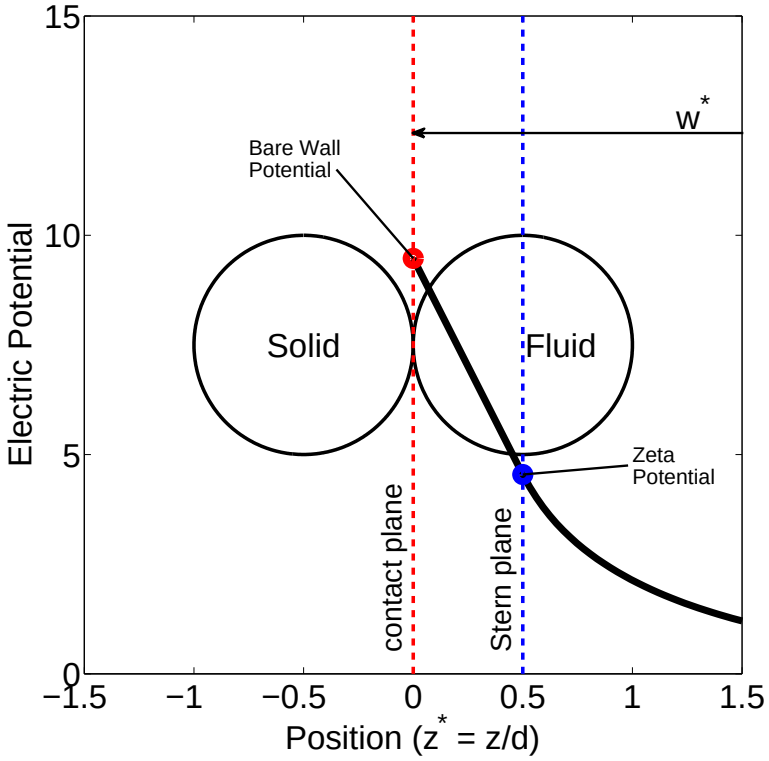

Figure 3.1. Diagram of zeta potential (blue) and bare wall potential (red), also known as the electric surface potential. Since finite atom sizes are foreign to PB theory, it makes no distinction between the two. The diagram also shows where the channel width, w^*, is measured from.

3.5 Results

Results are reported in terms of normalized position, $z^* = z/d$, channel width $w^* = w/d$, density $\rho^* = \rho d^3$, potential $\phi^* = \phi\ e/k_B T$, and surface charge $\sigma^* = \sigma d^2/e$. Parameters used in the EDL simulations are given in Table 3.1.

Bulk ion densities are varied from 1mM to 1M. The lower end of this range is typical of microscale chemical laboratory devices while the upper end applies to electrochemical energy storage

Parameter	c-DFT	MD
Atom-Atom ε^{LJ} (eV)	0.006596	0.006596
Atom-Atom d (Å)	3.1507	3.1507
Atom-Atom inner cutoff (Å)	2.9302	N/A
Atom-Atom outer cutoff (Å)	11.0275	13.0
Atom-Wall ε^{LJ} (eV)	0.1351	0.1351
Atom-Wall d (Å)	3.1507	3.1507
Atom-Wall outer cutoff (Å)	11.0275	11.0275
Relative Permittivity ε_r	80	80
Nominal Temperature (K)	300	300
Atomic Mass (g/mol)	N/A	18.0154

Table 3.1. Simulation parameters for c-DFT and MD calculations. The word "atom" is used to represent either a solvent or solute particle, as opposed to the LJ wall.

devices and desalination processes. Within this range of ion concetrations, the Debye thickness from PB theory λ decreases from approximately 97 to 3 Å or, equivalently, λ/d decreases from 30 to 1 with increasing concentration. Thus, to avoid excessive EDL overlap, we utilized a channel width of $w^* = 12.55$ for bulk concentrations of 100mM and 1M, but increased the width to $w^* = 100$ for the 10mM and 1mM runs. Note that these bulk ion concentrations refer to the state that would exist in a zero-potential reservoir of infinite extent in equilibrium with the charged channel. The same state would also be found at the center of a charged channel having a width much greater than the Debye thickness. For comparison purposes, the bulk of the MD domains is defined as the center $\sim$12 Å and $\sim$45 Å for the $w^* = 12.55$ and $w^* = 100$ channels, respectively, where the electric potential is observed to be relatively flat.

Channel widths quoted here represent the distance between the liquid/solid contact surfaces on opposite sides of the channels, as indicated in Figure 3.4. Similarly, the bare wall potentials reported here are measured at these same contact planes. Zeta potentials, by contrast, refer to the potential at the Stern plane: the center plane of the first layer of fluid molecules at a distance $d/2$ from the contact plane.

3.5.1 Preliminary Model Validation

Prior to the comparisons presented here, we had previously [67] used our c-DFT to replicate c-DFT results presented by Vanderlick *et al.* [96] and Tang *et al.* [90], as well as two of the MD simulations presented by Magda *et al.* [60].

As a prelude to the upcoming comparisons of our MD and c-DFT for the EDL, we performed an initial comparison of density profiles for a fluid confined between uncharged planar walls. The parameters are taken from an MC simulation by Snook and van Megen [88] for a channel width of 7.5 measured between the center planes of the first layers of wall atoms in the 10-4-3 LJ walls; this is a width of 6.5 between fluid/solid contact planes. The LJ energies for the fluid-fluid and fluid-solid interactions are both taken as $\varepsilon^{LJ}/k_BT = 0.833$ and the chemical potential is $\gamma/\varepsilon^{LJ} = -2.477$, which corresponds to a bulk fluid having a normalized density of $\rho^* = 0.5925$. Since the authors reported the number of fluid molecules in their MC simulations, we used this to guide the number needed in our MD.

Figure 3.2 compares Snook's MC and our MD with our c-DFT results for two different choices of the hard sphere diameter. The c-DFT result for $d_{hs} = d_{LJ}$ (dotted lines) has a spacing between molecular layers slightly greater than that of the MD and the MC simulations. This mismatch is corrected by the use of $d_{hs} = 0.93 d_{LJ}$ in the c-DFT calculation indicated by the solid line. This adjustment, similar in concept to the Barker-Henderson diameter [8], helps to align the spacing while having negligible influence on the magnitude of the density peaks. Thus, we make this adjustment of spacing mainly to facilitate the upcoming comparisons between c-DFT and MD for the EDL.

3.5.2 Comparison of c-DFT and MD Simulation of EDL

Figure 3.3 provides an overview comparison of computed surface potential versus surface charge density among our MD, our c-DFT, and classical PB modelling. This is a very important metric as the inverse slope of this plot is the capacitance. Since $k_BT/e \approx 25$mV, the upper range of the potential slightly exceeds 1V, typical of double layer capacitors.

MD results (symbols) are shown for three charge densities (0.44, 0.88, and 1.75) and for bulk concentrations of 10mM, 100mM, and 1M. Additional charge densities (0.22, 0.66, 1.32) are included for 1M. The agreement between MD and c-DFT is judged as excellent for 1M but degrades moderately at the lower concentrations. MD results are not included for 1mM due to the statistical difficulty in obtaining convergence of the very low ion densities in the channel center.

The classical PB results shown in Figure 3.3 are obtained by application of the Grahame equation [38] which is strictly applicable only to a semi-infinite medium,

$$\sigma^{*^2} = \frac{\rho_B^*}{\pi P}\left[\cosh\left(z\phi_w^*\right) - 1\right], \tag{3.27}$$

where $\rho_B^* = C_B A d^3$, $C_B A$ is the bulk ion concentration in ions/Å^3 (molarity $\times$ Avogadro's number $\times\ 10^{-27}$), and $P = e^2/4\pi\varepsilon k_B T d$ is the plasma constant. Thus, the very precise agreement in electric surface potential between MD/c-DFT with PB at low charge density is an indication that our channel widths are sufficiently large to minimize the effects of EDL overlap. Also, such a precise agreement at low charges might not have been anticipated given that the layered density profiles of c-DFT and MD differ greatly from their smooth PB counterparts. Most importantly, it is seen that the PB substantially deviates from MD/c-DFT at charge densities of 0.5 or greater.

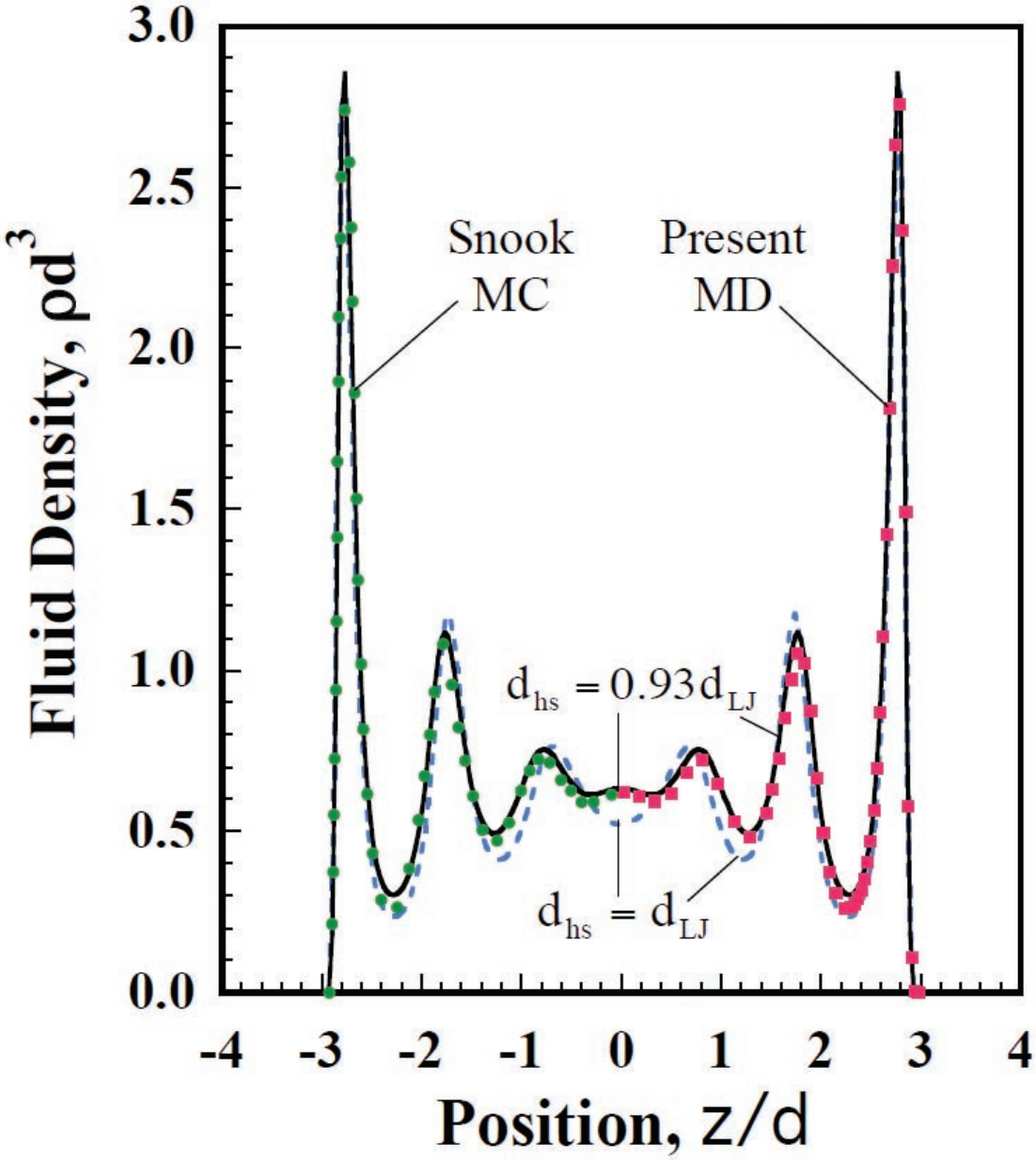

Figure 3.2. Snook MC (green circles) and present MD (red squares) compared to c-DFT (solid and dashed lines) with different choices of the hard sphere diameter, d_{hs}, relative to LJ diameter, d_{LJ}.

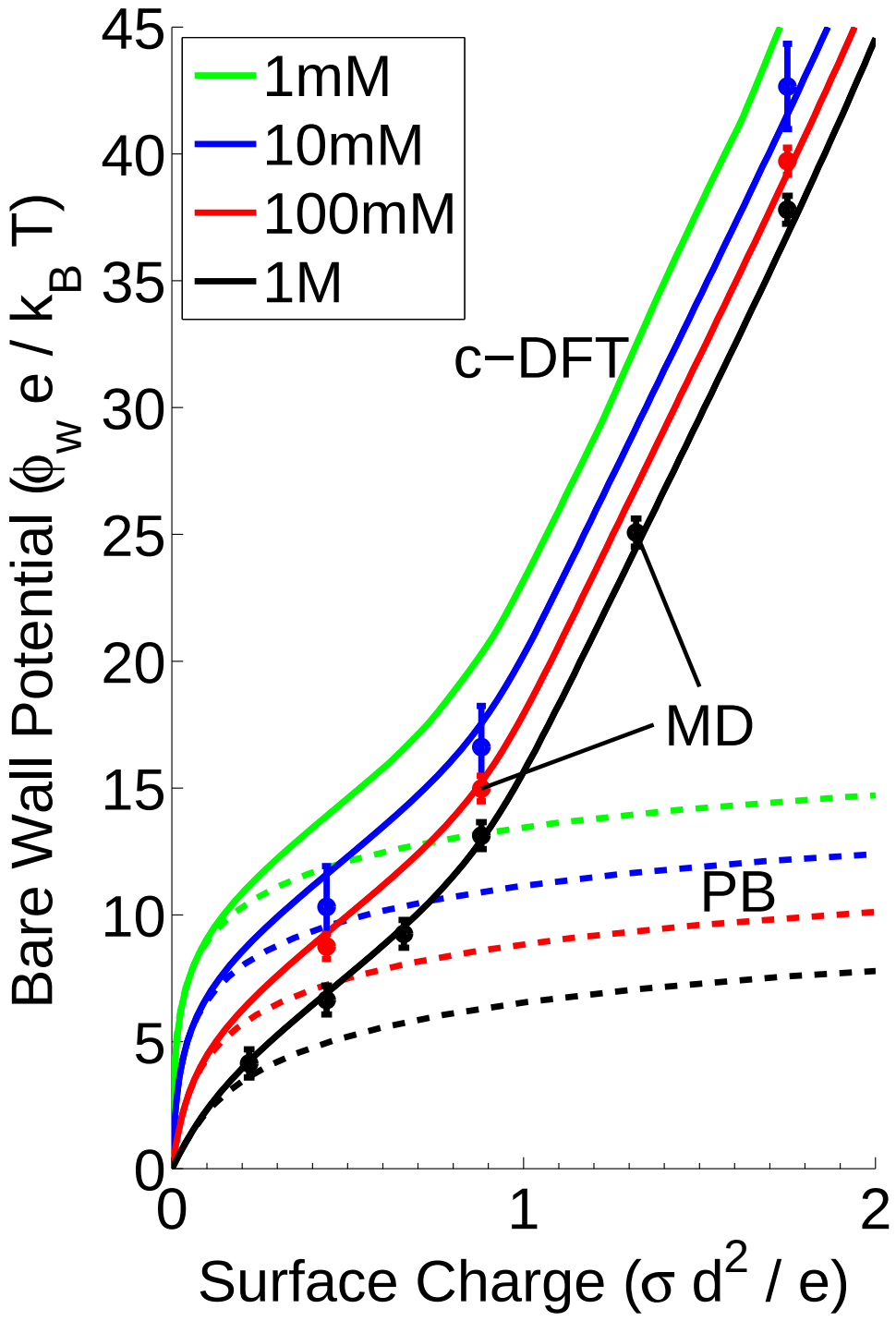

Figure 3.3. Capacitance comparison of three EDL models. MD is shown with circle markers and error bars which denote the standard deviation of the dataset. c-DFT is shown with solid lines, and PB is shown with dashed lines. Colors denote bulk ion molarities, as shown in the legend.

In an effort to find a fairer comparison to the PB, we tried two alternatives. In the first of these attempts, we treated the bare wall potential of the PB as though it were a zeta potential and used the surface slope to extrapolate backward by $d/2$ to the corresponding bare wall location (see Figure 3.4). This produced a PB that rose much faster than the c-DFT/MD. As a second alternative, we compared the bare wall potential of the PB with the zeta potential of the c-DFT. This reduces the disparity between c-DFT/MD and PB at large surface charges since the zeta potential of the c-DFT/MD increases far more slowly than the bare wall potential, but such a comparison still involves substantial error.

Example concentration profiles for three charged cases are shown in Figures 3.4a, 3.5a, and 3.6a. All three examples are targeted to a 100mM ion solution with varying surface charge loadings. Corresponding MD and c-DFT solutions are overlaid to show the agreement. Since populating the MD domain to a corresponding c-DFT case is a complex inverse problem, the MD models used as inputs: integrated solvent and solute density profiles, and surface charge density outputs from the c-DFT simulations. Since agreement is good between the two models, this method produces nearly analogous cases for comparison. An additional c-DFT iteration to match the MD is also done in some cases. The left hand side of Figures 3.4a-3.6a show the concentration profiles on a linear scale, distinguished by atom types. The right side of the figures are the analogous plots displayed on a logarithmic scale to showcase good agreement even over five to six decades.

The peak heights and widths appear to differ slightly between the two models, particularly near the wall. c-DFT tends to have broader, shorter peaks while the MD has narrower, tall peaks. This is especially noticable in the first two layers in Figure 3.6.

The particle density profiles are multiplied by the atom types' respective valences to obtain a charge density profile, which is shown in the top graph in Figures 3.4b, 3.5b, and 3.6b. The second and third plots correspond to the density profile once- and twice- integrated to obtain the z-component electric field and electric potential, respectively. The results from the two models are overlaid again in these plots, and the agreement is shown to be quite good. Even despite the slight mismatch in peak values observed in Figures 3.4a, 3.5a, and 3.6a, the integrals seem to converge to similar solutions. This is a result of having an equal amount of charge per layer, only differing in the mobility of the atoms within those layers.

3.5.3 Sequential Layer Charging Phenomenology

Charging of the EDL proceeds largely as a sequential layer-by-layer displacement of solvent molecules by counterions, as illustrated in Figure 3.7 with c-DFT results at 10mM. Similar results were observed in the MD, particularly at higher concentrations. As seen in the inset density profiles for $\sigma^* = 1.0$, all of the solvent has been displaced from the first layer prior to the formation of a second layer of counterions. With increasing surface charge density, the counterion density peaks in the first and second layers both continue to increase in height and narrow in width until all of the solvent has been excluded from the second layer, as seen in the inset for $\sigma^* = 2.1$. The third stage of the process continues in a similar fashion until all of the solvent has been displaced from

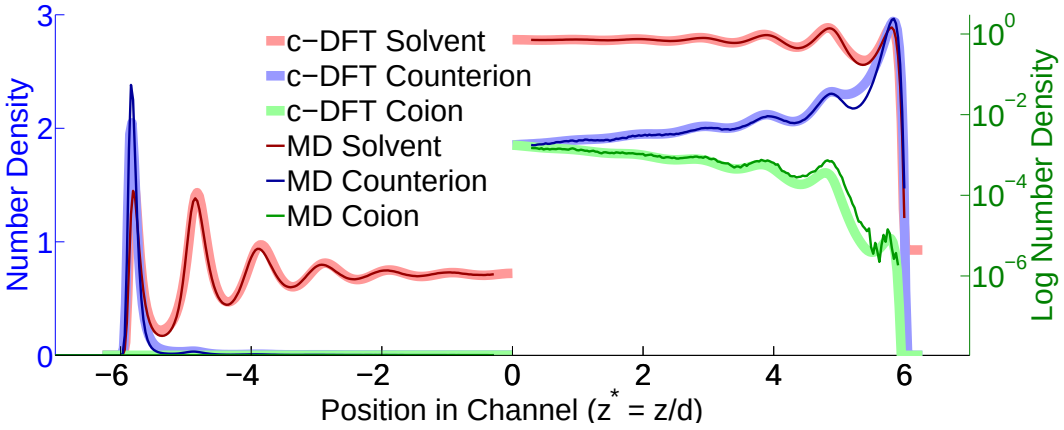

(a) Number density profiles on linear and logarithmic scales

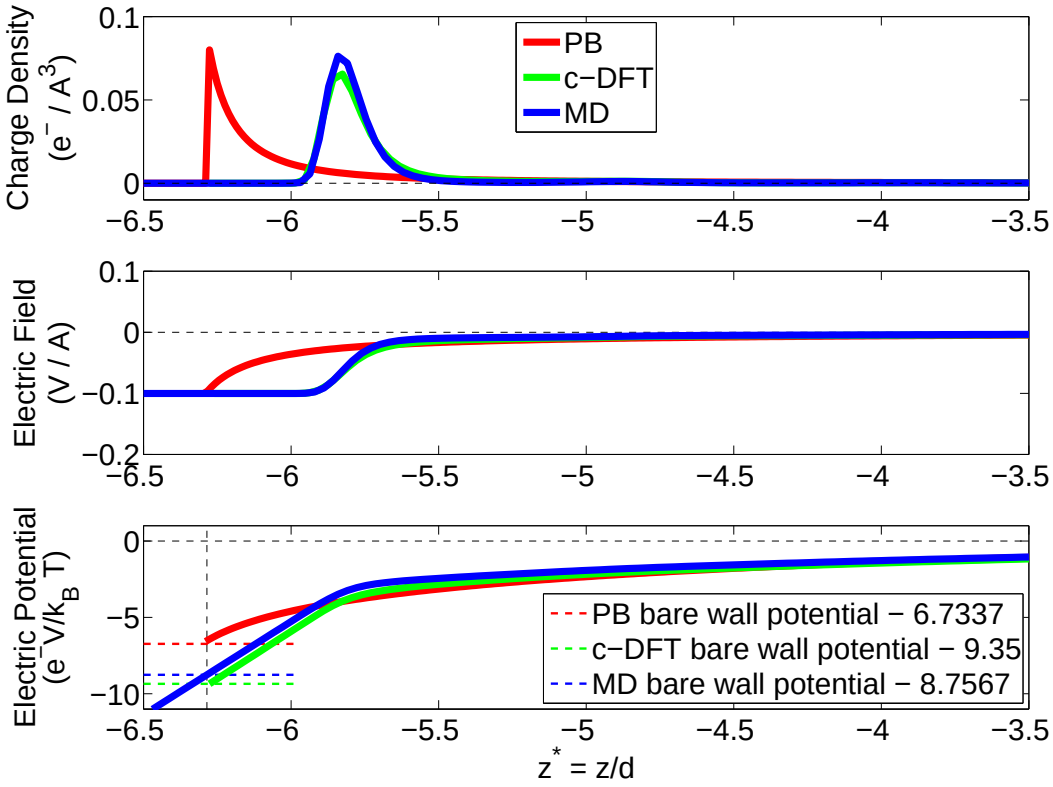

(b) Charge density, electric field, and electric potential comparison of MD/c-DFT/PB

Figure 3.4. MD/c-DFT EDL comparison for 0.44 normalized surface charge. Electryolyte concentration is 93.239mM (100mM target). Bulk solvent density, normalized by d^3, is 0.71711 (0.7 target).

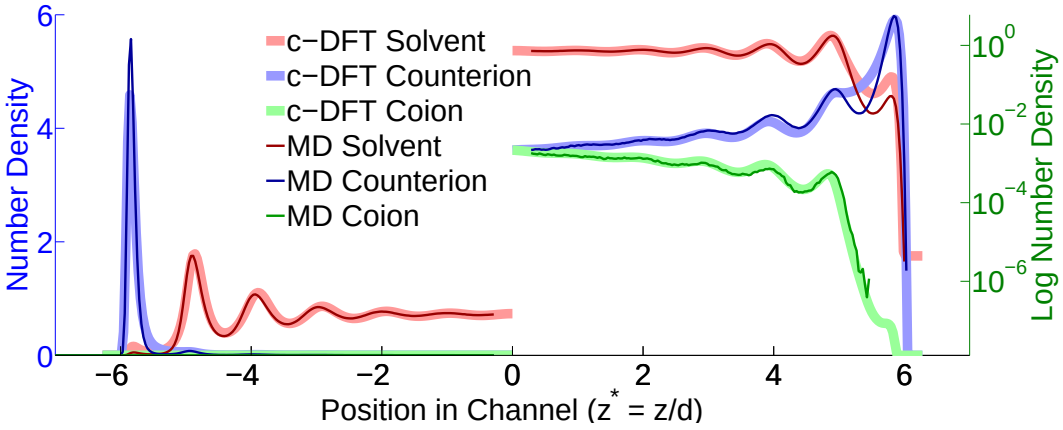

(a) Number density profiles on linear and logarithmic scales

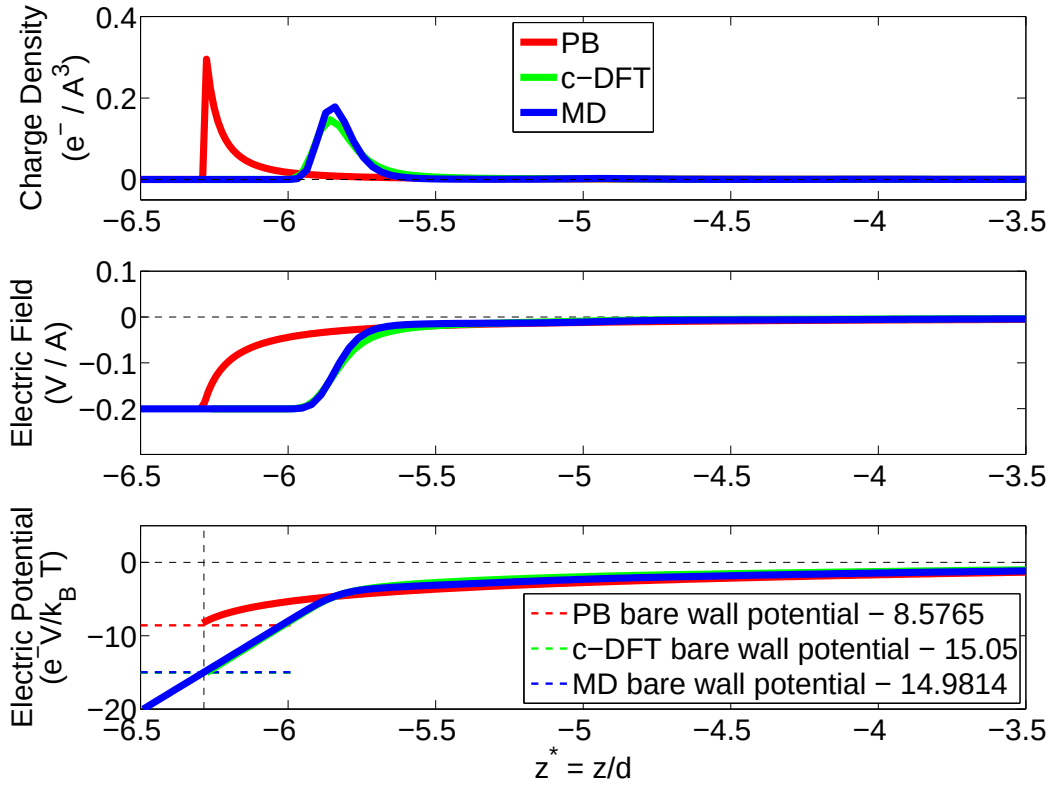

(b) Charge density, electric field, and electric potential comparison of MD/c-DFT/PB

Figure 3.5. MD/c-DFT EDL comparison for 0.88 normalized surface charge. Electryolyte concentration is 113.45mM (100mM target). Bulk solvent density, normalized by d^3, is 0.72227 (0.7 target).

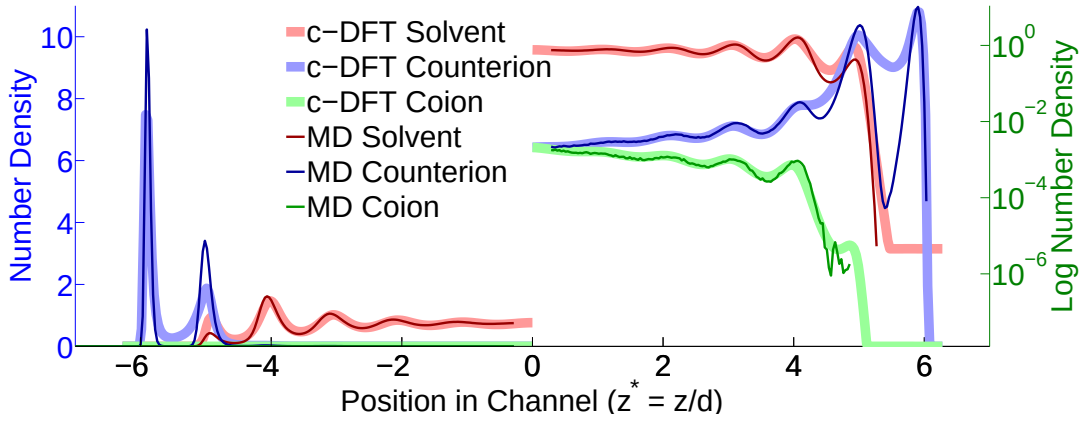

(a) Number density profiles on linear and logarithmic scales

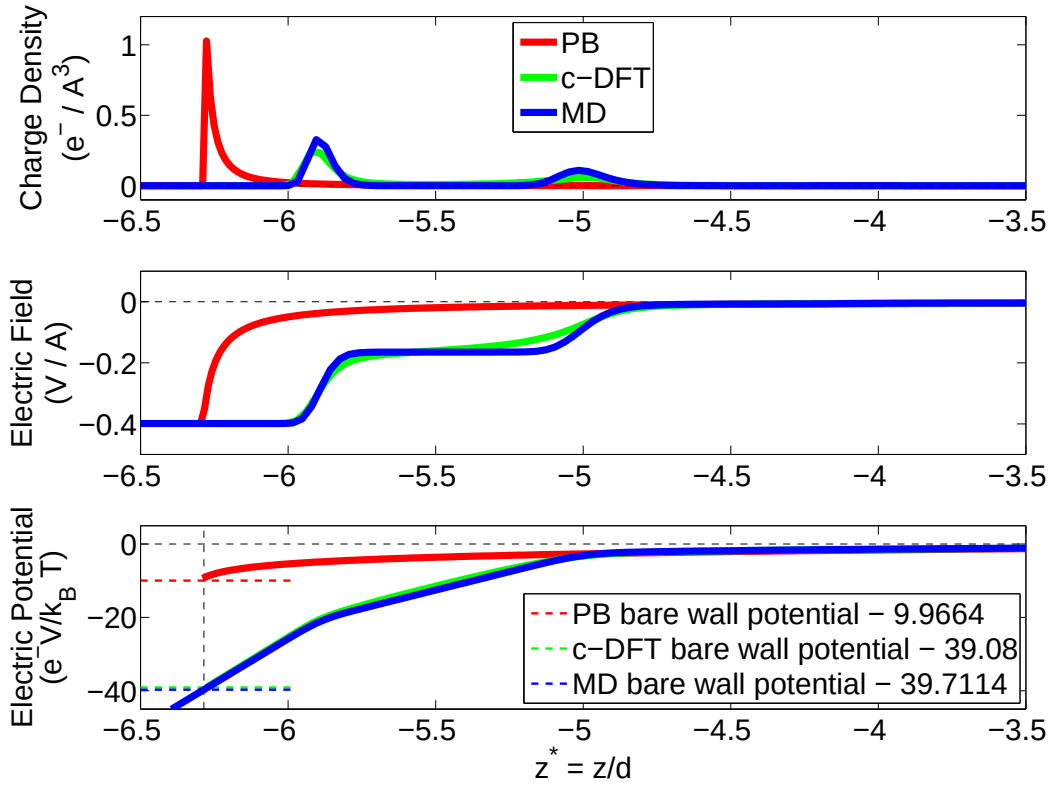

(b) Charge density, electric field, and electric potential comparison of MD/c-DFT/PB

Figure 3.6. MD/c-DFT EDL comparison for 1.75 normalized surface charge. Electryolyte concentration is 107.59mM (100mM target). Bulk solvent density, normalized by d^3, is 0.74146 (0.7 target).

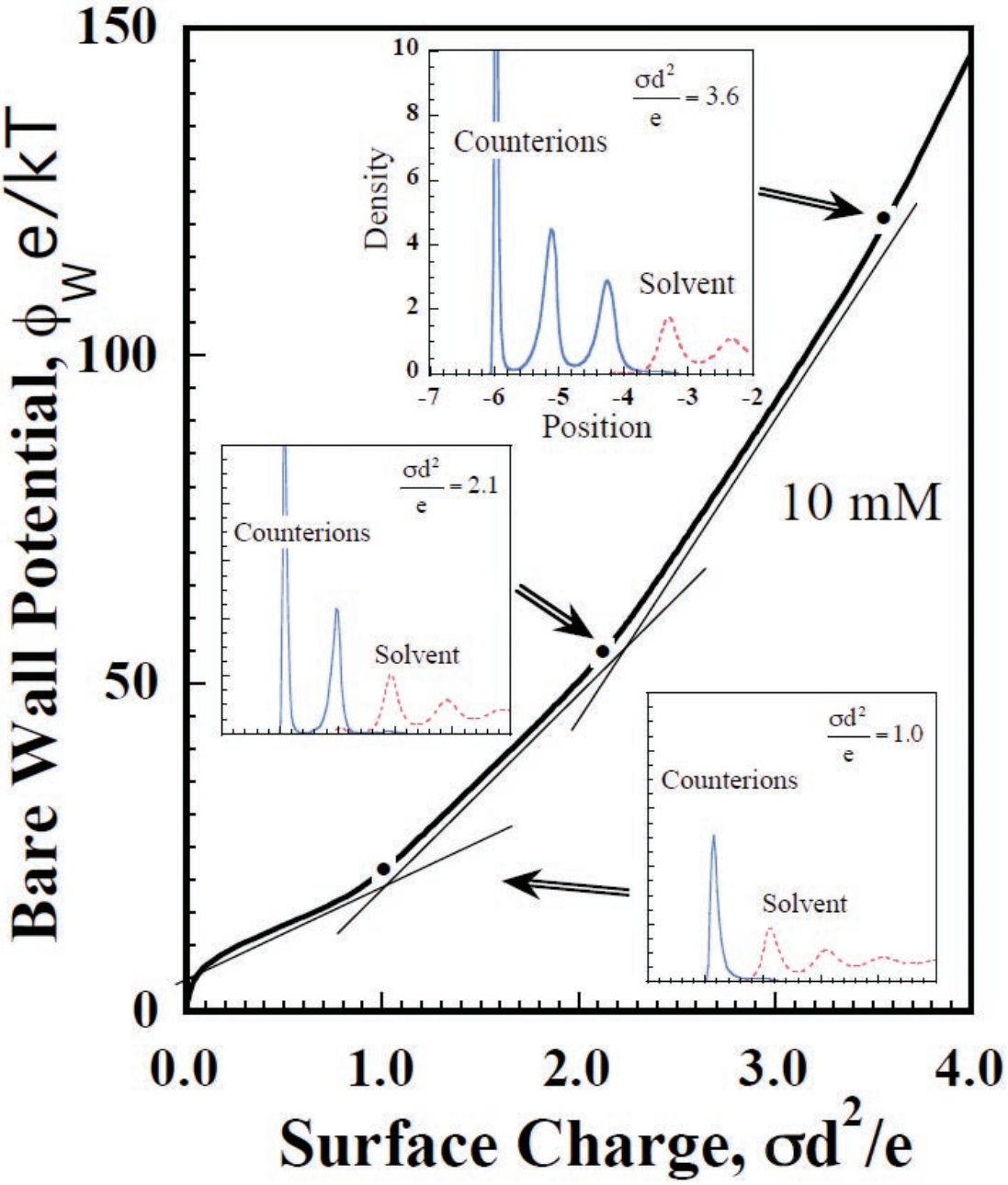

Figure 3.7. Layer filling phenomenology. Aside from initial non-linear behavior, the capacitance trend is a nearly piecewise linear function. Inflection points correspond to solvent depletion from subsequent near-wall layers, as depicted in the figure insets.

the third layer at $\sigma^* = 3.6$.

Another interesting feature of this step-like layer filling process is that each stage proceeds with a nearly constant capacitance, as indicated by a constant slope in Figure 3.7. The transition from one stage to the next is smooth but most of the charging occurs as a piecewise linear process with the slope increasing (and the capacitance decreasing) with each successive stage. This seems physically reasonable, as it becomes more difficult to accumulate charge in layers more remote from the surface. However, this interpretation does not appear to apply in the initial charging of the first layer which begins with a very steep slope (small capacitance) before turning off onto a much flatter, nearly constant slope. The initial non-linear phase occurs because ionic charges are relatively evenly distributed through the EDL for low surface charges. As loading increases, peak formation becomes energetically favorable, and most of the charge is found distributed near the walls, as shown in Figure 3.8. As the peak builds up (likewise for subsequent layers), the peak-structure's contributions begin to dominate those of the tail. Aside from the initial non-linear phase, these features of the charging behavior are expressly absent from theories not accounting for finite size effects since the physics arise from layered density profiles and solvent displacement processes entirely foreign to PB.

3.5.4 MSA Treatments Leading to Charge Inversion

In MSA formulations of c-DFT, the Mean Spherical Approximation of Waisman and Lebowitz [101, 102] is used to solve the Ornstein-Zernike equation relating the radial distribution functions and direct correlation functions of ion species. The resulting pair interactions can then be partitioned into a direct Coulombic contribution, a hard sphere repulsion, and an electric residual contribution with the latter given by our Eqns 3.19-3.22 [106]. Historically, the Debye length appearing in Eqn 3.19 had been evaluated using the ion concentrations of the bulk state existing within the center of a very wide channel or within an external reservoir, referred to here as the MSA_B approach. This was traditionally done, in part at least, to ensure electrical neutrality of the reference state since the MSA theory is derived as a perturbation about a neutral reference state. The expectation of the perturbation approximation is that the final result is a small correction to the reference. Given that large density variations occur near the walls, the perturbation ansatz can not be expected to work. More recent MSA implementations by Gillespie *et al.* [34] and Wang *et al.* [106] have used a local, non-uniform fluid as the reference state, as opposed to the bulk fluid. Because local ion concentrations are not electrically neutral, these authors defined an equivalent charge-neutral reference state having the same ionic strength as the local state. Thus, denoting reference densities with the subscript "ref," a pair of ion densities must satisfy the requirements that

$$\rho^+_{\text{ref}} + \rho^-_{\text{ref}} = \rho^+ + \rho^-, \tag{3.28}$$

$$\rho^+_{\text{ref}} \left(q^+\right)^2 + \rho^-_{\text{ref}} \left(q^-\right)^2 = \rho^+ \left(q^+\right)^2 + \rho^- \left(q^-\right)^2. \tag{3.29}$$

For the present univalent examples, the net result is that

$$\rho^+_{\text{ref}} = \rho^-_{\text{ref}} = \left(\rho^+ + \rho^-\right)^2. \tag{3.30}$$

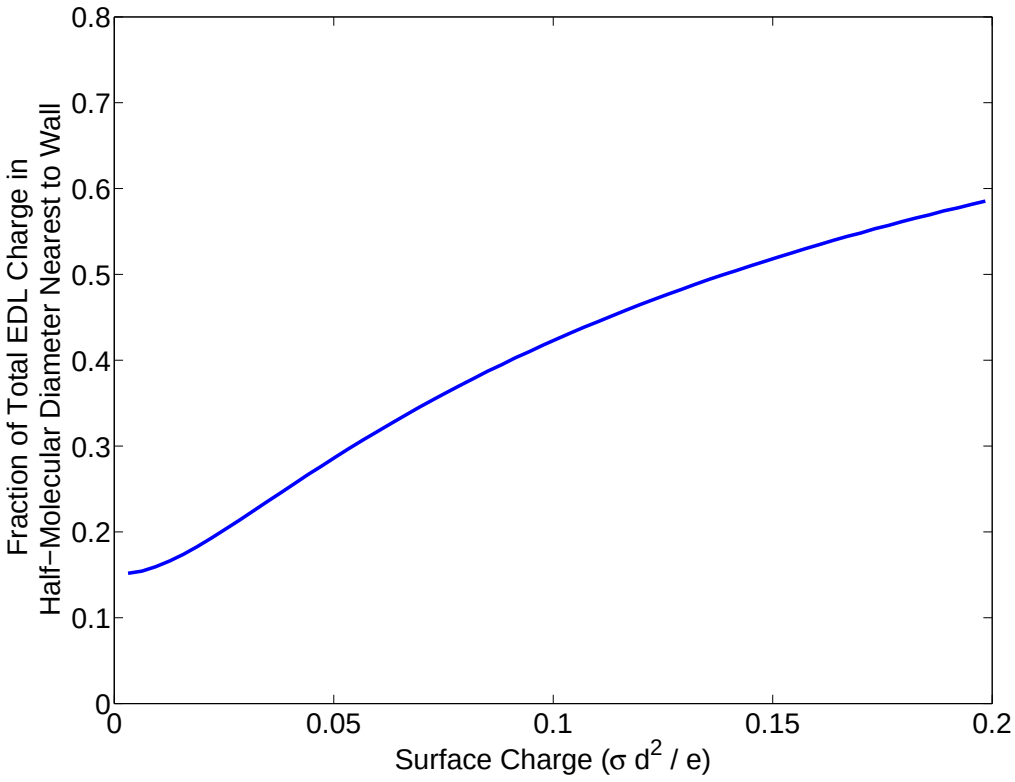

Figure 3.8. The distribution of charge in the EDL as surface charge increases (according to PB – similar trends are expected for MD and c-DFT since all three models are in good agreement in this regime). The fractional amount of charge found nearest the wall increases as surface charge increases. Prior to peak formation, the long tail of the EDL impacts the electric surface potential greatly, which causes the non-linear charging trend.

Wang *et al.* [106] found this approach to be in good agreement with MC simulations [95] of a solvent primitive electrolyte. Here we test this approach, referred to as MSA_L, against MD simulations of the 3CM in which ion and solvent species are all of finite size.

All of the preceding comparisons of c-DFT with MD use local ion densities evaluated at individual grid points to implement MSA_L. We find that those comparisons with MD are moderately degraded when the "local" Debye length is computed in an alternative manner by averaging over a surrounding sphere of molecular size, as suggested in previous versions of MSA_L [101, 102]. But these differences are very minor compared to deviations between MSA_L and MSA_B versions of c-DFT. As seen in Figure 3.9a, the ion concentrations in the first layer do not differ greatly in using these different versions of MSA, but the MSA_L produces a broader spreading of non-neutral ion concentrations into the central region of the channel. This leads to a substantial difference in the electric potential distributions depicted in Figure 3.9b. The MSA_L profile has a much broader region of gradually changing slope, resulting in a surface potential about 20% greater than MSA_B. Also included in Figure 3.9b is a c-DFT calculation that entirely excludes the MSA electric residual terms while retaining the Coulombic and hard sphere interactions, referred to as MSA_0. This leads to a surface potential that is about 20% above MSA_L. Given the excellent agreement of MSA_L with MD in our earlier results, we conclude that MSA_B and MSA_0 should be rejected in favor of MSA_L.

Differences between MSA_L and MSA_B are further illustrated in Figure 3.10 which displays bare wall and zeta potentials. The potentials for MSA_B (solid lines) generally fall below the corresponding results for MSA_L (dotted lines). This can be seen by comparing the MSA_B and MSA_L results for 1mM which are both indicated in Figure 3.10 in green and by comparing Figure 3.10 with Figure 3.3. Another interesting feature of Figure 3.10 is that the zeta potential for MSA_B becomes negative for bulk concentrations of 1M and for charges ranging from 0.4 to 0.9. This is an indication of over-screening or charge inversion which occurs when counterions adjacent to the electrode are more than sufficient to screen the surface charge. Although this phenomenon has been seen in some previous MD simulations (with polar solvent) [75, 76], it does not occur in our MD (with non-polar solvent) or MSA_L predictions for the parameter ranges considered here. So it is suspected that the charge inversion seen in Figure 3.10 may be an incorrect c-DFT result that arises from the MSA_B approximation. To better understand this phenomenon, we are studying the effects of polar solvents in an ongoing research.

Charge inversion attributed to MSA_B is also illustrated in Figure 3.11. Here, the solid symbols indicate the MC results of Lamperski and Zydor [53] for a 3CM similar to the present 3CM except that the molecules are hard spheres and the electrode surface is a hard wall; there are no LJ interactions. Also, the bulk density is 0.573 rather than 0.7 and the problem is posed on a semi-infinite domain. Our MSA_L results for this configuration are in reasonably good agreement with Lamperski's MC, whereas our MSA_B results indicate charge inversion and a resulting region of significant opposite potential near the electrode. The charge inversion is reversed in regions further from the electrode where the coions outnumber the counterions, as apparent in the inset of Figure 3.11.

Figure 3.12 compares the zeta and bare wall potentials computed by Lamperski (symbols) with our MSA_L and MSA_B results. It is seen here that the two versions of c-DFT tightly bracket the MC results. So, from this comparison, there is no reason to prefer one approach over the other. We

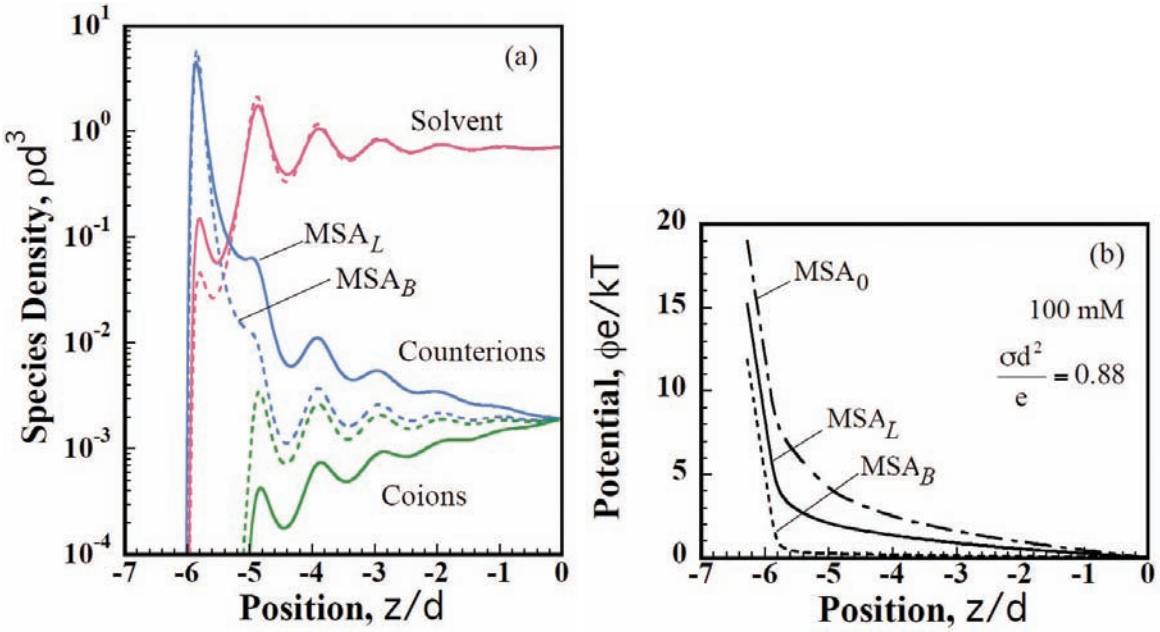

(a) Species Density Profiles

(b) Electric Potential Profiles

Figure 3.9. Comparison of results obtained with alternative implementation of MSA. Local evaluation of Debye length in MSA$_L$ produces broader distribution of counterions and higher surface potentials than bulk evaluation in MSA$_B$. MSA$_L$ is in best agreement with MD results, as suggested by comparisons in Figures 3.3-3.6.

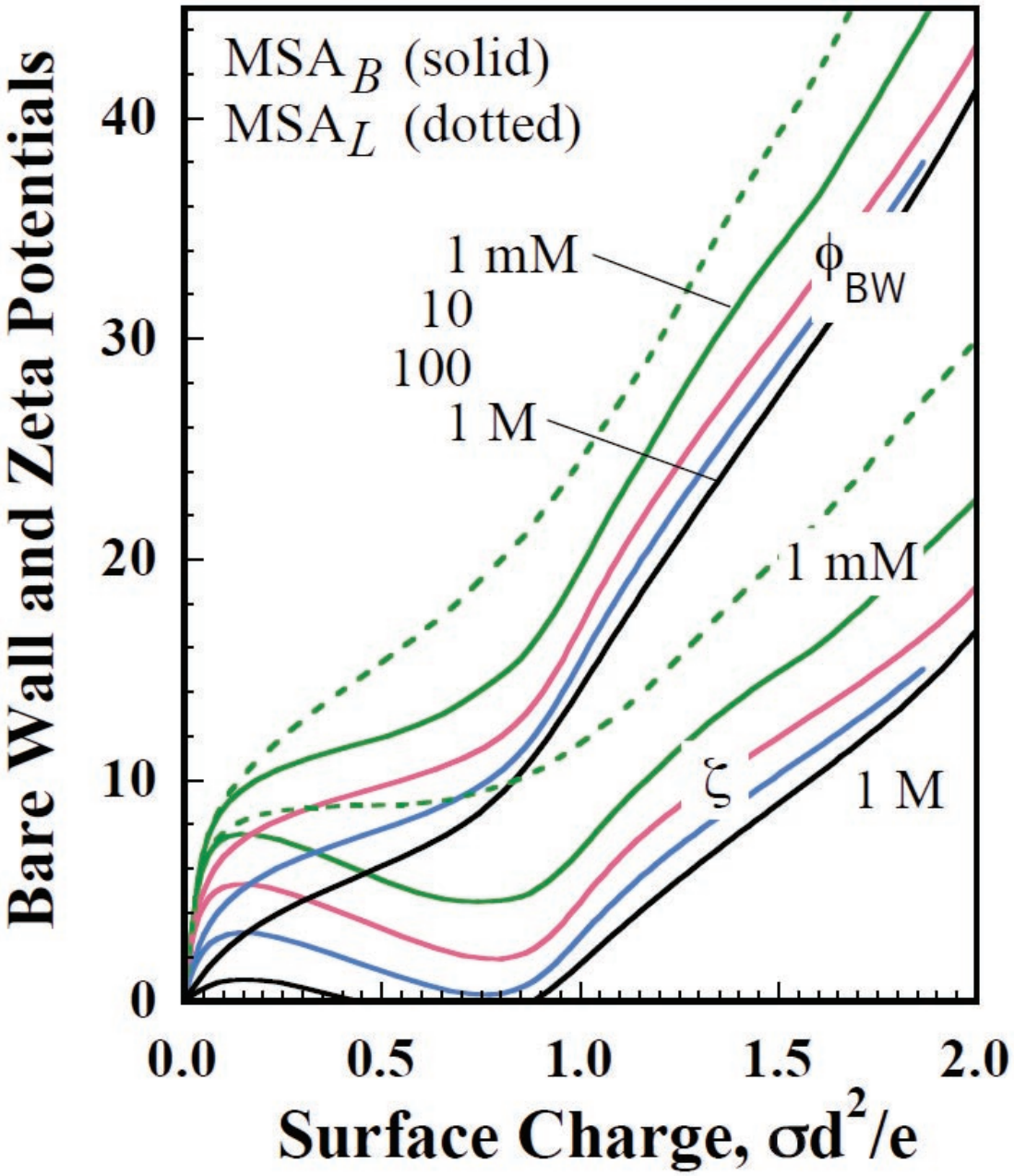

Figure 3.10. Capacitance comparison for MSA$_B$ (solid lines) vs. MSA$_L$ (dashed lines). The bare wall potentials are the upper curves, labeled as ϕ_{BW}, and the zeta potentials are the lower curves, labeled as ζ. Colors denote bulk ion molarities, as indicated in the plot. MSA$_B$ predicts strong charge inversion and negative zeta potentials for 1M, in contrast to MSA$_L$ and MD.

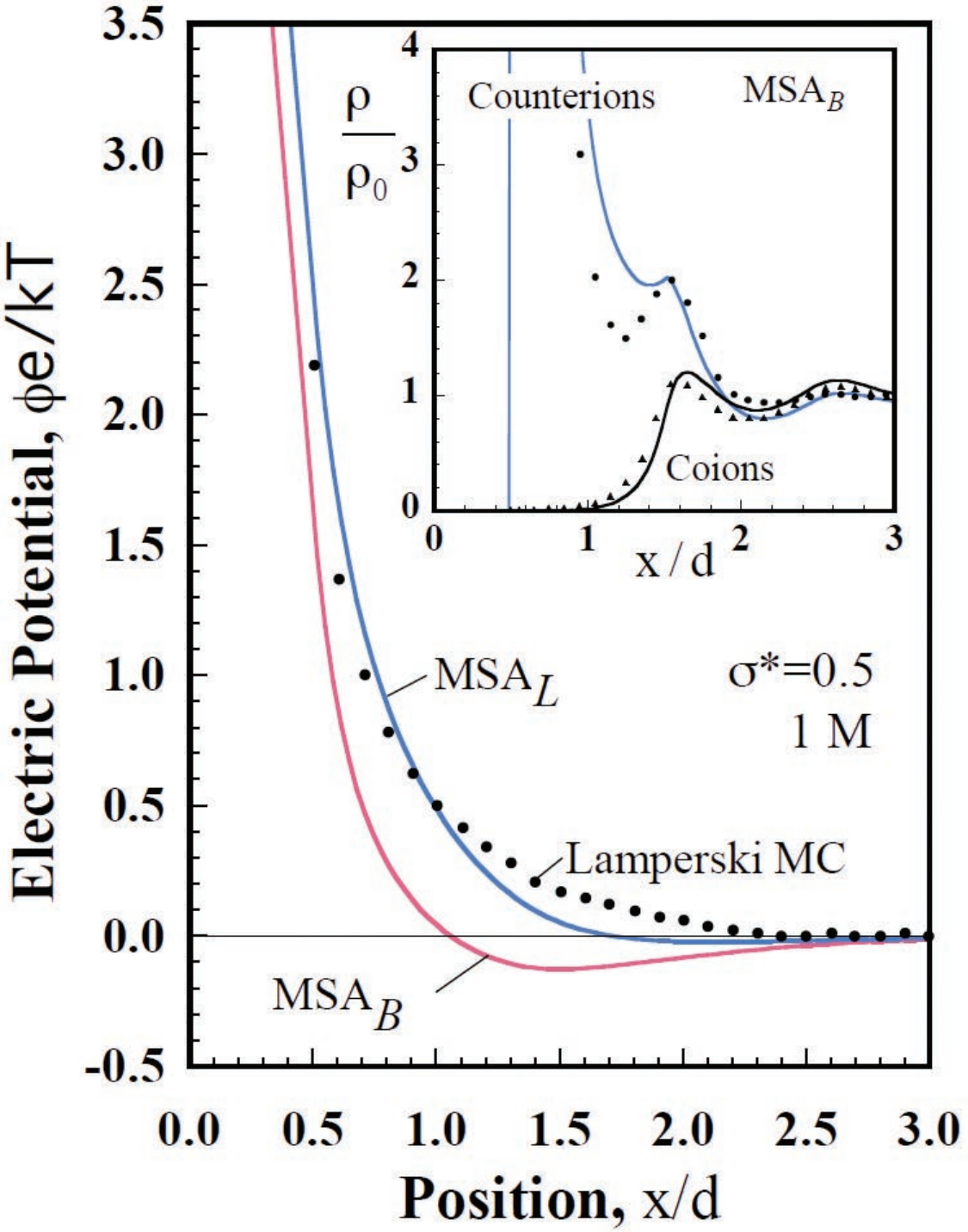

Figure 3.11. MSA_B and MSA_L implementation schemes compared with Lamperski MC electric potential and ion density profiles. MSA_B produces charge inversion in contrast to MSA_L and MC.

note that differences between our c-DFT MSA$_L$ and Lamperski's MC results, particularly those in the potential profiles of Figure 3.11, may arise partly from differing treatments of electrostatic interactions. The MC uses the method of charged planes to estimate long-range forces which is thought to be less accurate [16] than the corrected 3D Ewald summations used in our MD and the Poisson solver used in our c-DFT.

3.6 Conclusion

MD and c-DFT models of electrolyte fluids contained within nanochannels were studied and compared to classical PB theory. To facilitate proper comparison, special care was taken to model analogous parameters with both techniques. The simulations performed in this study used the 3CM, in which solvent and solute are represented by three distinct molecular species. The fluid-fluid and fluid-solid interactions use LJ-type potentials, in contrast to previous c-DFT-to-MC comparison studies, which utilized hard-sphere and hard-wall repulsions. In further contrast with previous studies, our simulations cover a wide range of electrolyte concentrations and surface charge densities. Our MD models are able to simulate concentrations as low as 10mM and still produce density profiles in agreement with c-DFT over a five to six decade range. All of our nanochannels are sufficiently wide to prevent overlapping EDLs, even in the case of low ion concentrations (hence large Debye lengths). A discernible bulk region with zero potential is important for direct comparison between MD and c-DFT.

As a result, MD and c-DFT methods are in excellent agreement for various qualitative and quantitative assessments, particularly for large molarities. Metrics for assessment include atomic density, charge density, electric field, and electric potential profiles, as well as capacitance trends for various loadings and concentrations. Specifically, density profiles agreed particularly well on peak location and spacing, while differing slightly on peak height and width. Comparisons are improved when c-DFT uses a modified hard sphere radius of $d_{hs} = 0.93 d_{LJ}$ and the MSA$_L$ implementation. MD calculations tended to have taller, narrower peaks than the c-DFT; this is resolved by the fact that there is an equivalent amount of charge in the layer.

Moreover, as electrolyte concentration decreases and surface charge loading increases, deviation from PB becomes increasingly apparent. These trends highlight the effect of distinct ion packing layers, which is due to the finite sizes of electrolyte and solute. Distinct layers result in significantly reduced capacitances relative to the predictions from PB theory. Further investigation shows a layer packing phenomenon in which a new ion peak begins to form when solvent is completely expelled from the previous fluid layer. The onset of the new ion peak produces a kink in the electric field and electric potential profiles, thereby reducing the capacitance of the EDL. Since this behavior arises from finite size effects, it is not captured in PB theory.

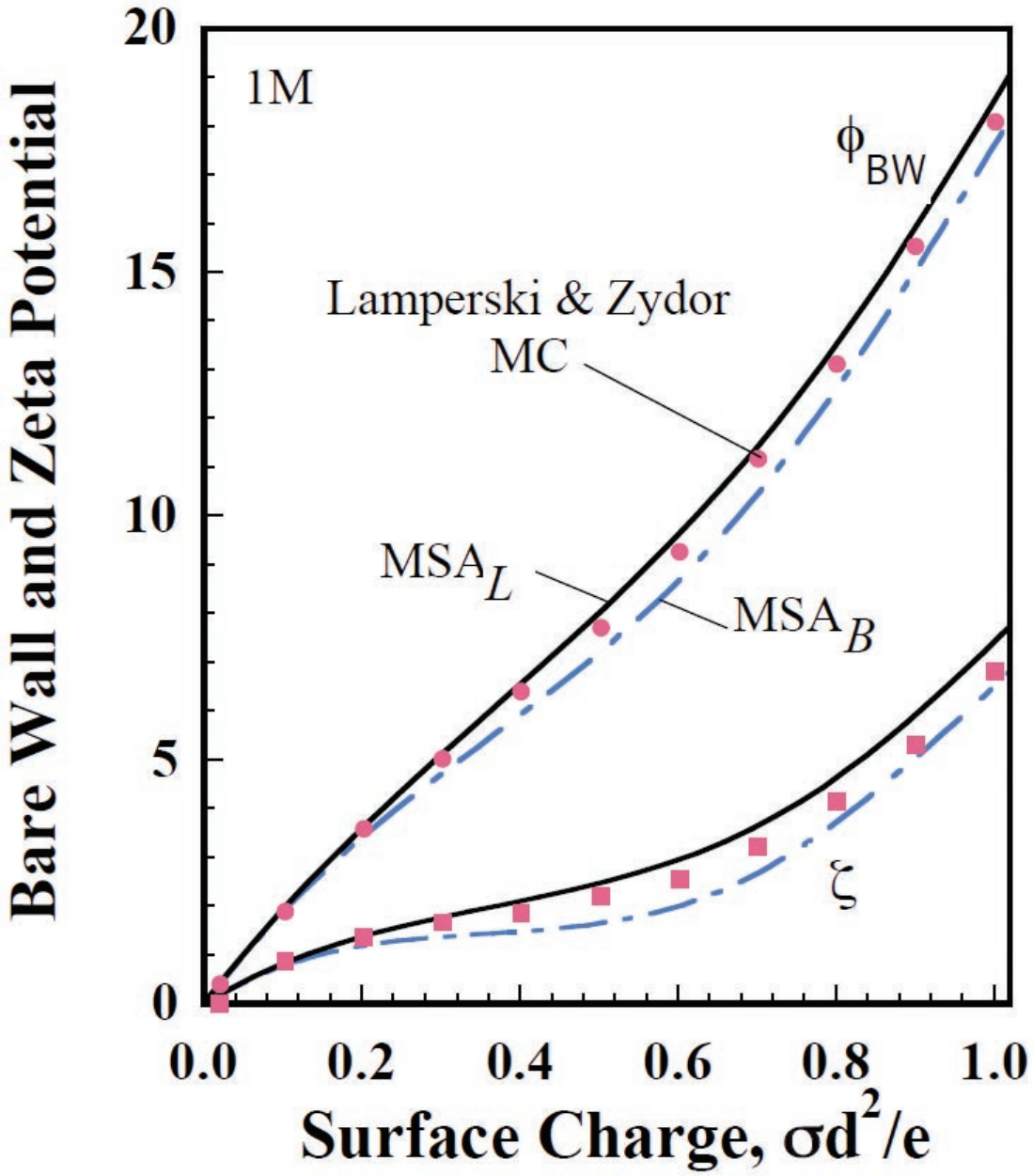

Figure 3.12. Bare wall and zeta potential trends of MSA_B and MSA_L implementation schemes compared with Lamperski's MC.

Chapter 4

Comparing TIP3P Solvent in Molecular Dynamics with Asymmetric Dipole in Fluids Density Functional Theory for Electrolyte Solutions in Charged Nanochannels

4.1 Introduction

As device miniaturization and electrical energy storage becomes increasingly relevant in today's technologies, we must strive to better understand the structure and basic physics of the electric double layer (EDL). In a recent study, we have shown using molecular dynamics (MD) simulation and Fluids Density Functional Theory (f-DFT) that a simple coarse-grained solvent model with a uniform dielectric constant was sufficient to illustrate large deviations from classic Poisson-Boltzmann theory [59]. It was shown specifically that beyond a certain surface charge loading, a steric layer of ions (the Stern layer) would form near the interface which causes a local depletion of the solvent. Furthermore, the ions have a finite packing structure which dictates the size of the Stern layer. This phenomenon is expressly absent from PB theory, which allows infinite packing.

Note that the dielectric constant is applied specifically to model the polar nature of the solvent, since this aspect is missing from the coarse-grained model. The approximation is expected to break down as the fluid becomes non-bulk-like, and it is definitely invalid for regions where the solvent is depleted. To understand the actual nature of the solvent and ion-solvent interaction at a charged surface, we shift our model from the coarse-grained solvent to a solvent molecule with explicitly described dipole(s). The solvent molecule is modelled based on water. Given the speed of f-DFT calculations, being able to model those interactions accurately with f-DFT would be an ideal resource for exploring a large parameter-space of this type of system. Unfortunately, the current code capabilities and limitations of the theory constrain our ability to model bonded systems. Conversely, for MD simulations, we can easily apply the TIP3P water model, where three rigidly bonded atomic sites serve as charge carriers, and the "oxygen" site also interacts with a Lennard-Jones potential. In an effort to find an appropriate f-DFT model for the water solvent, the f-DFT solvent is modelled as a dumbbell molecule with varied site sizes, charges, and bond

The primary authors of this chapter are J. Lee and J. Templeton

length. The f-DFT solutions are matched against the MD solutions in an optimization routine to find the most ideal set of parameters.

Following the optimization, the f-DFT is applied to a number of surface charges and ionic concentrations, which would be too time consuming (and virtually impossible in some cases) to simulate using MD. The following section describes the MD and f-DFT methods. This is followed by a presentation and discussion of the optimization and parameter study results, and lastly, we give final remarks and discuss future work.

4.2 Methodology

4.2.1 Molecular Dynamics

MD simulations of an electrolyte solution in an electrically charged nanochannel were performed with the LAMMPS software package [72]. The TIP3P water model (MSM) [48] is used in order to simulate some of the complexities of a molecular polar solvent. The models are examined over a range of surface charge densities. The simulation domain consists of a 1:1 electrolyte fluid bounded in the z-dimension by two substrate walls, which are positioned such that the EDLs do not overlap and a bulk region can be defined. Classically, EDL lengths are determined by the Debye lengths, which depend on the ionic molarity. For ease of computation, we only explore the 1M case, which has a Debye length of 3.08 Å. Periodic boundary conditions are applied in the transverse directions with a cross-section of 5nm $\times$ 5nm. Atomic interactions are modelled with Lennard-Jones (LJ) [47] and Coulomb's law. Simulations are performed at a nominal temperature of 300K.

In the TIP3P water model, there are three charge and mass carrier sites, and only the oxygen site interacts via LJ with other atoms and molecules. The charges on the hydrogen and oxygen atoms are fractional charges, and the masses are obtained from the periodic table. Bonds and angles are held rigid using the SHAKE algorithm [82]. All ions have the same atomic size and mass as the oxygen atom, and the mass is the same as the total water molecule. We use an unstructured one-dimensional LJ-type potential to model the substrate-fluid interaction.

Equations of motion are integrated with the velocity-Verlet algorithm [97, 98]. A timestep of 0.0005 picoseconds (ps) was used. LJ and Coulomb interactions both use a 1.3 nm cutoff radius. Long range Coulombics are computed using the PPPM algorithm [42] with slab geometry [114]. A summary of simulation parameters is shown in Table 4.1.

The systems are initialized according to the following procedure. Oxygen atom and ion coordinates are randomly placed at body-centered-cubic lattice sites. Hydrogen atoms are placed in a random configuration around the oxygen atoms. The total number of solvent atoms is chosen such that the bulk solvent density targets that of water at standard temperature and pressure. Similarly, the number of ions is chosen such that the the bulk molarity is targeted towards a desired value. Note that for MD simulations, bulk densities and molarities can not be determined *a priori*, so some iteration is often required. To estimate the number of ions to place in the system given a

Atom	ε (eV)	d (Å)	m (g/mol)	q (e^-)
H	0.0	0.0	1.008	+0.415
O	0.006596	3.1507	15.9994	−0.830
+ Ion	0.006596	3.1507	18.0154	+1
− Ion	0.006596	3.1507	18.0154	−1

Table 4.1. Atomistic parameters for all simulation variations. Inter-species parameters are obtained by the usual mixing rules: geometric mean for ε and arithmetic mean for d.

particular bulk molarity, an approximate bulk region is defined. The definition is based on the PB Debye length:

$$\lambda_D = \sqrt{\frac{\varepsilon k_B T}{2 n^o e^2}}, \tag{4.1}$$

where k_B is the Boltzmann constant, T is the temperature, n^o is the bulk molarity, and e is an electron charge. The region extending beyond the Debye length (from both substrates) is regarded as the bulk, for initialization purposes. Inside this bulk region, the number of ions is computed directly from the target molarity. Inside the PB EDLs, the number of counterions is sufficient to perfectly screen the surface charge, while the number of coions is set to zero.

The z-dimension is bounded by LJ 10-4-3 walls[60], of the form:

$$E = 2\pi\varepsilon \left[\frac{2}{5}\left(\frac{d}{r}\right)^{10} - \left(\frac{d}{r}\right)^{4} - \frac{\sqrt{2}d^3}{3\left(r + \left(0.61/\sqrt{2}\right)d\right)^3} \right]. \tag{4.2}$$

The wall potential uses a cutoff of 3.5 times the corresponding d. The parameters are also listed in Table 4.1. To model oppositely charged surfaces, a linear background electric field is applied to the system proportional to the surface charge density. Note that for the 3CM system, the dielectric constant effectively reduces the applied electric field by a factor of 80. All atom velocities are initialized to zero since lattice vacancies will cause the system kinetic energy to increase rapidly. The fluid box is equilibrated for one million timesteps to 300K. A Nosé-Hoover [69, 43, 61] thermostat is used to regulate the temperature. To avoid any local minima in the energy landscape, the system is annealed to 1000K for one million timesteps, followed by a cooling step back to 300K for two million timesteps.

After the system is equilibrated, the thermostat is turned off. The systems are allowed to naturally evolve toward a steady state solution for five million timesteps. The first one million timesteps after equilibration is considered transient, and the rest are confirmed to be steady state. Five permutations are performed for each surface charge case.

Spatial dependent particle concentrations are extracted by species from the domain via an

atomistic-to-continuum (AtC) interpolation method [117]. The resolution of the 1-D continuum mesh is approximately 0.1 Å. The concentration data is collected every 0.25 ps to facilitate post-processing. After removing the transient data, the remaining data is time-averaged and ensemble-averaged. The concentrations, scaled by the atomic valence, can be integrated once to get the z-component of the electric field and twice integrated to get the electric potential. The ζ-potential is determined by taking the difference in electric potential evaluated at the fluid-wall interface from the electric potential evaluated in the bulk. The electric potential at the wall is measured at the LJ 10-4-3 origin. The ion molarities are also measured in reference to the average behavior of the center 10 nm of the bulk region.

4.3 Fluids Density Functional Theory

Fluids Density Functional Theory (f-DFT) calculations are performed using the Tramonto software package [https://software.sandia.gov/tramonto/publications.html]. In f-DFT, the grand potential energy, Ω, of the system is expressed as a function of the atomic density distributions and position. Contributions are summed from atomic interactions, external potential fields, and ideal gas behavior. Atomic interactions are modelled with a cut-and-shifted LJ between an inner and outer cutoff and Coulombic forces. Inside the inner cutoff (typically the LJ length parameter or slightly smaller), a hard sphere repulsion is added. Ω is minimized to find the steady state equilibrium solution. The domain is the same as with MD, except for a change in the functional form of the LJ wall potential. The wall potential is of the 9-3 form, *i.e.*

$$E = \varepsilon \left[\frac{2}{15} \left(\frac{d}{r} \right)^9 - \left(\frac{d}{r} \right)^3 \right]. \tag{4.3}$$

The evaluated fields are three-dimensional, but restricted to vary only in the wall-normal dimension.

Due to limitations of the current software and theory, the f-DFT solvent model could not be exactly analogous to that of the MD model. Instead, the solvent molecule is modelled as an asymmetric dumbbell. The bond is treated as a constraint on the free energy of the two atomic species. The sites are given equal and opposite fractional charges, and their LJ sizes, as 'viewed' by each other, are both equal to the bond length such that they are tangentially touching. However, the LJ sizes, as 'viewed' by themselves and the solute atoms, are not necessarily equal. The non-dimensional LJ parameters are given in Table 4.2. The masses are not relevant for this f-DFT calculation, and the charge on the ions are the same as the MD model.

To find the model parameters, we ran an optimization routine to minimize the difference relative to the MD results. The cost functions consisted of counterion density, coion density, electric field (from ionic contributions only), and electric potential (from ionic contributions only) profiles on both the positive and negative electrodes. The parameters that were varied include the dumbbell charge, q, dumbbell bond length, b, LJ size of the positive dumbbell site (applied to self-self, self-ion, and self-wall interactions), s, and the dielectric permittivity, ε_r. The optimization was performed using DAKOTA [http://dakota.sandia.gov/publications.html].

d:	'2H'	'O'	+ Ion	− Ion
'2H'	*s*	*b*	*s*	*s*
'O'	*b*	1.0	1.0	1.0
+ Ion	*s*	1.0	1.0	1.0
− Ion	*s*	1.0	1.0	1.0
ε:	'2H'	'O'	+ Ion	− Ion
'2H'	1.0	1.0	1.0	1.0
'O'	1.0	1.0	1.0	1.0
+ Ion	1.0	1.0	1.0	1.0
− Ion	1.0	1.0	1.0	1.0

Table 4.2. Atomistic parameters for all f-DFT simulation variations. Mixing rules are specifically not used for these interactions. All values are in non-dimensional units.

4.4 Results

The following results are from a positively charged wall case. The applied surface charge is 0.9922 electrons per dimensionless area. The physical parameters used for the f-DFT in these results are shown in Table 4.3. The (dimensionless) dipole moment for the f-DFT is 0.6; the dipole moment for TIP3P is 0.154.

	f-DFT	MD
q:	1.0	0.830
σ:	0.1	0.0
b:	0.6	0.186
ε_r:	1.0	1.0

Table 4.3. Physical parameters used for f-DFT calculation of case presented in Results. The four parameters are the positive dumbbell site charge, the positive dumbbell site size parameter, the dumbbell bond length, and the relative permittivity constant. As a comparison, the corresponding parameters for the MD TIP3P model are shown. The charge and bond length refer to the resultant dipole moment from the two individual dipoles summed together. All parameters are dimensionless.

Figure 4.1 shows the ionic number density comparison between the two models. The co-ion data from MD is not smooth because the number of positive ions near a positively charged wall are so low; it is difficult to gather good statistics using MD. While this may adversely affect the optimization results, the matching of co-ion structure is much less significant to that of the counter-

ion structure. There are key differences in the counter-ion structure that need to be addressed, namely the number of observable peaks, and the peak shape(s) and location(s). The f-DFT shows only one dominant peak whereas the MD shows the emergence of a second peak. It is possible that this surface charge uniquely corresponds to the transition point from a single counter-ion peak to double counter-ion peaks; as such, it would not be unreasonable to expect some disagreement between the two models on the exact conditions of the transition. Also, the counter-ion peak magnitude has been truncated in the figure, and it is actually approximately 2.5 times higher than that of the MD. It is common, however, to expect taller, sharper peaks in f-DFT as compared with MD. The location of the peaks is also slightly offset, which could be caused by the hard-sphere functionals and inner cutoffs used by the f-DFT, which is the primary difference in interaction potentials of the two models. Lastly, the two models are using slightly different wall potentials, which further complicates the comparison.

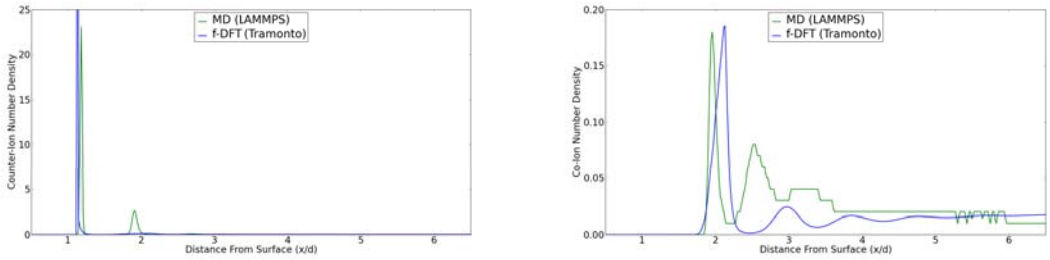

(a) Counter-Ion Number Density

(b) Co-Ion Number Density

Figure 4.1. Counter-Ion and Co-Ion number density profiles. The f-DFT and MD results are overlaid to show the comparison.

Figure 4.2 shows the ionic contributions to the: charge density profile, wall-normal component of the electric field profile, and electric potential profile of the two models. The charge density is just a linear combination of the previous figures. The electric field is the integral of the charge density with the applied field as a background offset. The electric potential is the integral of the electric field with an arbitrary offset. The wall-normal electric field shows agreement in the bulk, which means both models have sufficiently shielded the surface charge by that point. Furthermore, the contribution from the first MD peak shields the majority of the surface charge while the f-DFT essentially shields all of it (with a long exponential-like decay). This suggests that the first counter-ion peak is actually in fairly decent agreement between the two models. Unfortunately, the disagreement also shows up quite prominently in the electric potential profile, since there is only one significant change in slope in the f-DFT profile.

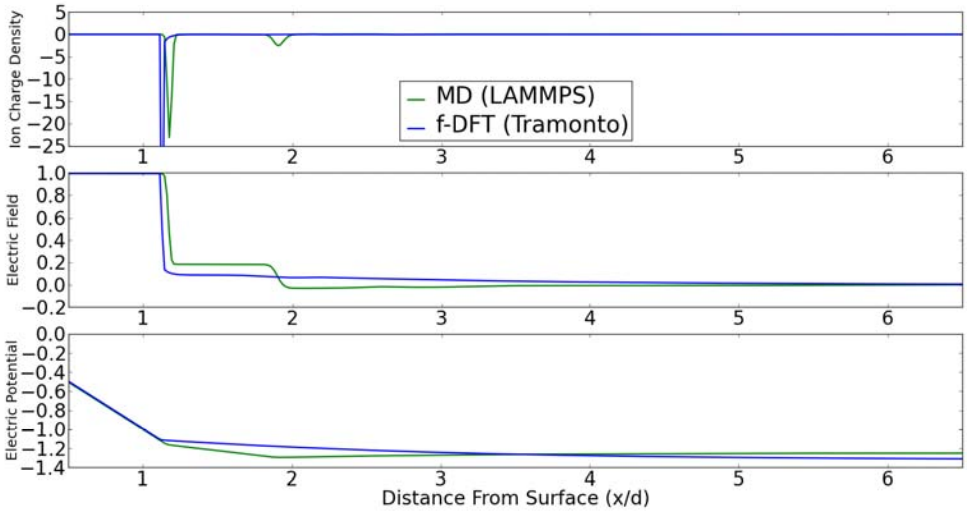

Figure 4.2. Charge density, Electric Field, and Electric Potential profiles. The f-DFT and MD results are overlaid to show the comparison.

This page intentionally left blank.

Chapter 5

Spatial resolution of diffusivity and conductivity for ionic fluids using Green-Kubo methods

This chapter develops methods to spatially resolve transport properties in a wall-ionic fluid system that is in electro-chemical equilibrium. A solid interface induces spatial gradations and anisotropy in the fluid. In steady-state/equilibrium the electro-chemical potential (not the chemical potential) is constant. The methods developed here are based on Green-Kubo/linear response methods which are typically applied to full systems but herein extended to a collection of disjoint cells covering the system.

5.1 Theory

5.1.1 Mixture theory & Linear irreversible thermodynamics

The per-species mass densities $\rho^{a)}$ are such that i.e. $\rho^{(a)} = \frac{1}{V}\sum_\alpha m_\alpha^{(a)}$ (followomg mixture theory, refer to [18, Chap. XIII],[28])

$$\rho = \sum_a \rho^{(a)} \tag{5.1}$$

and satisfy the conservation equation

$$\frac{\partial}{\partial t}\rho^{(a)} + \nabla_{\mathbf{x}} \cdot \left(\rho^{(a)}\mathbf{v}^{(a)}\right) = 0 \tag{5.2}$$

The primary authors of this chapter are S. Davidson, R. Jones, J. Templeton, and D. Ward.

These balances are consistent with the overall conservation of mass $\rho_{,t} + \nabla_{\mathbf{x}} \cdot (\rho \mathbf{v}) = 0$ with barycentric velocity

$$\rho \mathbf{v} = \sum_a \rho^{(a)} \mathbf{v}^{(a)} \tag{5.3}$$

Given that the material time derivative is defined *with respect to the barycentric velocity*

$$\begin{aligned} \dot{\rho}^{(a)} &\equiv \frac{\partial}{\partial t}\rho^{(a)} + \mathbf{v} \cdot \nabla_{\mathbf{x}} \rho^{(a)} \\ &= -\nabla_{\mathbf{x}} \cdot \left(\rho^{(a)} \mathbf{v}^{(a)} \right) + \mathbf{v} \cdot \nabla_{\mathbf{x}} \rho^{(a)} \\ &= -\rho^{(a)} \nabla_{\mathbf{x}} \cdot \mathbf{v} - \nabla_{\mathbf{x}} \cdot \underbrace{\rho^{(a)} \left(\mathbf{v}^{(a)} - \mathbf{v} \right)}_{\mathbf{J}^{(a)}} \end{aligned} \tag{5.4}$$

consistent with $\dot{\rho} = -\rho \nabla_{\mathbf{x}} \cdot \mathbf{v}$.

Eq. 5.4 implies that the diffusive flux for species a should be defined as

$$\mathbf{J}^{(a)} = \rho^{(a)} \left(\mathbf{v}^{(a)} - \mathbf{v} \right) = \mathbf{J}_0^{(a)} - \rho \mathbf{v} \tag{5.5}$$

which satisfies the conservation equation (Fick's 2nd law)

$$\rho \dot{c}^{(a)} + \nabla \cdot \mathbf{J}^{(a)} = 0 \tag{5.6}$$

Here, species concentrations can be defined

$$\rho c^{(a)} = \rho^{(a)} \tag{5.7}$$

so that they satisfy the conservation equation

$$\rho \dot{c}^{(a)} + \nabla_{\mathbf{x}} \cdot \mathbf{J}^{(a)} = 0 \tag{5.8}$$

Also, $\sum_a \mathbf{J}^{(a)} = \sum_a \rho^{(a)} \mathbf{v}^{(a)} - \mathbf{v} \sum_a \rho^{(a)} = \mathbf{0}$ by construction Eq. (5.5) and the definitions (5.1) and (5.3).

The electrical current is simply the flux of charge (density) $\mathbf{I}_0 = \frac{1}{V} \sum_\alpha q_\alpha$:

$$\mathbf{I}_0 = \sum_a \rho^{(a)} z^{(a)} \mathbf{v}^{(a)} = \rho z \mathbf{v} + \underbrace{\sum_{a=1}^{n} z^{(a)} \mathbf{J}^{(a)}}_{\mathbf{I}} \tag{5.9}$$

Fluxes associated with various reference velocities and normalizations based on number versus mass appear [18, Chap. XI Sec. 2]. These just change the diffusion coefficient but not the form of the governing equation. In general the mass fluxes are defined with respect to the barycentric velocity; but, according to Prigogine's theorem, under mechanical equilibrium $\rho \dot{\mathbf{v}} = 0$ and p constant, and the fluxes can be defined with repect to an arbitrary velocity $\bar{\mathbf{v}} = \sum_a a^{(a)} \mathbf{v}^{(a)}$ here $a^{(a)}$ is coefficient [18, Chap. XI Sec. 2]. The Gibbs-Duhem relation $\sum_a \mathbf{X}^{(a)} = \mathbf{0}$ is also invoked to remove an flux [107].

where $z^{(a)} = \sum_\alpha q_\alpha^{(a)} / \sum_\alpha m_\alpha^{(a)} = q^{(a)}/m^{(a)}$ is the charge per unit mass and $\rho^{(a)} z^{(a)}$ is the charge per unit volume of species a such that the net charge per mass z is given by

$$z = \frac{1}{\rho} \sum_a \rho^{(a)} z^{(a)} = \sum_a c^{(a)} z^{(a)} \tag{5.10}$$

Note the convective term $\rho z \mathbf{v}$ is zero if : (a) the fluid is quiescent $\mathbf{v} \equiv \mathbf{0}$ or (b) charge neutral $z \equiv 0$, *locally*. With this flux $\mathbf{I}$ the conservation equation

$$\rho \dot{z} + \nabla \cdot \mathbf{I} = 0 \tag{5.11}$$

is satisfied [18, Chap. XIII Sec. 3] after using Eq. (5.8) the fact that $z^{(a)}$ is constant.

The electrochemical potential

$$\Psi^{(a)} = \mu^{(a)} + z^{(a)} \phi \tag{5.12}$$

is defined in terms of the chemical potentials $\mu^{(a)}$ for the species a and the electrostatic potential ϕ. For an isothermal mixture, entropy production ς is

$$\varsigma = -\frac{1}{T} \left(\sum_a \mathbf{J}^{(a)} \cdot \nabla \mu^{(a)} - \mathbf{I} \cdot \mathbf{E} \right) = -\frac{1}{T} \sum_a \mathbf{J}^{(a)} \cdot \nabla \Psi^{(a)} \tag{5.13}$$

see [18, Chap. XIII Sec. 4] where the electric field is $\mathbf{E} = -\nabla \phi$. In equilibrium, with zero barycentric velocity, and the Helmholtz vector potential independent of time

$$\nabla_{\mathbf{x}} \Psi^{(a)} = \nabla_{\mathbf{x}} \Psi^{(b)} \quad \forall b \tag{5.14}$$

i.e. the electro-chemical potentials are equal up to a constant.

Linear phenomenological relations between the driving forces and the flux are assumed

$$\mathbf{J}^{(a)} = -\frac{1}{T} \sum_{b=1}^{n-1} L^{(a,b)} \nabla \mu^{(b)} \tag{5.15}$$

and

$$\mathbf{I} = -\frac{1}{T} \sigma \nabla_{\mathbf{x}} \Psi \tag{5.16}$$

see [28]. See also [115, 107]. [107] relates $L^{(a,b)}$ to σ see later. Specific to binary mixture. $\Psi = (\Psi^{(1)} - \Psi^{(2)})/(z^{(1)} - z^{(2)})$ and $\mathbf{I} = (z^{(1)} - z^{(2)}) \mathbf{J}^{(1)}$

$$\varsigma = \frac{1}{T} \mathbf{I} \cdot \nabla_{\mathbf{x}} \Psi$$

For the isothermal electrical resistance R

$$T\varsigma = \mathbf{I}_0 \cdot \underbrace{\left(\mathbf{E} - \nabla \frac{\mu}{z} \right)}_{R \mathbf{I}_0} \tag{5.17}$$

For a mixture of two ionic species (1,2) and a neutral solvent (0):

$$\begin{aligned} -T\varsigma &= \mathbf{J}^{(0)}\cdot\nabla\mu^{(0)} + \mathbf{J}^{(1)}\cdot\nabla\mu^{(1)} + \mathbf{J}^{(2)}\cdot\nabla\mu^{(2)} - \mathbf{I}\cdot\mathbf{E} \\ &= \mathbf{J}^{(1)}\cdot\nabla\left(\mu^{(1)}-\mu^{(0)}\right) + \mathbf{J}^{(2)}\cdot\nabla\left(\mu^{(2)}-\mu^{(0)}\right) - \mathbf{I}\cdot\mathbf{E} \\ &= \mathbf{I}\cdot\nabla\Psi + \left(\mathbf{J}^{(1)}+\mathbf{J}^{(2)}\right)\cdot\nabla\left(\frac{z^{(1)}\mu^{(2)}-z^{(2)}\mu^{(1)}}{z^{(1)}-z^{(2)}} - \mu^{(0)}\right) \end{aligned} \tag{5.18}$$

after use of construction of $\mathbf{J}^{(a)}$ Eq. (**??**) Extra term disappears if $\mathbf{J}^{(1)} = -\mathbf{J}^{(2)}$ i.e. if $\mathbf{J}^{(0)} \equiv \mathbf{0}$.

Alternatively, assuming mech eq Prigogine's thm. following [], use fluxes $\tilde{\mathbf{J}}^{(a)} \equiv \rho^{(a)}\left(\mathbf{v}^{(a)} - \mathbf{v}^{(0)}\right)$ relative to arb vel specifically $\mathbf{v}^0$ s.t. $\tilde{\mathbf{J}}^{(0)} \equiv \mathbf{0}$ and $\sum\tilde{\mathbf{J}}^{(a)} = \rho\left(\mathbf{v}-\mathbf{v}^{(0)}\right)$ so that

$$\begin{aligned} -T\varsigma &= \tilde{\mathbf{J}}^{(1)}\cdot\nabla\mu^{(1)} + \tilde{\mathbf{J}}^{(2)}\cdot\nabla\mu^{(2)} - \mathbf{I}\cdot\mathbf{E} \\ &= \mathbf{I}\cdot\nabla\Psi + \left(\tilde{\mathbf{J}}^{(1)}+\tilde{\mathbf{J}}^{(2)}\right)\cdot\nabla\left(\frac{z^{(1)}\mu^{(2)}-z^{(2)}\mu^{(1)}}{z^{(1)}-z^{(2)}}\right) \\ &= \mathbf{I}\cdot\nabla\Psi + \rho\left(\mathbf{v}-\mathbf{v}^{(0)}\right)\cdot\nabla\left(\frac{z^{(1)}\mu^{(2)}-z^{(2)}\mu^{(1)}}{z^{(1)}-z^{(2)}}\right) \end{aligned} \tag{5.19}$$

Specifically if $z^{(1)} = -z^{(2)}$ but not necessarily electroneutrality

$$-T\varsigma = \mathbf{I}\cdot\nabla\Psi + \frac{1}{2}\left(\mathbf{J}^{(1)}+\mathbf{J}^{(2)}\right)\cdot\nabla\left(\mu^{(2)}+\mu^{(1)}\right) \tag{5.20}$$

[107, Eq. (9)] relates to diffusion coeff

$$\varsigma = \sum_{a,b\neq 0} L_0^{(a,b)}\vartheta^{(a)}\vartheta^{(b)} \tag{5.21}$$

[14, Eq. (23)] relates this to the Nerst-Einstein relation and drop the cross terms.

5.1.2 Green-Kubo & Linear response theory

The Green-Kubo formulae are usually derived via one of two routes: (a) linear response of perturbed Hamiltonian or (b) a Laplace-Fourier transform of macroscale PDE.

Following the first route, the Hamiltonian perturbed by the flux is

$$\mathscr{H} = \mathscr{H}_0 - V\sum_a \mathbf{r}^{(a)}\cdot\mathbf{X}^{(a)} \tag{5.22}$$

where $\dot{\mathbf{r}}^{(a)} = \mathbf{v}^{(a)}$. The response

$$\begin{aligned} \langle A\rangle_0 + \langle\Delta A\rangle &= \frac{\int d\Gamma \exp[-\beta(\mathscr{H}_0 - \lambda B(p,q))]A}{\int d\Gamma\exp[-\beta(\mathscr{H}_0-\lambda B(p,q))]} \\ &= \beta(\langle B(0)A(t)\rangle_0 - \langle B(0)\rangle_0\langle A(t)\rangle_0) = \beta\langle B(0)A(t)\rangle_0 \end{aligned} \tag{5.23}$$

where 0 subscript is at equilibrium. The response is

$$\langle \mathbf{J}^{(a)}(t)\rangle_1 = \langle \mathbf{J}^{(a)}(0)\rangle_0 + \frac{V}{k_B T}\int_0^t ds\, \langle \mathbf{J}^{(a)}(s) \sum_b \mathbf{J}^{(b)}(t)\cdot \mathbf{X}^{(b)}\rangle \tag{5.24}$$

so

$$L_0^{(a,b)} \equiv \lim_{t\to\infty, \mathbf{X}^{(b)}\to 0} \frac{\partial \langle \mathbf{J}^{(a)}(t)\rangle}{\partial \mathbf{X}^{(b)}} = \frac{V}{k_B T}\int_0^t ds\, \langle \mathbf{J}^{(a)}(s)\cdot \mathbf{J}^{(b)}(t)\rangle \tag{5.25}$$

A phenomenlogical equation is asssumed for

$$\langle \Delta A\rangle = \int_{-\infty}^t ds \chi_{AB}(t-s)\lambda(s) \tag{5.26}$$

Mutual diffusion

Fick's 1st law

$$\mathbf{J}^{(i)} = -\frac{1}{T}\sum_{j=1}^{n-1} L^{(ij)}\nabla_{\mathbf{x}}\left(\frac{1}{m^{(j)}}\mu^{(j)} - \frac{1}{m^{(0)}}\mu(0)\right) = -\rho\sum_{j=1}^{n-1} D^{(ij)}\nabla_{\mathbf{x}} c^{(j)} \tag{5.27}$$

together with Eq. 5.6 gives Fick's 2nd law. The coefficient matrices are related by

$$D^{(ij)} = L^{(ik)}\frac{1}{\rho T}\frac{\partial}{\partial c^{(j)}}\left(\frac{1}{m^{(k)}}\mu^{(k)} - \frac{1}{m^{(0)}}\mu^{(0)}\right) \tag{5.28}$$

Mutual diffusion

$$L^{(a,b)} = \frac{1}{3k_B V}\int_0^\infty \left\langle \bar{\mathbf{J}}^{(a)}(0)\cdot \bar{\mathbf{J}}^{(b)}(t)\right\rangle \mathrm{d}t \tag{5.29}$$

where

$$\bar{\mathbf{J}}^{(a)} = \bar{\mathbf{v}}^{(a)} - \bar{\mathbf{v}}^{(0)} \tag{5.30}$$

i.e. the velocity of the a-th species relative to the 0-th. Note

$$\bar{\mathbf{v}}^{(a)} \equiv \frac{1}{N^{(a)}}\sum_{\alpha\in\mathscr{G}^{(a)}} \mathbf{v}_\alpha = \frac{1}{M^{(a)}}\sum_{\alpha\in\mathscr{G}^{(a)}} m_\alpha \mathbf{v}_\alpha \tag{5.31}$$

Ionic electrical conductivity

$$\sigma = \frac{V}{3k_B T}\int_0^\infty \langle \mathbf{I}(0)\cdot\mathbf{I}(t)\rangle \mathrm{d}t \tag{5.32}$$

where $\mathbf{I}_0 = \frac{1}{V}\sum_\alpha q_\alpha \mathbf{v}_\alpha = \mathbf{I}$ for a system with zero barycentric velocity. Note $\mathbf{I}$ does not appear to be a constant of the motion.

$$\mathbf{I} = \frac{1}{V}\sum_\alpha q_\alpha \mathbf{v}_\alpha = \frac{1}{V}\sum_a q^{(a)}\sum_\alpha \mathbf{v}_\alpha^{(a)} = \frac{1}{V}\sum_a \frac{q^{(a)}}{m^{(a)}}\mathbf{J}^{(i)}$$

This formulation is in [28, Eqs. (11)&(12)] for a binary system, and [107, Eq. (29)] which is derived from the sum of the diffusion coefficients for a general electroneutral solution and *fluxes* $\mathbf{v}^{(a)} - \mathbf{v}^{(0)} = \sum_b L_0^{(a,b)}\mathbf{X}^{(b)}$.

5.2 Methods

To construct a computational method suitable for molecular dynamics, first microscopic quantities such as the electrical flux

$$\mathbf{i}(\mathbf{x}) = \sum_{\alpha} q_{\alpha}\mathbf{v}_{\alpha}\delta(\mathbf{x}-\mathbf{x}_{\alpha}) \tag{5.33}$$

must be defined. For the collective properties such as the electrical flux we just computed the sum of microscopic fluxes per cell. To minimize non-smoothness in time we have also employed a (continuous) partition of unity

$$\mathbf{J}(\mathbf{x}_I) = \frac{1}{V}\sum m_{\alpha}\mathbf{v}_{\alpha}\Delta(\mathbf{x}_{\alpha}-\mathbf{x}_I) \tag{5.34}$$

where $\Delta_I(\mathbf{x}) = \Delta(\mathbf{x}-\mathbf{x}_I)$ and $\sum_I \Delta_I(\mathbf{x}) \equiv 1$. A smooth PU creates overlap and therefore bin-to-bin correlation. For any PU, the correlation $\mathbf{J}(0,x_I)\cdot\mathbf{J}(t,x_I)$ for a single spatial coordinate x.

$$\langle \mathbf{J}(0)\mathbf{J}(t)\rangle = \left\langle \sum_I \mathbf{J}_I(0)\sum_J \mathbf{J}_J(t)\right\rangle = \sum_{I,J}\langle \mathbf{J}_I(0)\mathbf{J}_J(t)\rangle \tag{5.35}$$

so clearly the bin-to-bin spatial correlations can contribute to the estimate of a transport coefficient localized to any particular bin. Note Eq. (5.35) results from the partition across cells

$$\mathbf{J}(t) = \sum_I \mathbf{J}_I(t) \tag{5.36}$$

where

$$\mathbf{J}_I(t) = \sum_{\alpha\in\mathcal{N}_I(t)} \mathbf{j}_{\alpha}(t) \tag{5.37}$$

and $N = \cup_I \mathcal{N}_I(t)$.

Also note that, given that the system is in equilibrium, the net flux between partitions is zero $\left\langle \mathbf{J}_I^{(i)}\right\rangle = \mathbf{0}$. The center of mass is not zero instantaneously and jumps when particles enter/leave region. On average net outflux is zero and

$$\left\langle \mathbf{J}^{(i)}\right\rangle = \mathbf{0} \tag{5.38}$$

but the instantaneous flux is

$$\mathbf{J}^{(i)} = \sum_{\alpha} m_{\alpha}^{(i)}\mathbf{v}_{\alpha}^{(i)} + net\ influx \approx \frac{1}{\Delta t}\sum_{\alpha} m_{\alpha}^{(i)}\Delta\mathbf{x}_{\alpha}^{(i)} + \sum in - \sum out$$

5.3 Results

To test the method a homogeneous system was partitioned in to cells in one direction. Here the expectation is that all cells are statistically equivalent and that the estimate for the cell should

match, to within appropriate noise, the estimate for the whole system. For a solid-fluid system representing the electrode-electrolyte the expectation is that layers nearest to the wall are the least mobile and therefore have the lowest diffusion constants (and narrowest concentration peaks). Both simple Lennard-Jones fluids and systems with Si walls with extended water molecules were investigated.

5.3.1 Homogeneous ionic fluid

Using a Lennard-Jones (LJ) ionic fluid with 10:10:80 ratio of positive,negative and neutral species we see in Fig. 5.1 that the cell auto-correlations appear to match the whole system auto-correlation. Now if we examine the integral of the correlation, which is proportional to the estimate, we see from Fig. 5.2 that only with cell cross-correlations (i.e. off-diagonal entries of the coarse-grained spatial correlation matrix) does the cell estimates converge to the true, system value. Likewise, Fig. 5.3 shows that integral of the cell auto-correlation does converge to the system value if the bin size is large enough.

Other sensitivities were investigated. For instance, increasing the cell dimensions transverse to the open cell boundaries only decreased the noise in the cell estimates not their accuracy. Likewise, increasing the sampling frequency for the flux had the same effect. Interestingly the behavoir of the correlation of the flux normal to the open cell boundary was different than that transverse to the open cell boundary, i.e. in a periodic direction. For the saltwater system, Fig. 5.4 shows that the integral of the auto-correlation of the transverse fluxes has a well-defined limiting value; where as the integral of the auto-correlation of the normal fluxes does not. For the normal fluxes the correlations with the neighboring cells are need to get a good estimate, as the plot of the decay of the cell-to-cell spatial correlations Fig. 5.5 bears out.

Lastly, the effects of the omitting the long range Coulomb effects was investigated. Fig. 5.6 shows the expected result, i.e. the long range effects increase the cell-to-cell correlation length and therefore decrease the ability to resolve transport coefficients. Also, Fig. 5.7 shows the effects of changing the charge density. With lower charge concentration we get worse statistics and less screening i.e. longer correlation. Lower charge density also implies that it is less likelyfor ions to cross cell boundaries.

5.3.2 Solid-fluid system

For an overall neutral system with a charged Si wall and a TIP3 water with K^+ and Cl^- ions shown in Fig. 5.3.2 we were able to extract the spatial variation of viscosity, at least qualitatively. Fig. 5.9 shows the viscosity increases significantly near the walls as is expected from the fact that molecules at the walls are nearly immobile. We also see that the transverse and normal fluxes are giving different correlations which may indicate anisotropy in the transport coefficients.

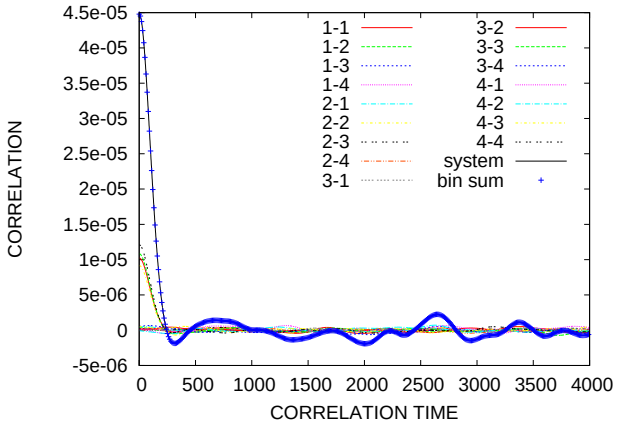

Figure 5.1. Cell auto-correlations match system auto-correlation for a homogeneous LJ system with short-range Coulomb interactions.

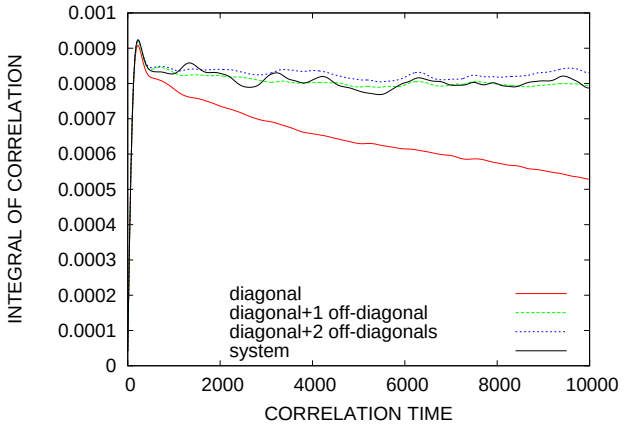

Figure 5.2. Convergence of the estimate with increasing number of diagonals of the correlation matrix for a homogeneous LJ system with short-range Coulomb interactions.

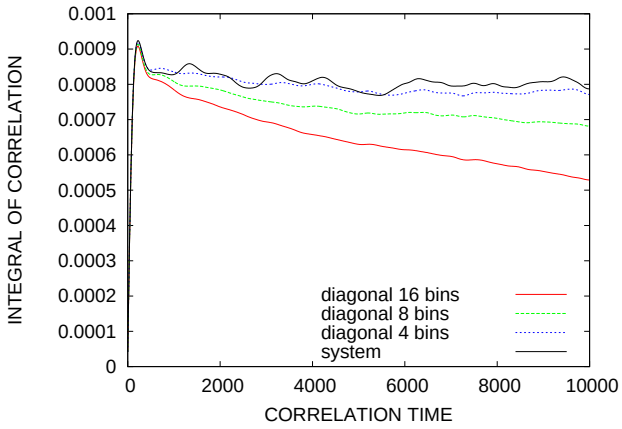

Figure 5.3. Convergence of the estimate with increasing cell size for a homogeneous LJ system with short-range Coulomb interactions.

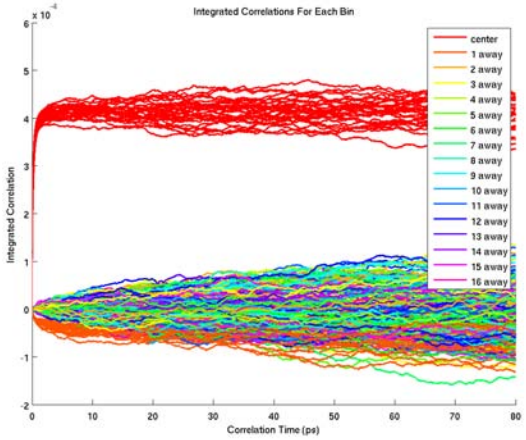

(a) mean of x and y (transverse) directions

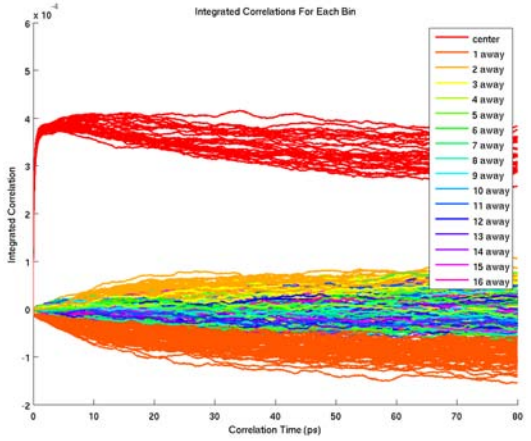

(b) z (cell normal) direction

Figure 5.4. Transverse vs. normal flux integrated correlations for each cell for a saltwater system

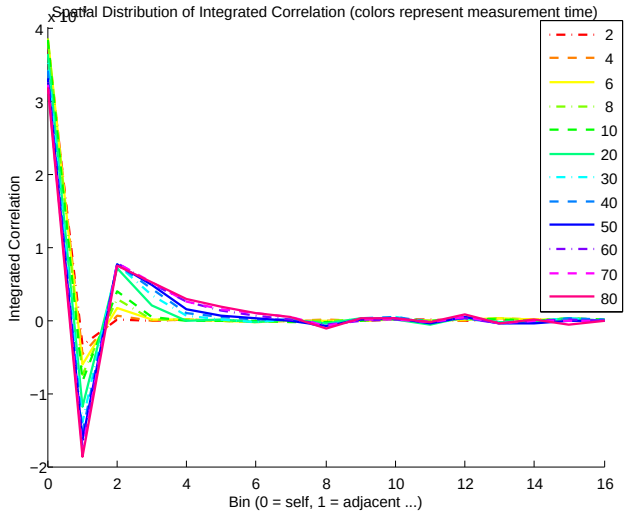

(a) mean of xy and yz (bin normal) directions

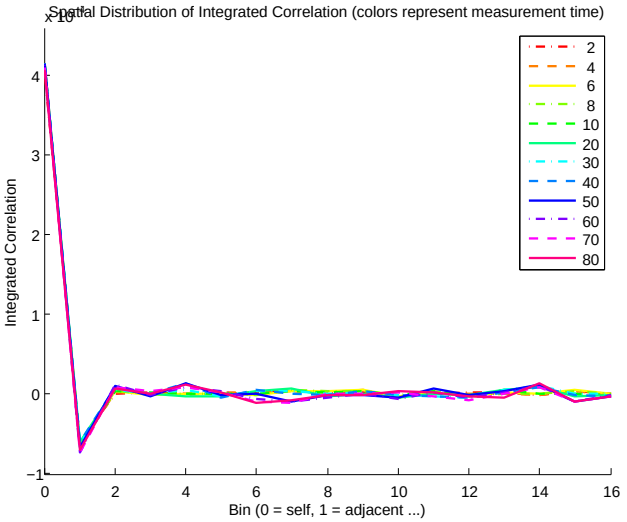

(b) xy (transverse) direction

Figure 5.5. Spatial distribution of transverse vs. normal integrated correlations for a saltwater system

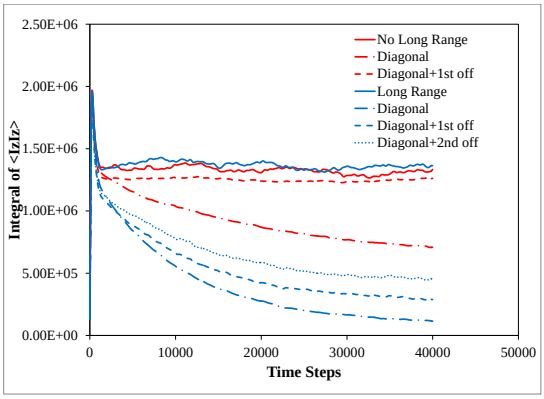

Figure 5.6. Convergence with Short-range vs. long-range Coulomb interactions

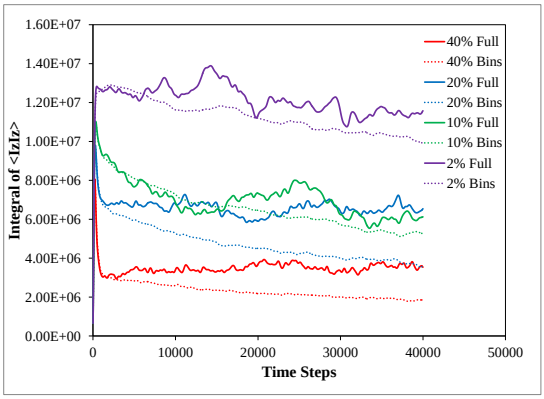

Figure 5.7. Sensitivity to charge density.

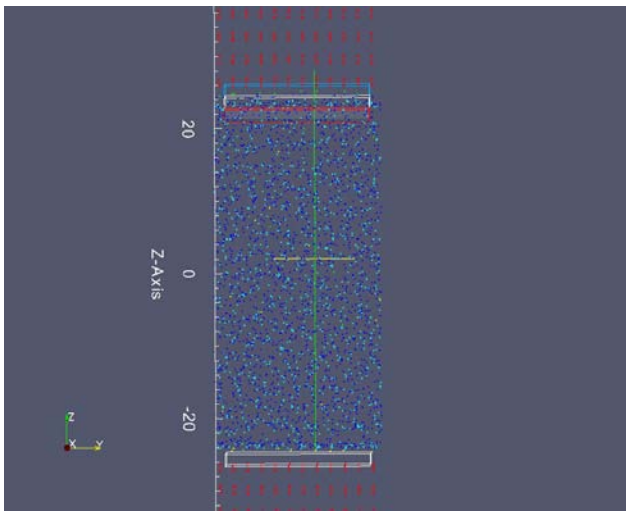

Figure 5.8. Wall-fluid system

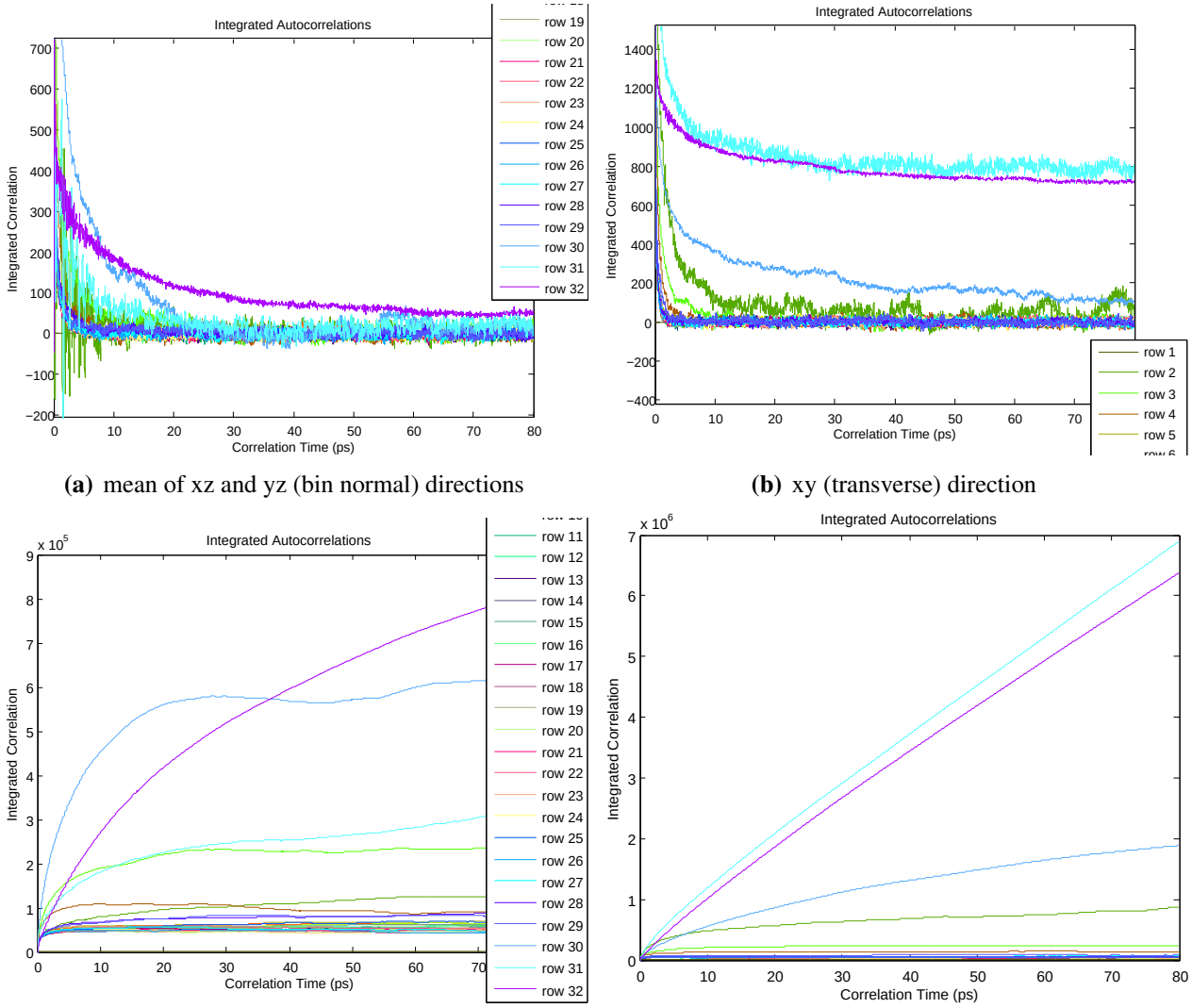

(a) mean of xz and yz (bin normal) directions

(b) xy (transverse) direction

(c) mean of xz and yz (bin normal) directions

(d) xy (transverse) direction

Figure 5.9. Cell autocorrelation and integrals of autocorrelation for a Si wall with TIP3 saltwater system

Chapter 6

Continuum Scale Constitutive Laws Extracted from Atomistic Simulations Using Bayesian Inference and Uncertainty Quantification

6.1 Introduction

Predictive simulation of engineering systems are often challenged by different phenomena operating over a broad range of length and times scales spreading from atomistic to continuum levels. Such phenomena are encountered for example in different engineering applications such as nanotechnology [25, 78, 54, 104, 112] and fluid dynamics [22, 50, 77, 5, 84, 37]. The ubiquity of such dynamics is illustrated by the need to supply constitutive relationships in mathematical models of physical phenomena to compensate for the unresolved degrees of freedom. For example, continuum mechanics can be derived from molecular mechanics [45, 41] in an average sense, but the missing degrees of freedom give rise to the complex constitutive relations found in solid mechanics, fluid mechanics, and heat transport. While combinations of experiments and theory can provide useful estimates of the impact of truncated information on the remaining degrees of freedom (examples: turbulence, solids), difficulties have been encountered when applying continuum theories at the atomistic scale, i.e., in the regimes when atomistic information becomes important. From a mathematical point of view, the challenge is that multiple scales, albeit without strict separation, are present everywhere in a domain rather than at on a lower dimensional manifold (e.g., interfaces and boundary layers). Developing accurate constitutive models for continuum descriptions of nanosystems has the potential to enable a new generation of devices characterized and optimized by predictive simulation.

As an illustration, the following observations are useful. Discretized continuum models always have a smallest resolved length sale associated with the mesh size. While mesh refinement can minimize this error and generate a family of solutions converging to the solution of the originating continuum equations, in reality the applicability of the equations breaks down as the discreteness of the atomistic processes becomes increasingly pronounced (e.g., [19]). In contrast, atomistic

The primary authors of this chapter are M. Salloum and J. Templeton.

simulations have a bounding length scale above as only a finite number of atoms can be simulated on a computer. As this length scale is increased, statistical mechanics increasingly accurately relates averages over the atomic system to established continuum quantities [116].

With this observation, the problem of constitutive modeling becomes one of a lack of multiscale information propagation. Several approaches have made progress at deriving constitutive relations from this perspective. Classical homogenization (e.g., [9]) focuses on deriving a governing equation for the large-scale field informed by the overall form of the equations and knowledge of the small scale field. Asymptotic analysis is used to extract the large-scale equations, so homogenization is usually only applicable to systems with two well-separated scales, although we do note recent efforts incorporating uncertainty in the large scale equations arising from the fine scale [68]. A computational analog is the heterogeneous multiscale method [21]. In this approach, molecular dynamics (MD) are instantiated at finite element (FE) quadrature points to compute the stress of a material. While effective, the drawbacks are potentially much larger simulation time with all MD evaluations as well as ambiguity regarding the length scale which should be used for the atomistic system. Within the context of FE methods, the variational multiscale method [44] has been used to modify constitutive models at particular scales and extended/enriched elements [64] add extra degrees of freedom to a system to account for specific small-scale behavior when known. Finally, the well-known dynamic Smagorinsky model for large-eddy simulation (LES) [30] uses scale similarity [33] to adaptively set the model coefficient.

There are also approaches which aim to directly reconstruct the missing small-scale information needed for the constitutive law. By using the known energy cascade in turbulence, a fractal-based model has been derived for LES to construct sub-grid velocity fields [12]. The necessary statistics are extracted from these fields and used to close the equations governing the resolved fluid motions. A different approach relies on application of an approximate filter inverse to estimate the total velocity field from the filtered (i.e., large-scale) motions [40]. However, it still relies on a Smagorinsky closure to account for the velocity fluctuations which cannot be represented on the grid under consideration.

For the purpose of this work, continuum descriptions are taken as appropriate models for physical systems at a macroscopic scale. As the macroscopic scale is taken smaller and smaller, it begins to approach the length scales of the microscopic, or atomic, system. Given the lack of a large scale separation between the atomistic and continuum descriptions, smaller-scale motions at the atomistic level give rise to larger-scale structures at the continuum level. Incomplete understanding of these sub-continuum processes leads to unresolved fluctuations at the continuum level, making application of existing modeling approaches problematic. There have been many efforts to develop techniques for combining atomistic and continuum representations, for example in solid mechanics (see the review article by Miller and Tadmor [63]), heat transfer [99, 7], and fluid mechanics [51, 66], although such methodologies are typically used for problems where the region requiring an atomistic description is (roughly speaking) on a lower-dimensional manifold than the over all system of interest, e.g., interfaces, cracks, and defects. In addition, most atomistic-to-continuum methods utilize continuum models based on macroscale behavior like Fourier's law. A notable exception is the concurrent coupling method for direct simulation Monte Carlo particles and continuum fluid mechanics of Donev *et al.* [20] which demonstrated that the Landau-

Lipfschitz Navier-Stokes equations, in which Brownian fluctuations are retained, are required to obtain an accurate solution to the overall problem. It is crucial therefore to derive such constitutive laws with their associated fluctuations directly informed from atomistic simulations to be appropriate models of the behavior of matter at the nanoscale.

Because of the difficulty in characterizing the mean and fluctuating components of the constitutive relations using existing means (even central limit theorems may not hold due to small sample sizes), atomistic simulations have to be performed to extract suitable constitutive laws. Figure 6.1 shows a one-dimensional version of such problem. The continuum simulation is characterized from a large length scale, L_c, down to the smallest resolved length scale representing the mesh size, h. The red dashed line illustrates an atomistic region of appropriate size to characterize the sub-continuum information at that mesh size level. A MD simulation is performed in order to extract suitable constitutive relationships between the problem variables.

Such an exercise should be performed on-the-fly during a large scale continuum simulation. This would result in a highly expensive cost of the overall simulation since many expensive MD simulations have to be performed in different regions in the computational domain over the course of the simulation. However, new advanced computer architectures [3] will have the power to realize such on-the-fly extraction of constitutive laws from MD simulations and can exploit extreme levels of concurrency for sampling-based methods. Before proceeding with such expensive simulations, it is expedient to first analyze and study the extraction of a constitutive law from MD simulations while accounting for the uncertainty due to finite sampling in MD simulations. The result of such study would be the derivation of the constitutive relationship between the physical entities in the simulation and the quantification of the uncertainty level associated with this relationship as a function of the system time and length scales.

In this paper, we focus on the study of a one-dimensional heat transfer problem at the nanoscale. This problem offers the advantages of being efficient to simulate on both atomistic and continuum scales while at the same time of sufficiently complex to develop a general constitutive law extraction methodology because the behavior of our atomistically-informed continuum can be compared to the true all atoms solution. We present an approach to extract the law that relates the heat flux to the temperature and temperature gradient from MD simulations, together with its associated uncertainty. The uncertainty we consider in this study is due to the intrinsic noise in MD simulations where finite sampling is required as well as the approximate nature of any continuum description. We seek methods that offer both flexibility and efficiency in order to propagate the uncertainty quantified in the constitutive law in continuum scale simulations. We assume that heat conduction is governed by Fourier law, that is the heat flux f is the product of the thermal conductivity κ and the temperature gradient ∇T,

$$f = -\kappa(T)\nabla T \tag{6.1}$$

where κ has a parametric dependency on the temperature T. We infer these parameters and express as polynomial chaos expansions (PCE) due to the facility with which they propagating uncertainty in continuum simulations [31, 56, 57, 55, 84]. We use Bayesian inference [29, 87, 62] to build the constitutive law. Bayesian inference has been found highly effective in handling different sources of uncertainty including noisy data typically obtained in MD simulations [80, 79]. We extract the heat conduction constitutive law and quantify its associated uncertainty as a function

of the spatial- and time-averaging scales and the amount of data used. This former are closely related to the time step and spatial discretization sizes in the continuum model. We then propagate the obtained constitutive law into a continuum scale simulation and compare with an equivalent simulation consisting only of atoms.

This paper is organized as follows. In section 6.2 the mathematical underpinnings of polynomial chaos expansions and Bayesian inference are provided. Section 6.3 overviews the molecular dynamics and multiscale methods used in this work. The mathematical formulation and specific formulation for the inferred conductivity is given in section 6.4 with results in provided in section 6.5.

6.2 Mathematical Background

6.2.1 Polynomial Chaos Expansions

We consider random entities parameterized by a finite collection of real-valued independent and identically distributed (*i.i.d.*) random variables $\xi_1, \ldots, \xi_n$ that share a common distribution function, $\mathscr{P}$. If, for example, ξ is a standard normal random variable on Ω, we write $\xi \sim \mathscr{N}(0,1)$ and $\mathscr{P}_\xi(x) = \frac{1}{\sqrt{2\pi}} e^{-x^2/2}$ is the Probability Density Function (PDF) of ξ. Any random variable admits an expansion of the form:

$$u = \sum_{k=0}^{\infty} u_k \Psi_k(\mathbf{1}), \tag{6.2}$$

where the $\{\Psi_k\}_{k=0}^{\infty}$ is an orthogonal basis with respect to the density of $\mathbf{1} = (\xi_1, \ldots, \xi_n)$,

$$\langle \Psi_k \Psi_l \rangle = \int_\Omega \Psi_k(\mathbf{x}) \Psi_l(\mathbf{x}) \mathscr{P}_\mathbf{1}(\mathbf{x}) d\mathbf{x} = \delta_{kl} \langle \Psi_k^2 \rangle \tag{6.3}$$

where δ_{kl} is the Kronecker delta. The expansion (6.2) is known as the polynomial chaos expansion (PCE) [109, 13, 46, 31, 55] of u. A common case, and the one considered in this work, takes $\xi_i \overset{iid}{\sim} \mathscr{N}(0,1)$ with $\{\Psi_k\}_{k=0}^{\infty}$ being n-variate Hermite polynomials [4]. In practical computations, we approximate $u(\mathbf{1})$ with a truncated series,

$$u(\mathbf{1}) \approx \sum_{k=0}^{P} u_k \Psi_k(\mathbf{1}), \tag{6.4}$$

where P is finite and depends on the truncation strategy adopted. We consider truncations based on the total degree of the retained polynomials in the series, such that P is a function of the stochastic dimension n and expansion order p according to:

$$P + 1 = \frac{(n+p)!}{n!p!}. \tag{6.5}$$

Here p refers to the largest polynomial degree in the expansion. One way to derive the polynomial chaos (PC) coefficients of u is by projection on the PC basis following:

$$u_k = \frac{\langle u\Psi_k \rangle}{\langle \Psi_k^2 \rangle}, \qquad k = 0, \ldots, P. \tag{6.6}$$

This approach is referred to as non-intrusive spectral projection (NISP) [55] and requires numerical evaluation of the projection integrals $\langle u\Psi_k \rangle$ using quadrature rules. An alternate strategy involves computing PC coefficients using Bayesian inference, which will be introduced in the following section.

6.2.2 Bayesian Inference

Let $\mathbf{1} \in \Omega$ denote a vector of model parameters and $\mathbf{1}$ a vector of observable data. A forward model Γ relates the data $\mathbf{1}$ to the parameters $\mathbf{1}$ by $\mathbf{1} \approx \Gamma(\mathbf{1})$ [62]. We use Bayes' rule to derive the posterior PDF for the model parameters $\mathbf{1}$ given the observed data $\mathbf{1}$ [62, 87]:

$$\mathscr{P}(\mathbf{1}|\mathbf{1}) = \frac{\mathscr{P}(\mathbf{1}|\mathbf{1})\mathscr{P}(\mathbf{1})}{\int_\Omega \mathscr{P}(\mathbf{1}|\mathbf{1})\mathscr{P}(\mathbf{1}) d\mathbf{1}} \tag{6.7}$$

The prior $\mathscr{P}(\mathbf{1})$ and posterior $\mathscr{P}(\mathbf{1}|\mathbf{1})$ probabilities represent degrees of knowledge of $\mathbf{1}$ *before* and *after* observing the data $\mathbf{1}$, respectively. The denominator in (6.7) is independent of $\mathbf{m}$ and is merely a normalizing constant for the purposes of this work. The key component in (6.7) is the likelihood function $L(\mathbf{m}) = \mathscr{P}(\mathbf{1}|\mathbf{1})$. To construct the likelihood, one needs to make assumptions regarding the distribution of the discrepancy between the model prediction and the data. Assuming that a forward model Γ predicts N realizations of the data $\mathbf{1}$ with a discrepancy $\mathbf{1} = [\varepsilon_1, \varepsilon_2, \cdots, \varepsilon_N]^T$ distributed according to the PDF $\mathscr{P}_\mathbf{1}(\cdot)$, *i.e.* $\mathbf{1} = \Gamma(\mathbf{1}) + \mathbf{1}$, we can write the likelihood as:

$$\mathscr{P}(\mathbf{1}|\mathbf{1}) = \mathscr{P}_\mathbf{1}(\mathbf{1} - \Gamma(\mathbf{1})). \tag{6.8}$$

Further, if $\{\varepsilon_i\}_{i=1}^N$ are *i.i.d.* with $\varepsilon_i \sim \mathscr{P}_\varepsilon(\cdot)$ (a condition which holds in the present context, as explained when used later below) then we have:

$$\mathscr{P}(\mathbf{1}|\mathbf{1}) = \prod_{i=1}^{N} \mathscr{P}_\varepsilon(d_i - \Gamma(\mathbf{1})) \tag{6.9}$$

In the present paper, we apply this Bayesian inference machinery to extract the heat conduction constitutive law from noisy MD simulations data. We infer the polynomial coefficients of the temperature dependent thermal conductivity (see Section 6.4.1). The Bayesian inference approach is preferred over the NISP methods (see Section 6.2.1) when inferring PC coefficients because it is more suitable in the presence of noisy data [80]. The NISP approach partially accounts for the noise information while the Bayseian approach fully captures the uncertainty due to noise in terms of probability density functions (PDF) for each PC coefficient. Starting from prior knowledge on these coefficients and given data $\mathbf{1}$ in the likelihood function, the posterior distribution calculated using (6.7) includes better knowledge of these coefficients.

6.3 MD Simulation

6.3.1 Simulation Domain Geometry and Setup

Figure 6.2 shows a stationary quasi-1D bar simulated by MD as a three-dimensional domain of size $L_a \times w \times w$ in the x, y, and z directions, respectively. MD computations were performed with LAMMPS [71] atomic simulator. The domain is occupied by Argon atoms with mass 39.95 g/mol with a lattice constant of $\alpha = 5.405$ Åand width $w = 3.24$ nm. The soft interparticle interaction is modeled by the Lennard-Jones (LJ) pairwise potential ϕ_{ij} [6, 58, 26]. For particles i and j separated by a distance r_{ij}, ϕ_{ij} is given by:

$$\phi_{ij} = 4\phi_0 \left[\left(\frac{\rho}{r_{ij}} \right)^{12} - \left(\frac{\rho}{r_{ij}} \right)^{6} \right] \tag{6.10}$$

We set the LJ parameters for Argon to $\phi_0 = 0.238$ Kcal/mole and ρ =3.405 Å [6], and atomic motions are resolved with a time step size of $\Delta t_a = 2$ fs. The boundary conditions are periodic in the y and z.

This MD simulation is intended to simulate a quasi-1D heat transfer problem, thus we must impose Dirichlet boundary conditions at $x = 0$ and $x = L_a$. To do so, we use the atomistic-to-continuum formalism initially proposed by Wagner *et al.* [100] to partition the domain using a FE mesh. Partitioning enables both the identification of a local temperature using FE projection, as well as imposition of localized temperature constraints via the FE shape functions. Temperatures are held fixed by augmenting the atomic forces from the interatomic potential by deriving a Lagrange multiplier which takes the form of a Gaussian isokinetic thermostat which varies on the length scale of the elements [93]. Specifically, the force on atom α is

$$\mathbf{f}_\alpha = \frac{\partial \Phi}{\partial \mathbf{x}_\alpha} - \frac{m_\alpha}{2} \mathbf{v}_\alpha \sum_I N_I \lambda_I, \tag{6.11}$$

where N_I is the shape function associated with node I and λ_I are the nodal Lagrange multipliers. To set up the temperature gradient, we constrain the temperature of the atoms where $0 \leq x \leq L_b$ (red region) such that it is fixed at $T = T_{MD,1}$ while at $L_a - L_b \leq x \leq L_a$, the temperature is constrained to be $T = T_{MD,N}$, which is effected by setting $\lambda_I = 0$ for all I except for $I = 1, N$.

The simulation is divided into three main parts. Argon atom are positions are on a FCC regular grid in a minimum energy configuration with initial velocities randomly assigned such that the initial (total) temperature of the system is equal to $T = T_{MD,N}$. The simulation is first run for 2000 fs until the initial temperature reaches a statistical steady state using the localized rescaling thermostat of [100]. Next, the localized temperature constraint is applied. The temperature at node 1 is ramped from $T_{MD,N}$ to $T_{MD,1}$ over 2000 fs, after which the system is allowed to come to a steady state. This simulation time is proportional to L_a^2. Finally short-time averaged samples of the heat flux q, ∇T and T are collected at the mesh points using the coarse-graining postprocessor of Zimmerman *et.al.* [116] until the noise amplitude due to finite sampling is reduced below a desired threshold.

6.3.2 Thermal Fields

The heat flux q, temperature gradient ∇T, and temperature T extracted at $x = L_a/2$ as a function of MD simulation time are shown in Figure 6.3. For $L_a = 53$ nm, it takes about 3 ns for the temperature of the system to reach a statistial state where the amplitude of the velocity noise decreases with increasing the averaging time window. The mean of the heat flux remains constant throughout the simulation, as expected. The short-term averaged data for $t_a > 3$ ns is used in the inference of the heat conduction constitutive law as further described in this paper.

Figure 6.4 depicts the thermal steady state of the quasi 1D-bar. Higher temperatures cause higher atoms velocities thus, the noise level decreases when the temperature decreases from $T_{MD,1} =$ 60 K to $T_{MD,N} = 40$ K. We compute the thermal conductivity κ as the opposite of the short-term averaged flux divided by the short-term averaged temperature gradient. This exercise results in a significant increase in the noise level since the value of temperature gradient samples could be close to zero. When plotting this κ as a function of temperature, it is not surprising to observe that it takes negative values, since unlike the continuum scale at such low atomistic time scale there is a substantial probability that the heat flux is in the same direction as the temperature gradient. The negative values decreases with increasing time averaging window, as expected, and the PDF of κ approaches a log-normal distribution.

6.4 Mathematical Model Formulation

6.4.1 Building the Heat Conduction Constitutive Law

For given L_a, $T_{MD,1}$ and $T_{MD,2}$, we extract the thermal entities q, ∇T and T at M mesh points and gather N_t short-time averaged samples of each of these three entities after the simulation reaches a statistical steady state. As such, we obtain $N_d = MN_t$ independent noisy samples $\{q_j, \nabla T_j, T_j\}_{j=1}^{N_d}$. We use these samples as data in a Bayesian inference process to determine the posterior distribution on the parameters that relate q, ∇T and T.

In this approach we assume that heat conduction is governed by Fourier's law that is the heat flux q is the product of a temperature dependent thermal conductivity κ and the temperature gradient ∇T. According to Figure 6.4, κ a nearly decreasing trend with temperature thus, we assume the following relationship:

$$\begin{aligned} \kappa &= A - BT \\ q &= -(A - BT)\nabla T \end{aligned} \tag{6.12}$$

where A and B and their associated uncertainty are to be determined by the Bayesian inference machinery. We assume a Gaussian noise model that relates A and B to the short-time averaged

samples $\{q_j, \nabla T_j, T_j\}$ such that:

$$\begin{aligned} q_j &= -(A - BT_j)\nabla T_j + \sigma\eta_j \\ &= -A\nabla T_j + BT_j\nabla T_j + \sigma\eta_j \end{aligned} \tag{6.13}$$

where the *i.i.d.* standard normals η_j represent the noise in the short-term MD sample averages, an assumption based on the central limit theorem (CLT). The variance σ^2 of the discrepancy is related to the fluctuation in the flux which level depends on the temperature. σ^2 is expected to decrease inversely proportional to the number of samples N and will be inferred as a hyperparameter [65, 62] along with A and B. Bayes' rule is then written as:

$$\mathscr{P}(A, B, \sigma^2|\mathbf{1}, \underline{d}) \propto \mathscr{P}(\mathbf{1}, \underline{d}|A, B, \sigma^2)\mathscr{P}(A, B, \sigma^2) \tag{6.14}$$

where $\mathbf{1} \in \mathbb{R}^N$ is the heat flux data q_j and $\underline{d} \in \mathbb{R}^{N\times 2}$ is a matrix containing the temperature and temperature data obtained from the MD simulations such that $\underline{d}_j = (-\nabla T_j, T_j\nabla T_j)$. Note that we assume that the inference relies on a constant σ noise model even though the noise level changes with temperature. The inferred value of σ would be then correspond to the fluctuations at the mean mean temperature in the MD system.

The likelihood function based on 6.14 is written as:

$$\mathscr{P}(\mathbf{1}, \underline{d}|A, B, \sigma^2) = (2\pi\sigma^2)^{-N/2}\exp\left(-\frac{\mathbf{1}^T\mathbf{1}}{\sigma^2}\right) \tag{6.15}$$

where the elements of the discrepancy vector $\mathbf{1}$ are given by:

$$\begin{aligned} \varepsilon_j &= \sigma\eta_j \\ &= q_j + (A - BT_j)\nabla T_j \end{aligned} \tag{6.16}$$

We assume independent priors for A, B and σ^2, *i.e.* $\mathscr{P}(A, B, \sigma^2) = \mathscr{P}(A)\mathscr{P}(B)\mathscr{P}(\sigma^2)$ and assign to both A and B an improper uniform prior [87] on $[-\infty, +\infty]$. For the hyperparameter, σ^2, leveraging the fact that there is a complete *a-priori* ignorance about its value except that it cannot be negative, we assume a Jeffreys prior:

$$\mathscr{P}(\sigma^2) = \frac{1}{\sigma^2} \tag{6.17}$$

If the likelihood (6.15) incorporates a large amount of data then the joint prior has a minimal role in the resulting posterior. Conversely, if the likelihood function only brings a small amount of data, the distribution of the resulting posterior is comparable to the prior. The effect of the amount of data will be discussed in Section 6.5.

Based on the chosen priors and the Gaussian noise model, the corresponding posterior over $\{A, B\}$ is a Student-t distribution [81, 39, 84] $\mathscr{S}(\gamma, \mathbf{1}, \underline{\mathbb{S}})$ where the mean vector $\mathbf{1}$, the number of

degrees of freedom γ and the scale matrix $\underline{\mathsf{S}}$ are given by [84]:

$$\begin{aligned}
\mathbf{1} &= \underline{\nu d}\mathbf{1} \\
\gamma &= N-2 \\
\underline{\mathsf{S}} &= \frac{1}{\gamma}\left(\mathbf{1}^T\mathbf{1}-\mathbf{1}^T\underline{d}\mathbf{1}\right)\underline{\nu} \\
\underline{\nu} &= \left(\underline{d}^T\underline{d}\right)^{-1}
\end{aligned} \tag{6.18}$$

Thus we can express A and B as:

$$\begin{pmatrix} A \\ B \end{pmatrix} = \mathbf{1} + \underline{\Lambda}\mathbf{1} \sim \mathscr{S}(\gamma, \mathbf{1}, \underline{\mathsf{S}}) \tag{6.19}$$

where $\underline{\Lambda} \in \mathbb{R}^{2\times 2}$ is the lower-triangular Cholesky factor of the scale matrix $\underline{\mathsf{S}} = \underline{\Lambda}\underline{\Lambda}^T$, and the vector $\mathbf{1} \in \mathbb{R}^2$ comprises *i.i.d.* random variables distributed according to $\mathscr{S}(\gamma, 0, 1)$. For large values of N_d, the Student-t distribution $\mathscr{S}(\gamma, 0, 1)$ approaches the normal distribution $\mathscr{N}(0, 1)$, such that, in this limit, $\mathscr{P}(A, B|\mathbf{1}, \underline{d})$ is close to a binormal distribution. A and B are finally written as a first order ($p = 1$) PCEs with two stochastic dimensions ($n = 2$) representing the finite sampling noise [84]:

$$\begin{aligned}
A &= \mu_1 + L_{11}\xi_1 \\
B &= \mu_2 + L_{21}\xi_1 + L_{22}\xi_2
\end{aligned} \tag{6.20}$$

where ξ_1 and ξ_2 follow $\mathscr{N}(0, 1)$ for large N_d. The thermal conductivity $\kappa = A - BT$ thus becomes an uncertain variable. Our main goal is to propagate this uncertainty in continuum simulation. However, since both A and B follow a Student-t distribution, they can take any value in $[-\infty, +\infty]$ allowing for κ to have negative values that are not defined in continuum. Thus, additional operations have to be performed on the distributions of A and B to enforce their positivity.

Enforcing the Positivity of the Thermal Conductivity

The mathematics of the diffusion equation require a positive thermal conductivity everywhere. However, the procedure described above would result in negative values as, due to nanoscale fluctuations, the heat flux follows the temperature gradient with non-zero probability. In order to guarantee solutions exist for the continuum heat transport equations, we propose a set operations on the distributions of A and B that simultaneously allow enforcing the positivity of $\kappa = A - BT$ for a given range $T_{MD,2} \leq T \leq T_{MD,1}$. The effect of the procedures is to build new distributions for A and B (continuum formulations without these descriptions will be the subject of future work). We proceed as follows:

1. We draw a large number, N_s, of realizations $(A, B)_i$ from the Student-t distributions of A and B derived in Section 6.4.1.

2. We eliminate from this set of realizations all the $(A,B)_i$ that satisfy $A_i - B_i T_{MD,2} < 0$ or $A_i + B_i T_{MD,1} < 0$.

3. Using Kernel Density Estimation (KDE) [11, 84], we build new distributions for A and B from the remaining realizations.

Remark #1 Another method to enforce the positivity of $\kappa = A - BT$ is to assign an appropriate prior on A and B in the Bayesian inference procedure in Section 6.4.1. The prior expression would then be:

$$\begin{aligned} \mathscr{P}(A,B) &= 0, \quad \text{for} \quad A - BT_{MD,2} < 0 \quad \text{or} \quad A + BT_{MD,1} < 0 \\ \mathscr{P}(A,B) &= \frac{1}{(A_{max} - A_{min})(B_{max} - B_{min})}, \quad \text{otherwise} \end{aligned} \tag{6.21}$$

where A_{max}, A_{min}, B_{max} and B_{min} determine a known range of variation of A and B. This approach however, does not allow an analytical derivation for the distribution of A and B. It requires sampling the posterior in Eq. 6.14 using the Markov Chain Monte Carlo method that is more expensive and complicated than the method described above.

Remark #2 The initial number of realizations N_s should be large enough such that after eliminating the $(A,B)_i$, the number of the remaining realizations is sufficient for statistical significance of the resulting distribution.

Spectral Projection of the Thermal Conductivity

The distributions of A and B obtained in Section 6.4.1 are not guaranteed follow any of the traditional distributions such as normal, log-normal, uniform, etc., particularly for the smaller sample sizes. Thus, the representation of the random variables A and B as PCEs requires high order polynomials. We first employ a RosenBlatt transform to map the jointly distributed random variables A and B (after enforcing the positivity of their corresponding κ) into two independent uniform random variables. We then apply an approximate inverse RosenBlatt to compute the PC coefficients of A and B at a given expansion order. These operations are further detailed in the work of Sargsyan *et.al.* [85, 86]. In this work we found that a fourth order expansion ($p = 4$) with one stochastic dimension ($n = 1$) can accurately represent both A and B. Hence, after enforcing the positivity of κ, A and B are written as:

$$\begin{aligned} A &= \sum_{k=0}^{4} A_k \psi_k(\xi) \\ B &= \sum_{k=0}^{4} B_k \psi_k(\xi) \end{aligned} \tag{6.22}$$

where the ψ_ks are Hermite polynomials given in [32, 55]

6.4.2 Propagating the Uncertain Constitutive Law into the Continuum Simulation

In this section we propagate the uncertainty in the thermal conductivity κ quantified in the previous section into a 1-D continuum problem.

$$\rho c_p \frac{\partial T}{\partial t} = \frac{\partial}{\partial x}\left[-(A - BT)\frac{\partial T}{\partial x}\right] \tag{6.23}$$

6.5 Results

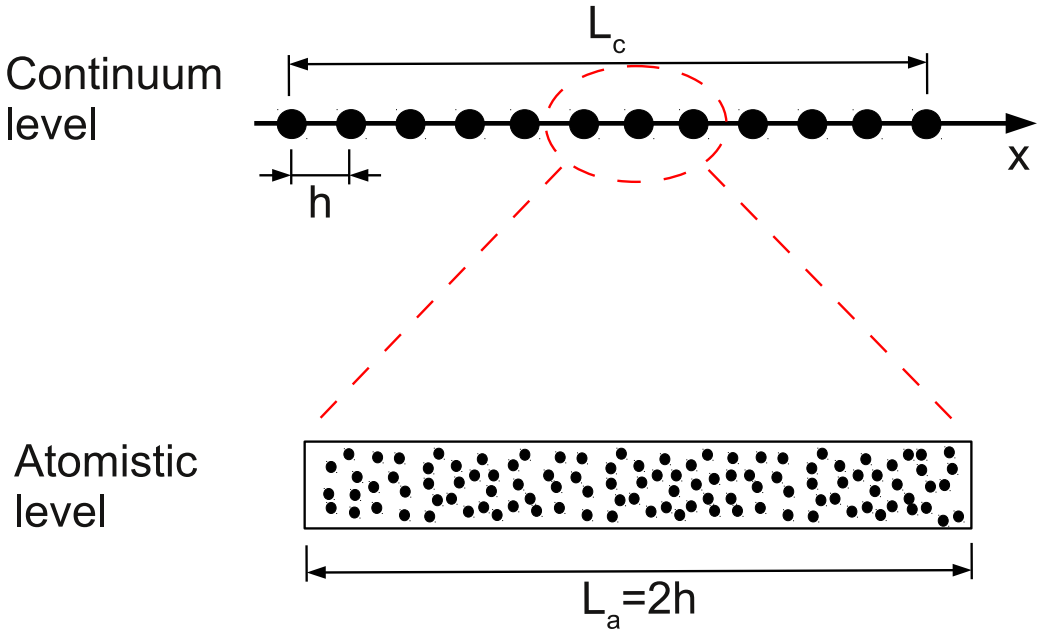

Figure 6.1. A schematic showing: (top) a one-dimensional continuum level finite element simulation domain characterized by a length scale L_c, a time scale τ_c and a mesh size h, and (bottom) an atomistic scale simulation domain characterized by a length scale $L_a = 2h$ and a time scale τ_a, where atomistic information is required to quantify physical phenomena that are beyond the reach of the continuum description.

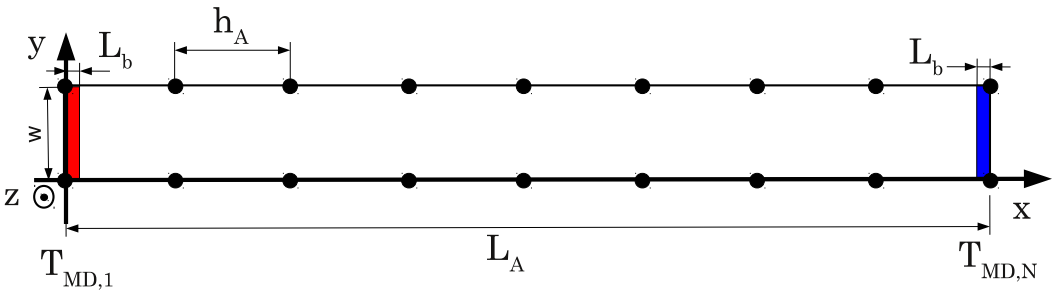

Figure 6.2. A schematic showing the MD simulation domain. The temperature is constrained in the red and blue regions to be $T = T_{MD,1}$ and $T = T_{MD,N}$, respectively. The black dots represent mesh points where the local heat flux, temperature gradient and temperature are extracted using the formalism of Zimmerman *et.al.* [116].

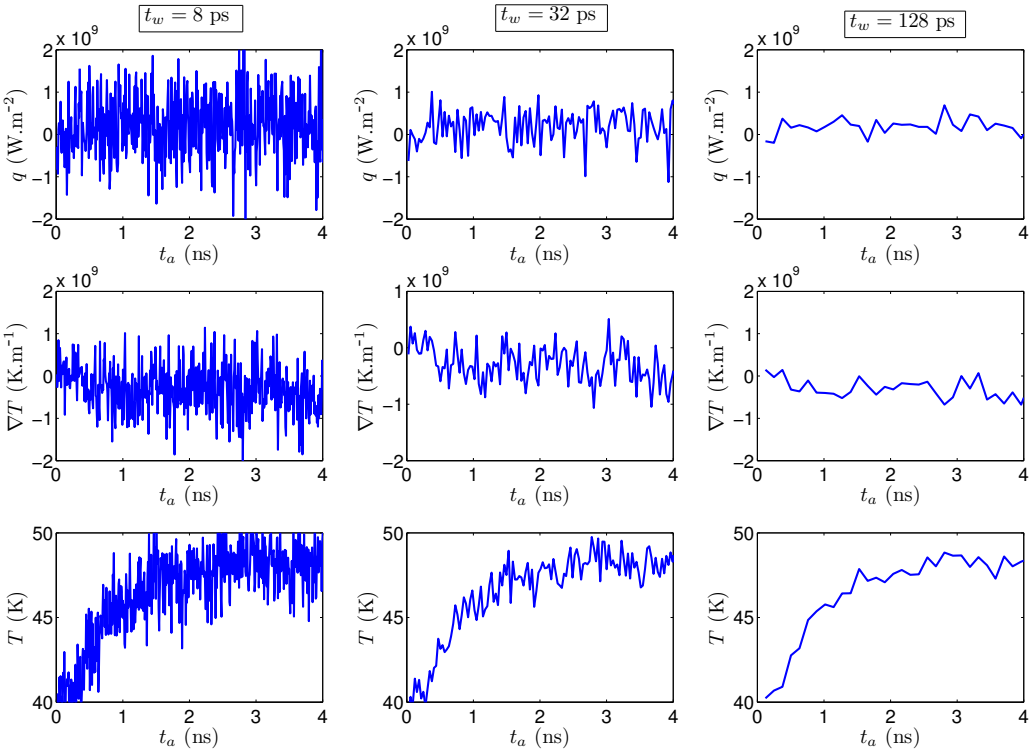

Figure 6.3. Plots showing short-time averaged heat flux q, temperature gradient ∇T, and temperature T extracted at $x = L_a/2$ from the MD simulation as a function of time for $T_{MD,1} = 60$ K, $T_{MD,N} = 40$ K and $L_a = 53$ nm, and different moving time averaging window widths, as indicated. Note for the method being used to apply the temperature gradient [93], the flux is expected to be a constant.

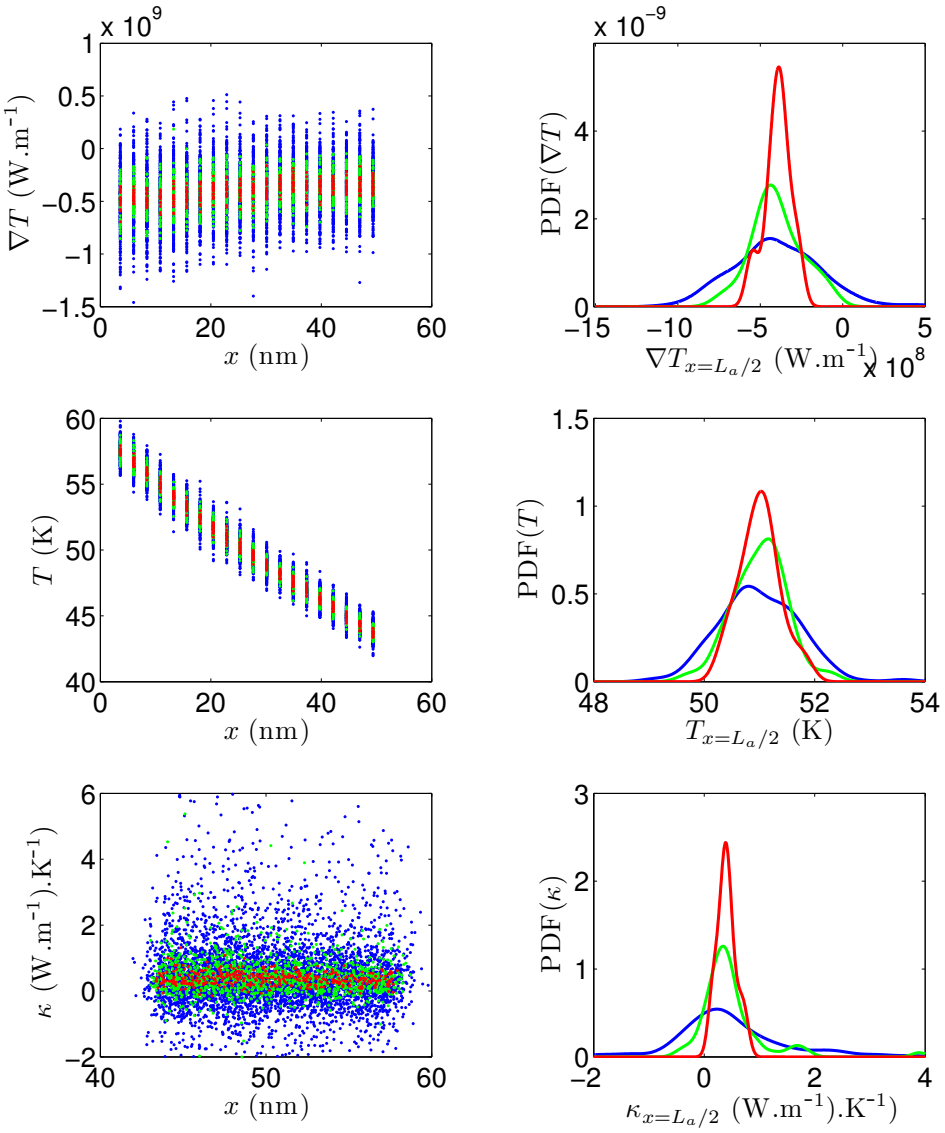

Figure 6.4. Plots showing (Left column): (top) temperature gradient field ∇T in the quasi-1D bar, (middle) temperature field T in the quasi-1D bar, (bottom) thermal conductivity κ as function of temperature, (Right column): the PDFs of ∇T, T and κ at $x = L_a/2$. Results are generated from the MD simulation for $T_{MD,1} = 60$ K, $T_{MD,N} = 40$ K and $L_a = 53$ nm when the statistical steady state is reached for different moving time averaging window widths, as indicated.

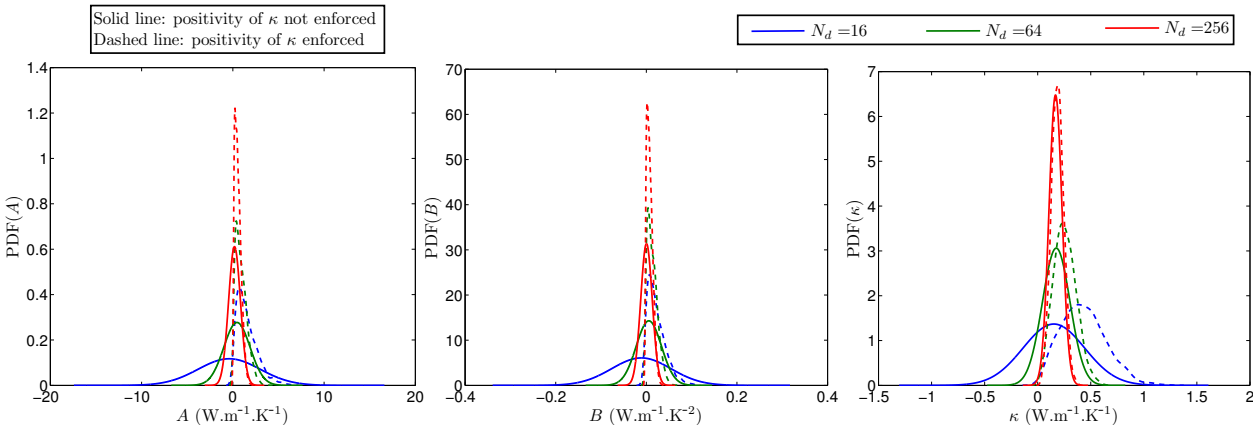

Figure 6.5. Plots showing the PDFs of: (left) the inferred coefficient A, (middle) the inferred coefficient B, and the corresponding the thermal conductivity κ for T =50 K. Results are obtained from data averaged at t_w =8 ps using 4 replica MD simulations for $T_1 = 60$ K, $T_2 = 40$ K and $L_a = 53$ nm. Plotted are the PDFs of the coefficients before (solid line) and after (dashed line) enforcing the positivity of κ for different amounts N_d of data used for the inference.

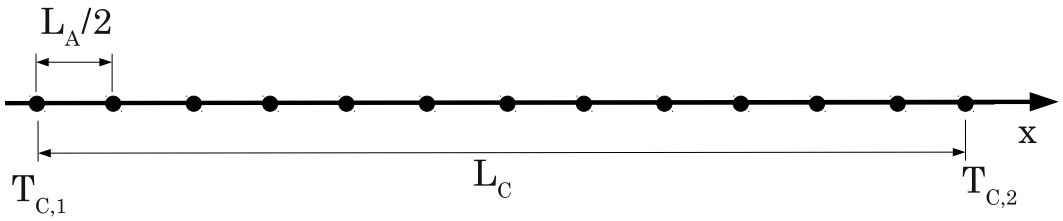

Figure 6.6. A schematic showing the 1-D continuum simulation domain. The temperature is controlled such that it fluctuates in the red and blue regions around $T = T_{C,1}$ and $T = T_{C,2}$, respectively. The black dots represent mesh points.

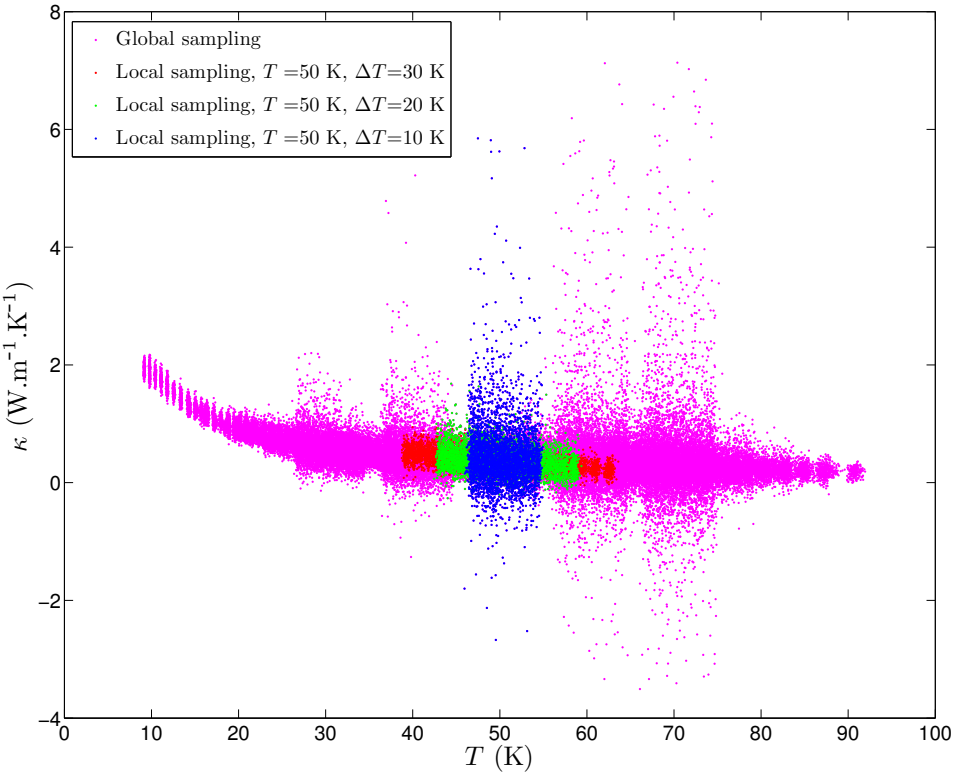

Figure 6.7. Plot showing short-time averaged values of the thermal conductivity $\kappa_j = -q_j/\nabla T_j$ as a function of the temperature T_j. Results are obtained from data averaged at t_w =512 ps, using 4 replica MD simulations for different ranges of temperature by local and global sampling of the $\{\Delta T, T\}$ space, as indicated.

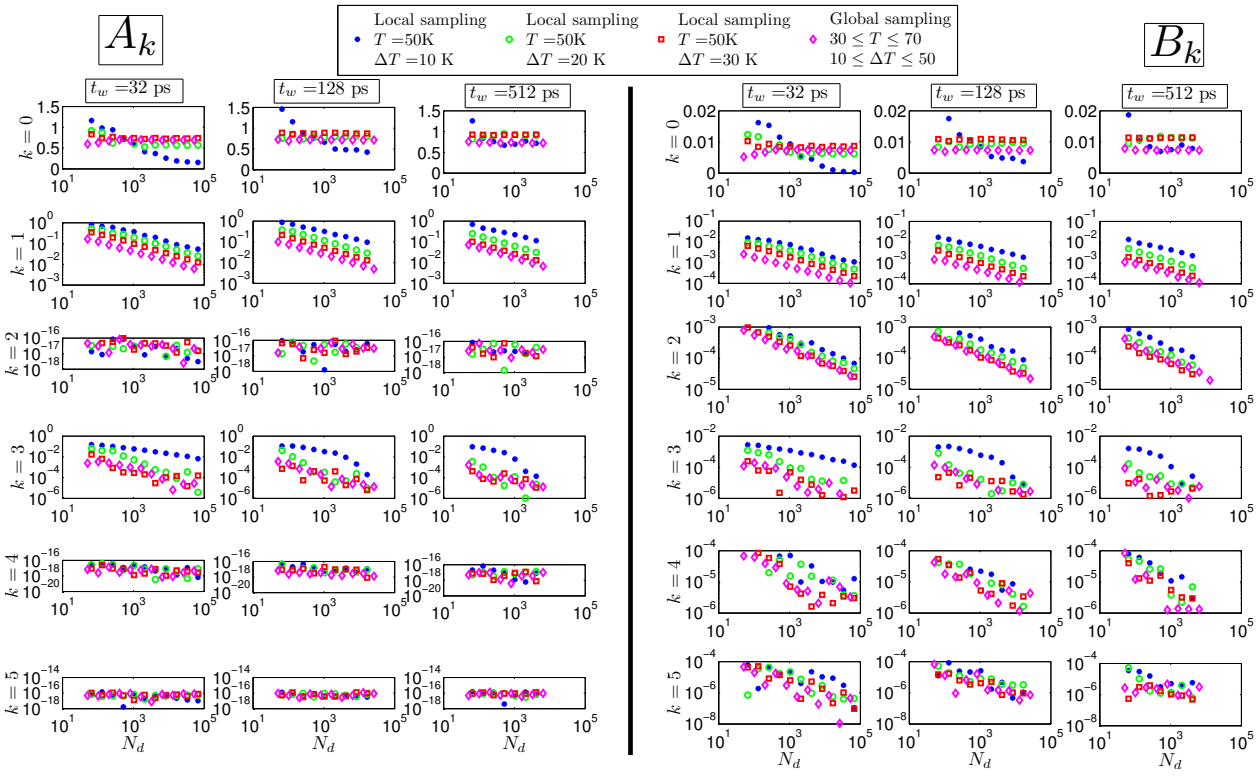

Figure 6.8. Plots showing the PC coefficients as a function of the amount N_d of data used for the inference of: (left panel) the inferred coefficient A, and (right panel) the inferred coefficient B. Results are obtained from data averaged at different values of t_w, using 4 replica MD simulations for different ranges of temperature by local and global sampling of the $\{\Delta T, T\}$ space, as indicated.

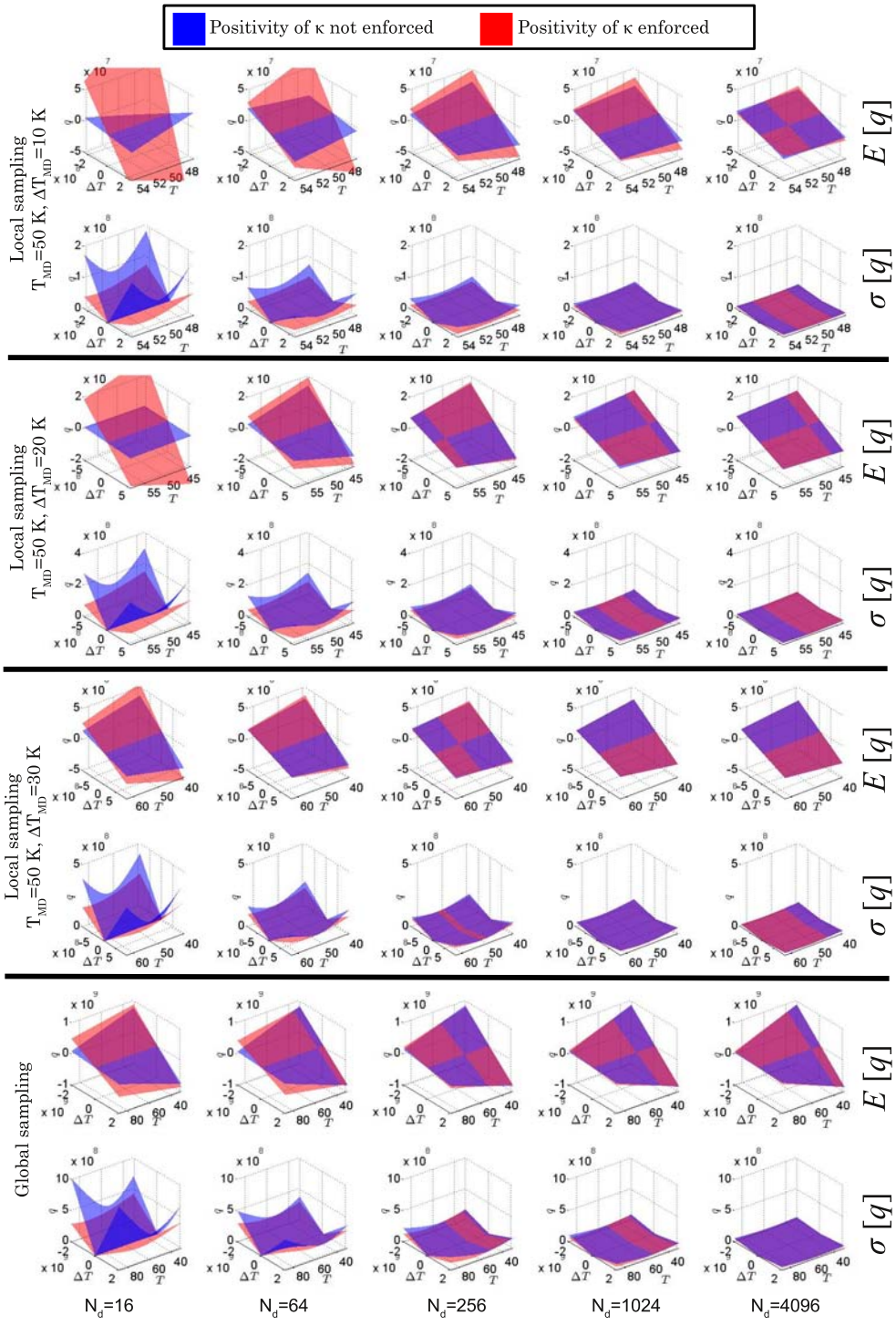

Figure 6.9. Plots showing the expectation E and standard deviation σ of the flux $q = (A - BT)\Delta T$ surface obtained after the inference of A and B, as a function of the amount N_d of $(q_j, \nabla T_j, T_j)$ data. Results are obtained from data averaged at t_w =8 ps, using 4 replica MD simulations for different ranges of temperature by local and global sampling of the $\{\Delta T, T\}$ space, as indicated. q is given in Wm^{-2}, ∇T in Km^{-1} and T in K.

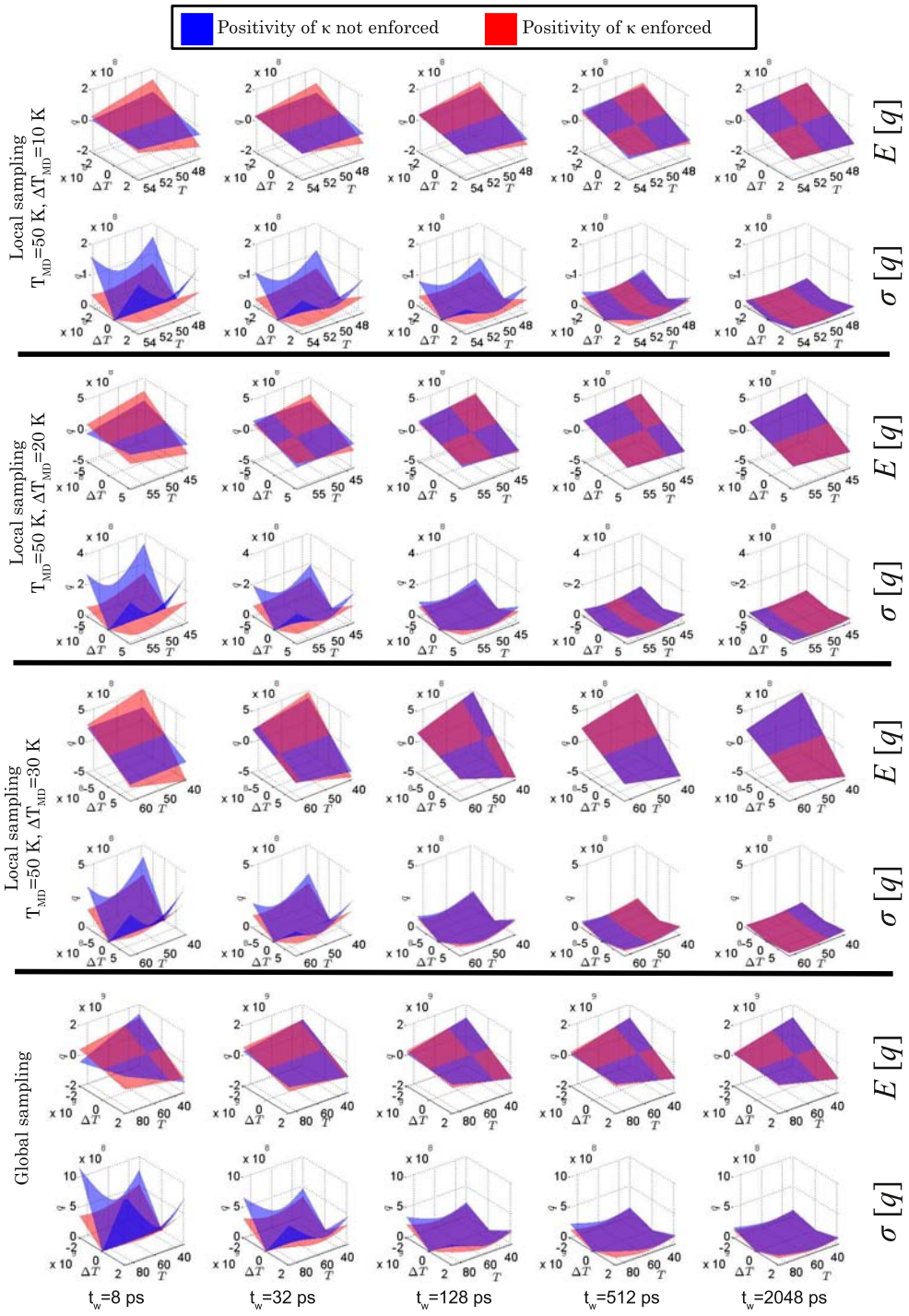

Figure 6.10. Plots showing the expectation E and standard deviation σ of the flux $q = (A - BT)\Delta T$ surface obtained after the inference of A and B, as a function of the amount time averaging window t_w. Results are obtained from $N_d = 16$ short-time averaged $(q_j, \nabla T_j, T_j)$ data, using 4 replica MD simulations for different ranges of temperature by local and global sampling of the $\{\Delta T, T\}$ space, as indicated. q is given in Wm^{-2}, ∇T in Km^{-1} and T in K.

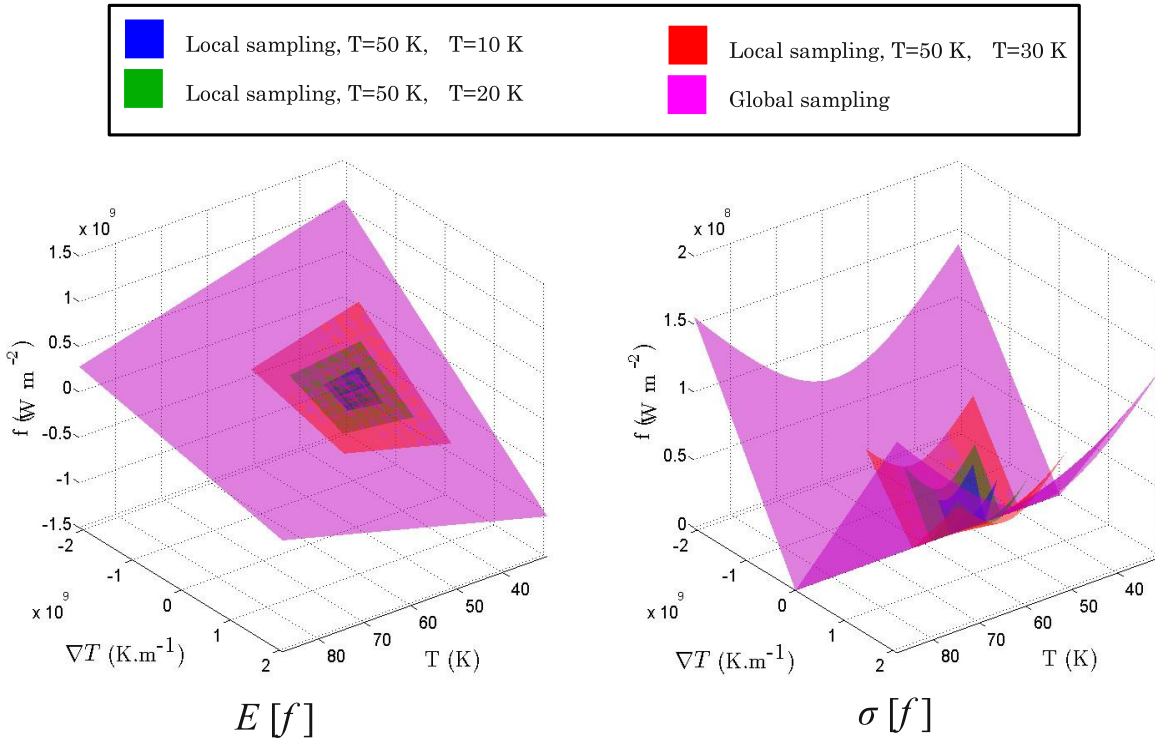

Figure 6.11. Plots showing the expectation E and standard deviation σ of the flux $q = (A - BT)\Delta T$ surface obtained after the inference of A and B. Results are obtained from $N_d = 16$ short-time $(f_j, \nabla T_j, T_j)$ data averaged at t_w =512 ps, using 4 replica MD simulations for different ranges of temperature by local and global sampling of the $\{\Delta T, T\}$ space, as indicated.

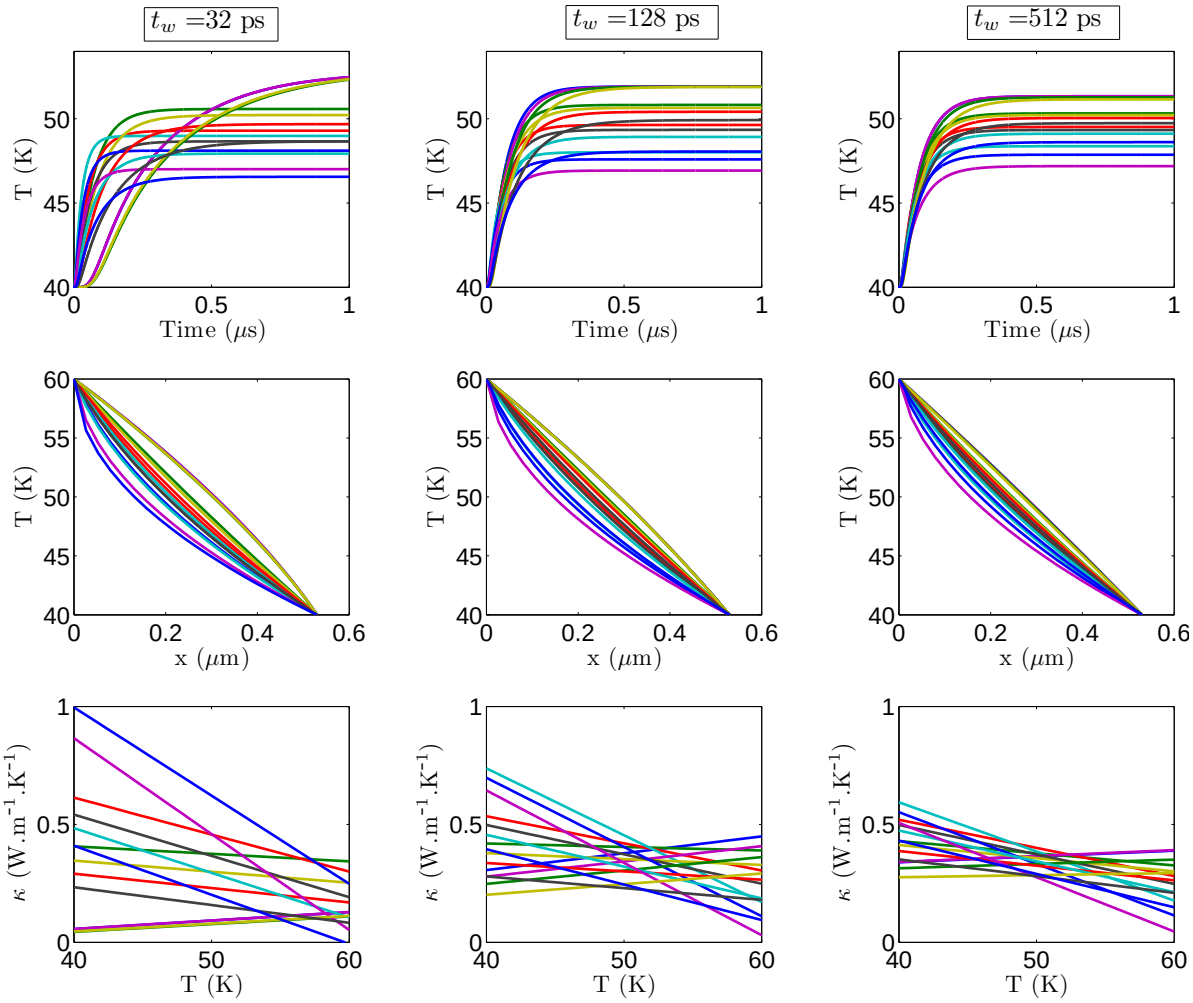

Figure 6.12. Plots showing the (top) temperature increase as a function of time in the middle of a continuum scale 1D bar ($x = 0.26\mu$s), (middle) the steady state temperature distribution in the bar, and (bottom) the steady state thermal conductivity as a function of the temperature. Results are obtained by simulating a continuum scale 1D bar with $L_c = 0.53\mu$m using a heat conduction constitutive law extracted from a MD at $\Delta T_{MD} = 20$ and K $T_{MD} =$ 50 K with $N_d = 64$ short-time averaged data points and different time averaging windows, as indicated. Each curve corresponds to a quadrature point when sampling the PCE of A and B ($\kappa = A - BT$).

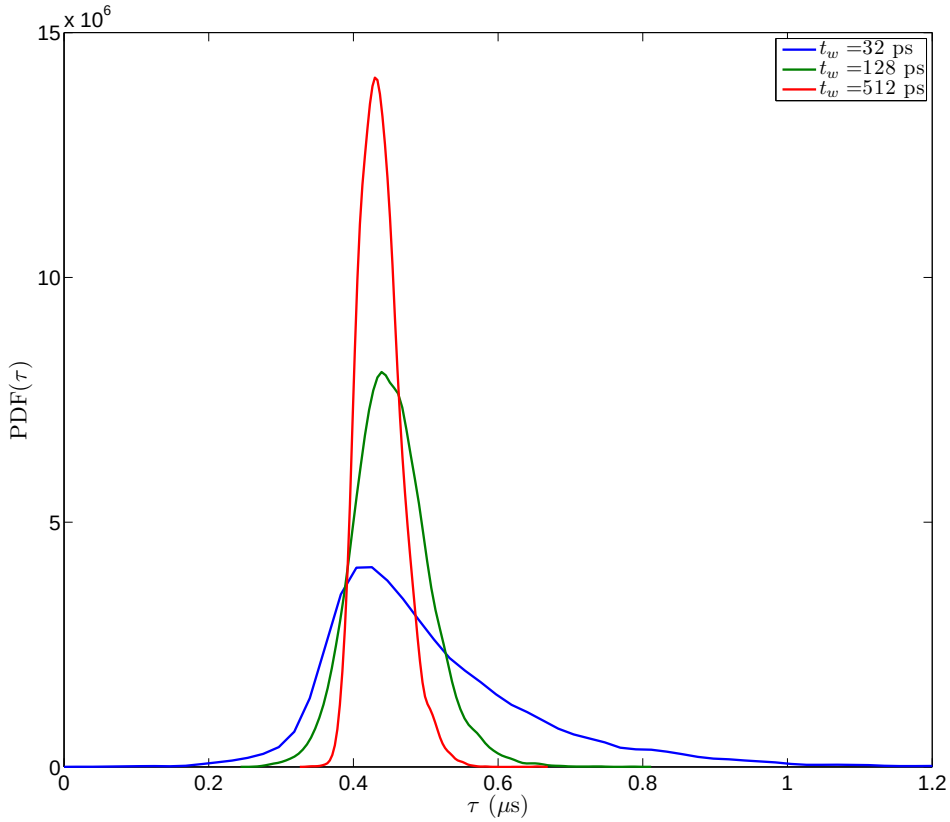

Figure 6.13. Plot showing the PDFs of the time scale (response time) of a continuum scale 1D bar with $L_c = 0.53\mu$m using a heat conduction constitutive law extracted from a MD at $\Delta T_{MD} = 20$ and K $T_{MD} = 50$ K with $N_d = 64$ short-time averaged data points and different time averaging windows, as indicated.

Chapter 7

Conclusions

The efforts in this work have focused on three key knowledge areas in which improvement is required to bridge the gap between atomistic simulation and engineering models capable of predictively simulating electric double layers. Bridging this gap in length and time scales, while retaining the effects of the discrete atoms near charged surfaces, is required to enable next generation battery and super-capacitor technology. To better understand the behavior of water-ion complexes at interfaces, quantum DFT calculations were performed. They showed that unanticipated hydration structures form as a result of the effectively reduced dimensionality resulting from confinement near the surface. In energy storage devices near interfaces, similar types of physical phenomena will likely occur. While the quantum calculations have successfully elucidated the physics, it proved difficult to tightly integrate them into the other models in this work. We suggest a future activity should focus on one of the missing aspects of multiscale research: quantum-to-atomistic (QtA) modeling. It is known that quantum models are needed to accurately capture electron transport and for understanding chemical reactions, as well as developing accurate interatomic potentials for surfaces and other non-bulk structures. Future work in this field would enable development of high-fidelity, low-expense chemistry models.

The second focus of this work was on development of a DFT model for the electric double layer DFT computes the equilibrium distribution of solvent and solute species by minimizing the energy defined as a function of the various densities. Calculations in this work all required less than one minute to perform, in contrast to the more accurate MD method which typically took on the order of a week using tens of processors. As we described, significant effort was required to obtain good agreement between the DFT and MD double layer representations. In particular, determining the most accurate electrical formulation for the DFT was critical. Once this form was identified, both models were in excellent agreement for a Lennard-Jones double layer. Note only does this result meet one of the goals of this project, to develop a fast and accurate double layer model, but the inclusion of atomistic effects results in the electrical properties significantly departing from classical PB theory. Therefore, it is important to utilize the DFT for engineering analysis and discovery. In order to increase its utility, a simple polar DFT model has been built to begin to account for solvent structure. An important near-term extension of this work would be to calibrate the simple polar model against MD of an aqueous solution using optimization techniques. Further work would develop more realistic solvent models, which requires substantial development in the Tramonto package. We also see the potential for a more innovative using of DFT which would incorporate time-dependence and stochasticity. These would enable this efficient method to model the charging and discharging processes, as well as possibly long-time diffusion dynamics which

are important to accurately model surface chemistry.

The final area investigated in this project was to how to obtain continuum transport coefficients from atomistic simulations. Much like the DFT work, established continuum transport models, e.g., viscosity and conductivity, can be solved very efficiently computationally. These properties often differ greatly between nanofluidic systems and their well characterized macroscale counterparts. MD allows nanosystems to be modeled, however extracting continuum properties is non-trivial. We developed an inhomogeneous Green-Kubo method capable of identifying spatially-varying transport coefficients perpendicular to a wall. In addition, Bayesian inference techniques were developed which can infer from MD calculations the coefficients of a prescribed functional form. At present, the Green-Kubo method is limited by long-range electrical interactions while the inference approach cannot identify constitutive laws different from the assumed form. Further efforts to resolve both issues would be of great use, although even in their present state, both can accurately estimate inhomogeneous transport laws which can be solved with orders of magnitude less effort than a full atomistic description.

We close with a final suggestion for future work: tight integration between the density and transport models identified by this project. To enable next-generation device design, both must be incorporated in an engineering analsyis code. Sandia has a logical package in SIERRA/Aria. DFT models would be appropriate for boundary conditions for microscale flows and as a substitute for the density equation for nanoscale flows. Aria already has the capability to simulate the necessary transport equations, and incorporating extracted constitutive laws is straightforward. However, a density update equation is that bridges the DFT and transport processes is necessary. Such a tool would enable engineers to analyze and optimize future electrical energy storage systems to meet the country's needs in the 21st century.

References

[1]

[2] Electrochemical energy storage technical team technology roadmap. Technical report, joint report of the U.S. Department of Energy Office of Energy Efficiency and Renewable Energy, FreedomCAR and Fuel Partnership and the U.S. Advanced Battery Consortium, July 2006.

[3] Scientific grand challenges in national security: the role of computing at the extreme scale. Technical report, U.S. Department of Energy, 2009.

[4] M. Abramowitz and I.A. Stegun. *Handbook of Mathematical Functions*. Dover, New York, 1970.

[5] H. Adalsteinsson, B. J. Debusschere, K. R. Long, and H. N. Najm. Components for atomistic-to-continuum multiscale modeling of flow in micro- and nanofluidic systems. *Scientific Programming*, 16:297–313, 2008.

[6] M.P. Allen and D.J. Tidlesley. *Computer Simulation of Liquids*. Oxford Science Publications, 1989.

[7] G. Anciaux, S.B. Ramisetti, and J.F. Molinari. A finite temperature bridging domain method for md-fe copuling and application to a contact problem. *Computational Methods in Applied Mechanics and Engineering*, 205:204–212, 2012.

[8] Barker, J.A. and Henderson, D. Perturbation theory and equation of state for fluids. II. A successful theory of liquids. *Journal of Chemical Physics*, 47(11):4714–4721, 1967.

[9] A. Bensoussan, J.L. Lions, and G. Papanicolaou. Boundary layers and homogenization of transport processes. *Publications of the Research Institute for Mathematical Sciences, Kyoto University*, 15(1):54–156, 1979.

[10] Bitsanis, I., Vanderlick, T.K., Tirrell, M., and Davis, H.T. A tractable molecular theory of flow in strongly inhomogenous fluids. *J. Chem. Phys.*, 89(5):3152–3163, 1988.

[11] A.W. Bowman and A. Azzalini. *Applied Smoothing Techniques for Data Analysis*. New York: Oxford University Press, 1997.

[12] G.C. Burton and W.J.A. Dahm. Multifractal subgrid-scale modeling for large-eddy simulation. I. Model development and *a priori* testing. *Physics of Fluids*, 17(7):075111, 205.

[13] R.H. Cameron and W.T. Martin. The orthogonal development of nonlinear functionals in series of Fourier-Hermite functionals. *Annals of Mathematics*, 48:385–392, 1947.

[14] Chowdhuri, S. and Chandra, A. Molecular dynamics simulations of aqeuous NaCl and KCl solutions: Effects of ion concentration on the single-particle, pair, and collective dynamical properties of ions and water molecules. *Journal of Chemical Physics*, 115(8):3732–3741, 2001.

[15] Conway, B.E. *Electrochemical Supercapacitors*. Kulwer Academic, New York, 1999.

[16] Crozier, P.S., Rowley, R.L., Spohr, E., and Henderson, D. Comparison of charged sheets and corrected 3D Ewald calculations of long-range forces in slab geometry electrolyte systems with solvent molecules. *Journal of Chemical Physics*, 112(21):9253–9257, 2000.

[17] Cui, S.T. and Cochran, H.D. Molecular dynamics simulation of interfacial electrolyte behaviors in nanoscale cylindrical pores. *Journal of Chemical Physics*, 117(12):5850–5854, 2002.

[18] S. R. de Groot and P. Mazur. *Non-equilibrium Thermodynamics*. Dover, 1984.

[19] A. Donev, J. B. Bell, A. L. Garcia, and B. J. Alder. A hybrid particle-continuum method for hydrodynamics of complex fluids. *SIAM Multiscale Modeling and Simulation*, 8:871–911, 2010.

[20] A. Donev, J.B. Bell, A.L. Garcia, and B.J. Alder. A hybrid particle-continuum method for hydrodynamics of complex fluids. *SIAM Journal on Multiscale Modeling and Simulation*, 8(3):871–911, 2010.

[21] W. E and B. Engquist. The heterogeneous multiscale methods. *Communications in Mathematical Sciences*, 1(1):87–132, 2003.

[22] W. E and X. Li. Analysis of the heterogeneous multiscale method for gas dynamics. *Meth. Appl. Analysis.*, 11(4):557–572, 2004.

[23] J.B. Goodenough *et al.* Basic research needs for electrical energy storage. Technical report, Report of the Basic Energy Sciences Workshop for Electrical Energy Storage, April 2007.

[24] Feng, G., Qiao, R., Huang, J., Sumpter, B.G., and Meunier, V. Ion distribution in electrofied micropores and its role in the anomalous enhancement of capacitance. *ACS Nano*, 4(4):2382–2390, 2010.

[25] A. Ferreira and S.S. Aphale. A survey of modeling and control techniques for micro- and nanoelectromechanical systems. *IEEE. Tran. Sys. Man. Cybernetics. Part C: Applications and Reviews*, 41(3):350–364, 2011.

[26] B. Frenkel and B. Smit. *Understanding Molecular Simulation: From Algorithms to Applications*. Elsevier, 2002.

[27] Freund, J.B. Electro-osmosis in a nanometer-scale channel studied by atomistic simulation. *Journal of Chemical Physics*, 116(5):2194–2200, 2002.

[28] N. Galamba, C. A. Nieto de Castro, and James F. Ely. Equilibrium and nonequilibrium molecular dynamics simulations of the thermal conductivity of molten alkali halides. *J. Chem. Phys.*, 126(20):204511, 2007.

[29] A. Gelman, J.B. Carlin, H.S. Stern, and D.B. Rubin. *Bayesian Data Analysis*. CRC/Chapman and Hall, 2003.

[30] M. Germano, U. Piomelli, P. Moin, and W.H. Cabot. A dynamic subgrid-scale eddy viscosity model. *Physics of Fluids A*, 3:1760–1765, 1991.

[31] R.G. Ghanem and P.D. Spanos. *Stochastic Finite Elements: A Spectral Approach*. Springer Verlag, 1991.

[32] R.G. Ghanem and P.D. Spanos. *Stochastic Finite Elements: A Spectral Approach*. Springer Verlag, New York, 1991.

[33] S. Ghosal, T.S. Lund, P. Moin, and K. Akselvoll. A dynamic localization model for large-eddy simulation of turbulent flows. *Journal of Fluid Mechanics*, 286:229–255, 1995.

[34] Gillespie, D., Nonner, W., and Eisenberg, R.S. Density functional theory of charged, hard-sphere fluids. *Physical Review E*, 68(3), 2003.

[35] Goel, T., Patra, C.N., Ghosh, S.K., and Mukherjee, T. Molecular solvent model of cylindrical electric double layers: a systematic study by Monte Carlo simulations and density functional theory. *Journal of Chemical Physics*, 129(15), 2008.

[36] Goel, T., Patra, C.N., Ghosh, S.K., and Mukherjee, T. Effect of ionic size on the structure of cylindrical electric double layers: A systematic study by Monte Carlo simulations and density functional theory. *Journal of Physical Chemistry B*, 115(37):10903–10910, 2011.

[37] I.G. Graham, T.Y. Hou, O. Lakkis, and R. Schechl. *Numerical Analysis of Multiscale Problems*. Springer, 2012.

[38] Grahame, D.C. The electrical double layer and the theory of electrocapillarity. *Chemical Reviews*, 41(3):441–501, 1947.

[39] G. Grimmett and D. Stirzaker. *Probability and Random Processes*. Oxford, 2011.

[40] J. Gullbrand and F.K. Chow. The effect of numerical errors and turbulence models in large-eddy simulations of channel flow, with and without explicit filtering. *Journal of Fluid Mechanics*, 495:323–341, 2003.

[41] R J Hardy. Formulas for determining local properties in molecular-dynamics simulations: Shock waves. *Journal of Chemical Physics*, 76(1):622–628, 1982.

[42] Hockney, R.W. and Eastwood, J.W. *Computer Simulation using Particles*. American Institute of Physics, New York: McGraw-Hill, 1988.

[43] Hoover, W.G. Canonical dynamics: Equilibrium phase-space distributions. *Physical Review A*, 31(3):1695–1697, 1985.

[44] T.J.R. Hughes, L. Mazzei, and K.E. Jansen. Large Eddy Simulation and the variational multiscale method. *Computing and Visualization in Science*, 3:47–59, 2000.

[45] J. H. Irving and J. G. Kirkwood. The statistical mechanical theory of transport processes. IV. The equations of hydrodynamics. *J. Chem. Phys.*, 18:817–829, 1950.

[46] S. Janson. *Gaussian Hilbert Spaces*. Cambridge University Press, 1997.

[47] Jones, J.E. On the determination of molecular fields. II. From the equation of state of a gas. *Proceedings of the Royal Society of London, Series A*, 106(738):436–477, 1924.

[48] Jorgensen, W.L., Chandrasekhar, J., Madura, J.D., Impey, R.W., and Klein, M.L. Comparison of simple potential functions for simulating liquid water. *Journal of Chemical Physics*, 79(2):926–935, 1983.

[49] Kim, D. and Darve, E. Molecular dynamics simulation of electro-osmotic flows in rough wall nanochannels. *Physical Review E*, 73(5):051203, 2006.

[50] E. M. Kotsalis, J. H. Walther, and P. Koumoutsakos. Hybrid atomistic-continuum method for the simulation of dense fluid flows. *J. Comput. Phys.*, 205(1):373 – 390, 2005.

[51] E.M. Kotsalis, J.H. Walther, and P. Koumoutsakos. Control of density fluctuations in atomistic-continuum simulations of dense liquids. *Physical Review E*, 76:016709, 2007.

[52] Lamperski, S., Outhwaite, C.W., and Bhuiyan, L.B. A modified Poisson-Boltzmann analysis of the solvent primitive model electrical double layer. *Molecular Physics*, 87(5):1049–1061, 1996.

[53] Lamperski, S. and Zydor, A. Monte Carlo study of the electrode—solvent primitive model electrolyte interface. *Electrochimica Acta*, 52(7):2429–2436, 2007.

[54] J. Lan and G. Li. A multiscale component mode synthesis approach for dynamic analysis of nanostructures. *J. Numer. Meth. Engrg.*, 2011. doi: 10.1002/nme.4330.

[55] O.P. Le Maître and O.M. Knio. *Spectral Methods for Uncertainty Quantification with Applications to Computational Fluid Dynamics*. Springer, 2010.

[56] O.P. Le Maître, O.M. Knio, H.N. Najm, and R.G. Ghanem. A stochastic projection method for fluid flow. I. Basic formulation. *Journal of Computational Phyics*, 173:481–511, 2001.

[57] O.P. Le Maître, M.T. Reagan, H.N. Najm, R.G. Ghanem, and O.M. Knio. A stochastic projection method for fluid flow II. Random process. *J. Comput. Phys.*, 181:9–44, 2002.

[58] A.R. Leach. *Molecular Modelling: Principles and Applications*. Pearson, 2001.

[59] Lee, J.W., Nilson, R.H., Templeton, J.A., Griffiths, S.K., Kung, A., and Wong, B.M. Comparison of molecular dynamics with classical density functional and poisson-boltzmann theories of the electric double layer in nanochannels. *Journal of Chemical Theory and Computation*, 2012.

[60] Magda, J.J., Tirrell, M., and Davis, H.T. Molecular dynamics of narrow, liquid-filled pores. *Journal of Chemical Physics*, 83(4):1888–1901, 1985.

[61] Martyna, G.J., Klein, M.L., and Tuckerman, M. Nosé-Hoover chains: The canonical ensemble via continuous dynamics. *Journal of Chemical Physics*, 97(4):2635–2643, 1992.

[62] Y.M. Marzouk, H.N. Najm, and L.A. Rahna. Stochastic spectral methods for efficient bayesian solution of inverse problems. *J. Comp. Phys.*, 224:560–586, 2007.

[63] R.E. Miller and E.B. Tadmor. A unified framework and performance benchmark of fourteen multiscale atomistic/continuum coupling methods. *Modeling and Simulation in Materials Science and Engineering*, 17:053001, 2009.

[64] N. Moes, J. Dolbow, and T. Belytschko. A finite element method for crack growth without remeshing. *International Journal for Numerical Methods in Engineering*, 46(1):131–150, 1999.

[65] A. Mohammad-Djafari. Bayesian inference for inverse problems. In *Bayesian inference and Maximum Entropy Methods in Science and Engineering*, volume 21, pages 477–496, 2002.

[66] X. Nie, S. Chen, and M.O. Robbins. Hybrid continuum-atomistic simulation of singular corner flow. *Physics of Fluids*, 16(10):3579–3591, 2004.

[67] Nilson, R.H. and Griffiths, S.K. Influence of atomistic physics on electro-osmotic flow: An analysis based on density functional theory. *Journal of Chemical Physics*, 125(16), 2006.

[68] J. Nolen and G. Papanicolaou. Fine scale uncertainty in parameter estimation for elliptic equations. *Inverse Problems*, 25:115021, 2009.

[69] Nosé, S. A unified formulation of the constant temperature molecular dynamics methods. *Journal of Chemical Physics*, 81(1):511–519, 1984.

[70] Patra, C.N. and Ghosh, S.K. Structure of electric double layers: A self-consistent weighted-density-functional approach. *Journal of Chemical Physics*, 117(19):8938–8943, 2002.

[71] S.J. Plimpton. Fast parallel algorithms for short-range molecular dynamics. *J. Comp. Phys.*, 117:1–19, 1995. http://lammps.sandia.gov.

[72] Plimpton, S.J. Fast parallel algorithms for short-range molecular dynamics. *Journal of Computational Physics*, 117(1):1–19, 1995.

[73] Poisson, S.D. *Bulletin de la societe philomatique*, 1813.

[74] L.A. Pozhar. Structure and dynamics of nanfluidics: theory and simulation to calculate viscosity. *Physical Review E*, 41:1432, 2000.

[75] Qiao, R. and Aluru, N.R. Ion concentrations and velocity profiles in nanochannel electroosmostic flows. *Journal of Chemical Physics*, 118(10):4692–4701, 2003.

[76] Qiao, R. and Aluru, N.R. Charge inversion and flow reversal in a nanochannel electro-osmotic flow. *Physical Review Letters*, 92(19):198301, 2004.

[77] W. Ren. Analytical and numerical study of coupled atomistic-continuum methods for fluids. *Journal of Computational Physics*, 227:1353–1371, 2007.

[78] L.A. Ricardez-Sandoval. Current challenges in the design and control of multiscale systems. *Canadian. J. Chem. Engrg.*, 89(6):13241341, 2011.

[79] F. Rizzi, H.N. Najm O.M. Knio, B. Debusschere, K. Sargsyan, M. Salloum, and H. Adalsteinsson. Uncertainty quantification in md simulations: Forward propagation and parameter inference. In P. Koumoutsakos, editor, *Bulletin of the American Physical Society: 64th Annual Meeting of the APS Division of Fluid Dynamics*, volume 56, 2011.

[80] F. Rizzi, M. Salloum, Y.M. Marzouk, R.G. Xu, M.L. Falk, T.P. Weihs, G. Fritz, and O.M. Knio. Bayesian inference of atomic diffusivity in a binary Ni/Al system based on molecular dynamics. *SIAM Mult. Model. Simul.*, 9:486–512, 2011.

[81] D. Rowe. *Multivariate Bayesian Statistics: Models for Source Separation and Signal Unmixing*. Chaplain-Hall, 2003.

[82] Ryckaert, J.-P., Ciccotti, G., and Berendsen, H.J.C. Numerical integration of the Cartesian equations of motion of a system with constraints: Molecular dynamics of *n*-alkanes. *Journal of Computational Physics*, 23(3):327–341, 1977.

[83] Musabbir A. Saeed, Avijit Pramanik, Bryan M. Wong, Syed Ataul Haque, Douglas R. Powell, Dillip Kumar Chand, and Md. Alamgir Hossain. Self-assembly of ordered water tetramers in an encapsulated [Br(H2O)(12)](-) complex. *CHEMICAL COMMUNICATIONS*, 48(69):8631–8633, 2012.

[84] M. Salloum, K. Sargsyan, H.N. Najm, B. Debusschere, R. Jones, and H. Adalsteinsson. A stochastic multiscale coupling scheme to account for sampling noise in atomistic-to-continuum simulations. *SIAM. Multi. Model. Simu.*, 10(2):550–584, 2011.

[85] K. Sargsyan, B. Debusschere, H.N. Najm, and O.P. Le Maître. Spectral representation and reduced order modeling of the dynamics of stochastic reaction networks via adaptive data partitioning. *SIAM. J. Sci. Comput.*, 31(6):43954421, 2010.

[86] K. Sargsyan, C. Safta, B. Debusschere, and H.N. Najm. Uncertainty quantification given discontinuous model response and a limited number of model runs. *SIAM. J. Sci. Comput.*, 34(1):B44B64, 2012.

[87] D.S. Sivia and J. Skilling. *Data Analysis, A Bayesian Tutorial*. Oxford Science, second edition, 2006.

[88] Snook, I. and van Megen, W. Structure of dense liquids at solid interfaces. *Journal of Chemical Physics*, 70(6):3099–3105, 1979.

[89] Spohr, E. Molecular simulation of the electrochemical double layer. *Electrochimica Acta*, 44(11):1697–1705, 1999.

[90] Tang, Z., Scriven, L.E., and Davis, H.T. A three-component model of the electrical double layer. *Journal of Chemical Physics*, 97(1):494–503, 1992.

[91] Tang, Z.X., Mier-y-Teran, L., Davis, H.T., Scriven, L.E., and White, H.S. Nonlocal free-energy density-functional theory applied to the electrical double layer. 1. Symmetrical electrolytes. *Molecular Physics*, 71(2):369–392, 1990.

[92] Tarazona, P. Free-energy density functional for hard-spheres. *Physical Review A*, 31(4):2672–2679, 1985.

[93] J.A. Templeton, R.E. Jones, and G.J. Wagner. Application of a field-based method to spatially varying thermal transport problems in molecular dynamics. *Modeling. Simul. Mater. Sci. Eng.*, 18, 2010.

[94] Thompson, A.P. Nonequilibrium molecular dynamics simulation of electro-osmotic flow in a charged nanopore. *Journal of Chemical Physics*, 119(14):7503–7511, 2003.

[95] Torrie, G.M. and Valleau, J.P. A Monte Carlo study of an electrical double layer. *Chemical Physics Letters*, 65(2):343–346, 1979.

[96] Vanderlick, T.K., Scriven, L.E., and Davis, H.T. Molecular theories of confined fluids. *Journal of Chemical Physics*, 90(4):2422–2436, 1989.

[97] Verlet, L. Computer "experiments" on classical fluids. I. Thermodynamical properties of Lennard-Jones molecules. *Physical Review*, 159(1):98–103, 1967.

[98] Verlet, L. Computer "experiments" on classical fluids. II. Equilibrium correlation functions. *Physical Review*, 165(1):201–214, 1968.

[99] G.J. Wagner, R.E. Jones, J.A. Templeton, and M.L. Parks. An atomistic-to-continuum coupling method for heat transfer in solids. *Computational Methods in Applied Mechanics and Engineering*, 197:3351–3365, 2008.

[100] G.J. Wagner, R.E. Jones, J.A. Templeton, and M.L. Parks. An atomistic-to-continuum coupling method for heat transfer in solids. *Comput. Methods Appl. Mech. Engrg.*, 197:3351–3365, 2008.

[101] Waisman, E. and Lebowitz, J.L. Mean spherical model integral-equation for charged hard spheres I. Method of solution. *Journal of Chemical Physics*, 56(6), 1972.

[102] Waisman, E. and Lebowitz, J.L. Mean spherical model integral-equation for charged hard spheres. II. Results. *Journal of Chemical Physics*, 56(6), 1972.

[103] Wander, M.C.F. and Shuford, K.L. Molecular dynamics study of interfacial confinement effects of aqueous NaCl brines in nanoporous carbon. *Journal of Physical Chemistry C*, 114(48):20539–20546, 2010.

[104] X. Wang, J. Li, J.D. Lee, and A. Eskandarian. On the multiscale modeling of multiple physics. In S. Li and X. Ga, editors, *Handbook of Micromechanics and Nanomechanics*, pages 1–24, 2012.

[105] Wang, H. and Laurent, P. Accurate simulations of electric double layer capacitance of ultramicroelectrodes. *Journal of Physical Chemistry C*, 115(33):16711–16719, 2011.

[106] Wang, Z., Liu, L., and Neretnieks, I. The weighted correlation approach for density functional theory: a study on the structure of the electric double layer. *Journal of Physics: Condensed Matter*, 23(17), 2011.

[107] Dean R. Wheeler and John Newman. Molecular dynamics simulations of multicomponent diffusion. 1. equilibrium method. *The Journal of Physical Chemistry B*, 108(47):18353–18361, 2004.

[108] Widom, B. Some topics in the theory of fluids. *Journal of Chemical Physics*, 39(11):2808–2812, 1963.

[109] N. Wiener. The homogeneous chaos. *Am. J. Math.*, 60:897–936, 1938.

[110] Willard, A.P., Reed, S.K., Madden, P.A., and Chandler, D. Water at an electrochemical interface–a simulation study. *Faraday Discussions*, 141:423–441, 2009.

[111] Wu, P. and Qiao, R. Physical origins of apparently enhanced viscosity of interfacial fluids in electrokinetic transport. *Physics of Fluids*, 23(7), 2011.

[112] L. Xionga, Q. Denga, G. Tuckerb, D.L. McDowellb, and Y. Chena. A concurrent scheme for passing dislocations from atomistic to continuum domains. *Acta. Mater.*, 60(3):899913, 2012.

[113] Xu, D., Li, D., Leng, Y., and Chen, Y. Molecular dynamics simulations of ion distribution in nanochannels. *Molecular Simulation*, 33(12):959–963, 2007.

[114] Yeh, I.-C. and Berkowitz, M.L. Ewald summation for systems with slab geometry. *Journal of Chemical Physics*, 111(7):3155–3162, 1999.

[115] Yanhua Zhou and Gregory H. Miller. Greenkubo formulas for mutual diffusion coefficients in multicomponent systems. *The Journal of Physical Chemistry*, 100(13):5516–5524, 1996.

[116] J.A. Zimmerman, R.E. Jones, and J.A. Templeton. A material frame approach for evaluating continuum variables in atomistic simulations. *J. Comput. Phys.*, 229:2364–2389, 2010.

[117] Zimmerman, J.A., Webb III, E.B., Hoyt, J.J., Jones, R.E., Klein, P.A., and Bammann, D.J. Calculation of stress in atomistic simulation. *Modelling and Simulation in Materials Science and Engineering*, 12(4):S319–S332, 2004.

DISTRIBUTION:

1	MS 0899	Technical Library, 8944 (electronic)
1	MS 0123	D. Chavez, LDRD Office, 1011

This page intentionally left blank.

Sandia National Laboratories